INVESTIGATION AND MODELING OF PROCESSING-

MICROSTRUCTURE-PROPERTY RELATIONS IN ULTRA-FINE

GRAINED HEXAGONAL CLOSE PACKED MATERIALS UNDER

STRAIN PATH CHANGES

A Dissertation

by

GUNEY GUVEN YAPICI

Submitted to the Office of Graduate Studies of
Texas A&M University
in partial fulfillment of the requirements for the degree of

DOCTOR OF PHILOSOPHY

August 2007

Major Subject: Mechanical Engineering

INVESTIGATION AND MODELING OF PROCESSING-MICROSTRUCTURE-PROPERTY RELATIONS IN ULTRA-FINE GRAINED HEXAGONAL CLOSE PACKED MATERIALS UNDER STRAIN PATH CHANGES

A Dissertation

by

GUNEY GUVEN YAPICI

Submitted to the Office of Graduate Studies of
Texas A&M University
in partial fulfillment of the requirements for the degree of

DOCTOR OF PHILOSOPHY

Approved by:

Chair of Committee,	Ibrahim Karaman
Committee Members,	Karl Theodore Hartwig
	Xinghang Zhang
	Tahir Cagin
Head of Department	Dennis L. O'Neal

August 2007

Major Subject: Mechanical Engineering

ABSTRACT

Investigation and Modeling of Processing-Microstructure-Property Relations in Ultra-

Fine Grained Hexagonal Close Packed Materials under Strain Path Changes.

(August 2007)

Guney Guven Yapici, B.S., Bogazici University, Turkey;

M.S., Texas A&M University

Chair of Advisory Committee: Dr. Ibrahim Karaman

Ultra-fine grained (UFG) materials have attracted considerable interest due to the possibility of achieving simultaneous increase in strength and ductility. Effective use of these materials in engineering applications requires investigating the processing-microstructure-property inter-relations leading to a comprehensive understanding of the material behavior. Research efforts on producing UFG hexagonal close packed (hcp) materials have been limited in spite of their envisaged utilization in various technologies. The present study explores multiple UFG hcp materials to identify the general trends in their deformation behaviors, microstructural features, crystallographic texture evolutions and mechanical responses under strain path changes.

UFG hcp materials, including commercial purity Ti, Ti-6Al-4V alloy and high purity Zr, were fabricated using equal channel angular extrusion (ECAE) as a severe plastic deformation (SPD) technique following various processing schedules. Several characterization methods and a polycrystal plasticity model were utilized in synergy to impart the relationships between the UFG microstructure, the texture and the post-ECAE flow behavior.

Pure UFG hcp materials exhibited enhanced strength properties, making them potential substitutes for coarse-grained high strength expensive alloys. Incorporation of post-ECAE thermo-mechanical treatments was effective in further improvement of the

strength and ductility levels. Strong anisotropy of the post-ECAE flow response was evident in all the materials studied. The underlying mechanisms for anisotropy were identified as texture and processing-induced microstructure. Depending on the ECAE route, the applied strain level and the specific material, the relative importance of these two mechanisms on plastic flow anisotropy varied. A viscoplastic self-consistent approach is presented as a reliable model for predicting the texture evolutions and flow behaviors of UFG hcp materials in cases where texture governs the plastic anisotropy.

Regardless of the material, the initial billet texture and the extrusion conditions, ECAE of all hcp materials revealed similar texture evolutions. Accurate texture and flow behavior predictions showed that basal slip is the responsible mechanism for such texture evolution in all hcp materials independent of their axial ratio. High strength of the UFG microstructure was presented as a triggering mechanism for the activation of unexpected deformation systems, such as high temperature deformation twinning in Ti-6Al-4V and room temperature basal slip in pure Zr.

Dedicated To My Parents, Selma and Cahit Yapici

I am proud to be your son.

ACKNOWLEDGMENTS

Foremost, I wish to express my profound gratitude to my advisor, Dr. Ibrahim Karaman, who has been a great source of inspiration, and who has provided invaluable scientific guidance in various aspects of my research. I am especially thankful to him for giving me the opportunity to work on a variety of projects related to the work presented herein.

I would also like to thank Dr. Ted Hartwig. He shared his invaluable experience and knowledge in the severe plastic deformation area. I would also like to thank him for helping me discover the methods of successful scientific writing. I would like to thank Dr. Xinghang Zhang and Dr. Tahir Cagin for their constructive comments at various stages in this work.

I wish to thank Dr. Hans Maier for being a great collaborator on various projects throughout my graduate study and for being a wonderful host at the University of Paderborn. Dr. Carlos Tome and Dr. Irene Beyerlein are especially thanked for giving me the opportunity to research at Los Alamos National Laboratory. Their immense experience in crystal plasticity helped me to obtain the accurate predictions presented in this work.

I am grateful to the help Mr. Robert Barber provided regarding the deformation processing issues of the present work. Dr. Zhiping Luo is thanked for his assistance in TEM work and letting me benefit from his invaluable TEM experience. Dr. Vogel, Dr. Liu, Dr. Necker and Dr. Proust are thanked for their help on the experimental part of my work at Los Alamos. I would also like to thank the several research group members I worked with over the past years. Their existence made my stay at Texas A&M an enjoyable and memorable one.

Last, but most importantly, the continuous courage and support received from my family is sincerely appreciated. I would like to thank my brother, Murat Yapici for being

vii

a friend, roommate and colleague during my graduate study. The immense love of my parents, Selma and Cahit Yapici, has been a key aspect in the completion of my graduate work. Without their support, this work would not be possible.

TABLE OF CONTENTS

LIST OF FIGURES

Page

LIST OF TABLES

CHAPTER I

INTRODUCTION

1.1. Motivation

Characterizing and modeling the response of materials after deformation processing have always attracted interest in the scientific community. Deformation processing of hcp materials has, up to now, involved conventional techniques such as rolling, drawing and extrusion at ambient and elevated temperatures [1, 2]. Recently, severe plastic deformation (SPD) techniques have been utilized to obtain ultra-fine grained (UFG) materials for many important engineering applications. Obtaining an UFG microstructure is crucial due to the mechanical property improvements it provides [3-7].

Conventional deformation methods, such as rolling, drawing and extrusion can impart large strains on the work-piece. However, one or more dimensions of the sample are always gradually reduced during deformation, thus a foil or filament with limited applications is produced. Additionally, refining grain size with these methods is not very efficient. These methods are limited in the amount of strain that may be imparted. Thus, for instance grain sizes in rolled materials are typically above sub-micron range. In addition, since they generally do not involve any strain path changes and at most are redundant strain processes with strain reversals; they are less effective for subdividing the original grain structure [8-11]. It has been reported that the original grain shapes, grain orientations and textures can be largely restored upon strain reversals. In this respect, utilizing severe plastic deformation techniques involving abrupt strain path changes improves the efficiency to produce an ultra-fine grained microstructure. This study employed ECAE as the severe plastic deformation technique due to its many advantages in quest for obtaining improved mechanical properties via grain size refinement down to submicron levels.

Achieving the ECAE of materials for grain size refinement is a processing issue in this research. However, equal importance should be given to the characterization of microstructure and mechanical behavior obtained during ECAE. Investigating the processing-microstructure-property inter-relations is necessary to have a comprehensive

_____

This dissertation follows the style and format of Acta Materialia.

understanding of the material's mechanical behavior. In return, effective processing routes can be devised to produce suitable microstructures with desired resultant mechanical properties. Although countless studies contributed to the characterization of ECAE deformed materials, not many followed an approach describing the inter-relations mentioned above.

An important tool in linking the deformation processing and the resulting properties is polycrystal plasticity modeling. Polycrystal plasticity of hcp materials involves a variety of deformation mechanisms, including substantial twinning activity, and anisotropic single crystals. Thus, a modeling approach that can assess the impact of the grain anisotropy on the deviation of its response with respect to the aggregate is necessary. Additionally, the model has to account for the abrupt orientation change during twinning and its effect on texture evolution and hardening response. In this study, a viscoplastic self-consistent approach is employed to predict the texture evolution and mechanical response of hcp materials during ECAE and post-ECAE straining. The modeling efforts aim at reducing the number of experimental trials for optimizing the processing parameters that will lead to desired mechanical properties and texture evolution. Additionally, it would help identifying the underlying deformation mechanism responsible for observed texture evolution and mechanical response and will support the microstructural characterizations.

ECAE has been applied to many materials with the common goal of improving the strength levels. However, limited research has been focused on hcp materials [12-22]. Hcp materials receive attention due to several reasons. First of all, many hcp materials have technological importance and investigating whether their mechanical properties can be optimized by ECAE has merit. Since hcp materials have limited deformation systems available, ECAE processing presents a challenge and achieving this task could open new frontiers in the applicability of these materials. Especially, increasing the strength levels of pure hcp metals without a huge loss in ductility via grain refinement and post-processing annealing treatments will make these advanced UFG materials as alternatives to coarse-grained heavily alloyed expensive material systems.

It is expected that the high strain levels reached through various deformation routes of ECAE could lead to the formation of strong textures which may not be

accessible with conventional processing methods. Since hcp materials are highly sensitive to crystallographic texture due to their low symmetry crystal structures, investigating the evolution of texture during ECAE is of paramount importance. In addition, formation of dense dislocation boundaries was observed in heavily deformed face centered cubic (fcc) and body centered cubic (bcc) materials [23-28]. However, there is not sufficient information regarding the microstructural evolution during severe deformation of hcp materials. Insight into the texture evolution and processing induced microstructure development of severely deformed hcp materials is important due to their reflection on the mechanical behavior.

The main mechanisms that contribute to the directional dependence of the material behavior are crystallographic texture, directional substructure and presence of internal stress [29-35]. Textured materials where there is a tendency for certain preferred orientations exhibit anisotropic mechanical properties. Secondly, during deformation processing well organized dislocation boundaries tend to form. Among the processing conditions, strain level is highly influential in transforming the dislocation substructure from a random one to an aligned and developed one. In this respect, microstructural evolution of fcc, e.g. copper and aluminum, and bcc, e.g. interstitial free (IF) steel, materials after ECAE was shown to be highly directional consisting of elongated lamellar dislocation substructures [36-40]. Formation of dense dislocation boundaries has been documented to be effective in dictating the post-processing mechanical anisotropy of heavily deformed materials by changing the mean free path of gliding dislocations.

Hexagonal materials have low symmetry crystal structures making them anisotropic without the need of complex multi-strain paths due to the multiplicity of deformation modes [41-44]. Thus, the importance of both texture and dislocation substructure formation on mechanical behavior and anisotropy of hcp materials is even higher as compared to cubic crystals. With that in my mind, the present research materials are subjected to deformation processing up to very high strain levels involving abrupt strain path changes magnifying the effect of the two aforementioned mechanisms on mechanical behavior. Unfortunately, investigation of these topics on hcp materials during ECAE has not received noticeable attention as compared to the cubic counterparts. Indeed, it is considerably limited for the severely deformed cubic materials as well [29,

45-47]. However, industry scale forming applications generally require multiple strain-paths with moderate to high strain levels and transforming the current UFG material production technologies to commercial use would not be possible without the understanding of root mechanisms causing anisotropic behavior in their mechanical response.

1.2. Technical Approach

With the motivation outlined in the previous section, the present study considered the following hcp metals and alloys due to their technological importance in several advanced technology applications. The materials selected for this study are commercial purity (CP) Ti, Ti-6Al-4V (Ti64) alloy and high purity Zr. These three materials have similar deformation mechanisms, however the relative ease of a certain deformation system is different in each material. Thus for each material, different processing schedules were used to ensure uniform deformation without shear localization. In addition, purity level and tendency for shear localization are other factors that determine the ease of processing. Specifically, Ti64 was investigated to see the effect of second phase on ECAE processing parameters and the effect of high temperature ECAE deformation on microstructural development. On the other hand, efforts on high purity Zr aimed at investigating the sole effect of ECAE deformation on microstructural development by eliminating the possible dynamic recrystallization effects that might otherwise take place during high temperature processing of Ti and Ti64.

In light of the main motives behind this research, the overall objectives of the present research with specific details pertaining to each material studied are stated below. To accomplish these objectives, a set of experimental and computational methods has been utilized.

1. Perform ECAE processing of Ti, Ti64 and Zr at minimum possible deformation temperatures to prevent the adverse effects of recovery-recrystallization on microstructure evolution and at high enough temperatures to achieve a uniformly deformed ultra-fine grained microstructure free of shear localization.

2. Investigate the microstructural development and crystallographic texture evolution of the research materials after ECAE using a multitude of experimental

characterization methods. Identify the common trends and apparent contrasts in the microstructural features and the textures evolved after ECAE among the materials studied.

3. Predict the texture evolution of ECAE processed materials utilizing crystal plasticity modeling tools by incorporating experimental observation of active deformation mechanisms.

4. Determine the post-ECAE mechanical response of the research materials, identify the presence of possible directional dependency of the mechanical response. Explore the mechanisms responsible for the anisotropy using experimental and plasticity modeling tools and thus clarify the specific effects of texture and processing induced microstructure on the anisotropy. Investigate the extent of each mechanism for each material subjected to different processing routes.

5. Investigate operative deformation mechanisms during ECAE of the research materials. Underline the deformation systems common to all material studied and the reasons behind their activation. In this respect, examine the possible activation of abnormal deformation systems that are expected to be inactive for a given material under respective deformation conditions. Devise mechanistic models triggering the operation of these deformation mechanisms.

More specifically, the following goals were set for the materials in focus.

1. Microstructural refinement of CP Grade 2 Ti via ECAE and post-ECAE cold rolling for reaching strength levels as compared to that of as-received Ti64, with relatively high uniform ductility. Optimize the mechanical properties using post-processing heat treatments. Determine the mechanical behavior of severely deformed CP Grade 2 Ti and CP Grade 4 Ti via uniaxial tension experiments at room temperature.

2. Investigate the in-plane anisotropy of the post-ECAE cold rolled CP Grade 2 Ti slabs. Identify the possible mechanisms causing anisotropy by underlining their individual contributions.

3. Exhibit the crystallographic texture evolution during ECAE and post-ECAE rolling of CP Grade 2 Ti. Identify the effect of texture on the anisotropy of post-

ECAE cold rolled CP Grade 2 Ti using a viscoplastic self-consistent polycrystal plasticity model.

4. Achieve improved strength levels in ECAE processed Ti64 via grain refinement. Demonstrate both tensile and compressive flow behaviors at room temperature.

5. Demonstrate the high temperature deformation systems in severely deformed Ti64. Devise possible mechanisms for the activation of these systems.

6. Exhibit the crystallographic texture developed during ECAE of Ti64 and predict its evolution using a viscoplastic self-consistent modeling approach.

7. Identify the reasons for possible differences in the tension and compression responses of ECAE processed Ti64.

8. Achieve room temperature ECAE of pure Zr. Demonstrate the microstructural evolution and resulting mechanical behavior along three orthogonal directions of the extruded billet.

9. Exhibit the texture evolution of pure Zr after ECAE and post-ECAE room temperature compression experiments. Predict the texture evolution during ECAE and post-ECAE straining via modeling efforts. At the same time, simulate the post-ECAE compression response along three orthogonal directions.

10. Investigate the possible anisotropy obtained via multi directional compression experiments. Explain the anisotropy in light of texture evolved during ECAE and identify the responsible deformation mechanisms.

Achievement of these goals will form a basis for understanding the processing-microstructure-property relations in the individual hcp material studied. Focusing on three different materials is important because it will enable to recognize the common trends and striking differences in microstructures and textures evolved during ECAE and post-ECAE mechanical behavior. It will also exhibit the effect of material inherent properties on the suitable ECAE processing schedule to be followed for achieving uniformly deformed UFG microstructures. Moreover, identifying the responsible deformation mechanisms for the observed texture evolutions and mechanical behaviors in each material will help to identify the common systems in operation during ECAE of hcp materials.

CHAPTER II
TECHNICAL BACKGROUND

2.1. Ultra-fine Grained Materials and Fabrication Techniques

Ultra-fine grained (UFG) materials can be defined as polycrystalline materials that are composed of very fine grains and have large grain boundary area. The grain size is in the submicron regime and can go down to nanometer scale as well. Bulk nanocrystalline (nc) materials contain grains with average size less than 100 nm [48, 49]. The presence of fine grains and large grain boundary area results in improved physical and mechanical properties [3, 6, 49-52].

Several fabrication techniques are currently available to produce nc and UFG materials. They can be generally classified into the following five groups as mechanical milling and compaction [53-55], severe plastic deformation [3, 5, 56], consolidation via severe plastic deformation [57-59], inert gas condensation of particulates and consolidation [60-62] and electrodeposition [63, 64]. Whereas the first two methods typically tend to yield material with ultra-fine grain sizes, the latter three techniques are capable of producing material with mean grain sizes in the tens of nm. Each of these methods has advantages and disadvantages and one should choose the appropriate method depending upon the material design attributes. Here, only the methods used for producing UFG materials will be discussed in detail.

Mechanical milling or ball milling is an efficient synthesis technique for obtaining large quantities of UFG and nc materials where the resulting powder can be consolidated to near full density with insignificant grain growth. Mechanical milling is based on heavy cyclic plastic deformation in order to subject the coarse grained powders to structural deformation. Coarse-grained powders are put together with hardened steel balls in a sealed container and violently agitated. During this process the powder particles deform, cold weld and fracture due to the collisions with hardened steel balls and the container walls [54, 55]. This process has become a popular method because of its simplicity, relatively inexpensive equipment, and its applicability to essentially all classes of materials. There are certain problems such as powder contamination from milling media and/or atmosphere, and obtaining full density during compaction. Residual porosity in

compacted samples, and inability to process large scale sample are major drawbacks [65]. Moreover, requirement of a multi-step process of fabrication plus consolidation is costly and time consuming [54].

Inert gas condensation consists of evaporating a metal inside a chamber that under high vacuum and then backfilled with inert gas, such as helium. The evaporated atoms collide with the gas atoms, lose their kinetic energy, and then condense as small, discrete crystals of loose powder. Convection currents, generated due to the heating of the inert gas by the evaporation source and cooled by the liquid nitrogen-filled collection device (cold finger), carry the condensed fine powders to the collector device, from where they can be stripped off from the cold finger into a compaction device. Upon removal, the clusters of nanoparticles fall from the surface and are funneled into a set of compaction devices, in which the nanophase samples are formed at room temperature, or at elevated temperatures if needed. The compaction processes are also carried out under ultra-high vacuum conditions to maintain cleanliness of the particles surface and also to minimize the amount of any trapped gases [66]. Drawbacks include limited specimen volume and yield, purity issues particularly in the vicinity of the particle boundaries, incomplete densification/porosity, and difficulties associated with retaining the fine grain size during consolidation. The process can provide a microstructure that is usually texture-free and consisting of equiaxed grains [67].

In contrast, severe plastic deformation (SPD) techniques eliminate the shortcomings of inert gas condensation and ball milling methods associated with material purity and deformed billet size [5]. SPD methods can impart very high strains to refine the grain size down to submicron level without a change in the billet dimensions. There are several SPD techniques developed and will be reviewed in this section briefly.

Equal channel angular extrusion (ECAE) was originally developed by Segal and offers the potential of achieving grain refinement, and of producing UFG materials with corresponding improvements in mechanical properties [68]. An ECAE die consists of two channels of equal cross-section intersecting at an angle through which a billet of material is extruded. The billet experiences a state of simple shear while passing through the channel intersection [68]. The name "equal channel" comes from the fact that the inlet and outlet channels have the same cross section. This enables that the billet cross section

does not change during processing and thus very large strains may be achieved in bulk material by repetitive ECAE operations. The only known disadvantage of this method is that it is not continuous and requires human interference. Improvements in die design are necessary to commercialize this technology. Details regarding the ECAE technique will be explained later.

High pressure torsion (HPT) was also developed as an SPD method in Russia [50, 69]. During HPT, a disc of material is placed between two plates and high pressure, normally in the GPa range, is applied. One of the plates is then rotated and the disc of material is deformed in shear through the frictional effects with the plates. The strain in the material is a function of location along the disc radius and number of rotations of the tool [69], and hence is non-uniform throughout the sample. This procedure is limited to the formation of disc-shaped samples that are measured in millimeters. Details regarding this method can be found in [3, 69].

Accumulative roll bonding (ARB) is a method that utilizes conventional rolling to induce severe plastic deformation into a material. ARB was developed in Japan [70] and has been studied recently [71, 72]. This process uses conventional rolling. After each rolling pass, the material is cut in half, the surfaces to be bonded are prepared and the two plates are stacked on top of one another. By this way, the sample returns almost to the original length and thickness. Finally, the stacked plates are subjected to another rolling operation intended to bond the plates while again reducing the thickness of the stack. The process is repeated until the desired strain is achieved. The surface preparation must include careful cleaning and surface preparation [70]. Delamination and problems with contamination during bonding have also been reported [72].

Friction-stir processing technique involves traversing a rotating tool under an applied force, across the surface of a material, producing intense plastic deformation associated with a "stirring" action in the material under the tool. Previous work on commercial aluminum alloys [73, 74]. revealed that friction-stir processing resulted in grain refinement and improved local material properties. However, this method cannot produce bulk UFG materials. In a similar approach, materials removed during a machining process have been considered as severely deformed and their potential was examined [75].

Repetitive corrugation and straightening involves bending or corrugating the sample using a special die and then straightening it between two flat plates. As in the ARB technique, repetition of this process helps build up significant plastic strain in the samples. In some cases the samples are immersed in liquid nitrogen before deforming them so as to lower the chances of dynamic recovery and consequently improve efficiency of grain refinement. This technique was used to produce UFG Cu [76].

2.2. Principles of Equal Channel Angular Extrusion

ECAE is carried out by introducing a lubricated billet into a die containing two channels with equal cross-section. For sufficiently long billets, plastic flow is essentially steady and in one plane. The channels intersect at an angle denoted by 2ϕ near the center of the die. The process is described in Fig. 2.1. Under these conditions the billet moves inside the channels as a rigid body, and deformation is achieved by simple shear in a thin layer at the crossing plane of the channels [5, 10, 68]. In this way the complete billet, except the small end regions and the minor surface area is deformed in the same uniform manner. The die angle determines the incremental strain intensity applied as the billet passes through the shear plane [10, 68]. The effective Von Misses strain per pass is given by:

$$\varepsilon = \frac{2}{\sqrt{3}}\cot\phi \qquad (1)$$

The punch pressure needed to press the billet can be determined by:

$$p = \frac{2}{\sqrt{3}} \cdot \sigma_y \cdot \cot\phi \qquad (2)$$

where σ_y is the yield stress of the material [10, 68].

The equivalent percent area reduction (AR) values of ECAE for N passes with respect to conventional extrusion can be found as:

$$AR = (1 - RR^{-1}) \cdot 100\% \qquad (3)$$

In the current study the intersection angle is 90° and the billet is pressed through the die using a servo-hydraulic press. With a die angle of 90°, a true plastic strain of 1.16 and equivalent area reduction of 69% can be reached [68].
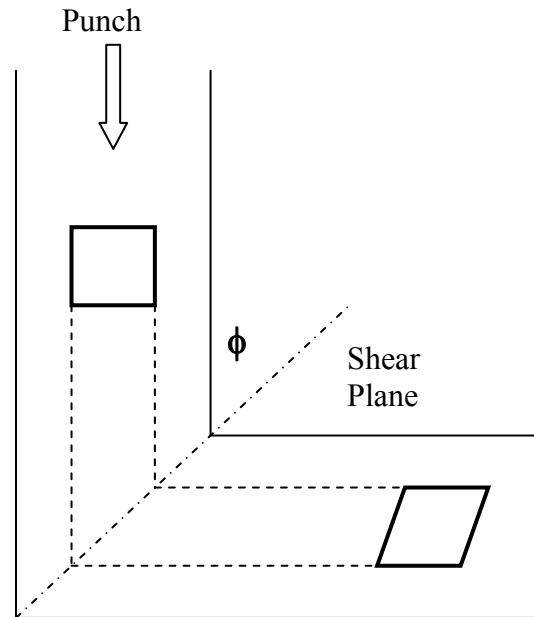
Fig. 2.1. Schematic describing the ECAE process. The representative material element goes through simple shear deformation when passing through the ECAE die.

The most important advantage of ECAE is the development of near uniform, intensive and simple shear in bulk billets in a relatively simple way. The process can easily be repeated a number of times in the same tool and very large effective deformations can be produced without a decrease in billet cross-sectional area. For an ECAE process of N passes, the total strain imposed is [77]:

$$\varepsilon_t = N \cdot \varepsilon$$

Here ε is the effective Von Misses strain per pass as given earlier. Multiple passes can be applied by changing the billet orientation at each step. This results in the modification of the shear planes and shear directions and is important for the creation of special structures and textures.

From the many possibilities, the common routes are described below and shown schematically in Fig. 2.2. These routes contribute to different final shear patterns in the deformed billet which crucial in dictating grain size of the refined microstructure.

Route A: For this sequence of extrusions, the billet orientation is the same at each pass. As a result, the distortion of material elements is continuously increased with each

successive pass. Because all elements are distorted in the same direction, strongly developed laminar grain structures and fiber textures are produced via this route.

Route B: The billet is deformed alternatively in two orthogonal directions $(+/-90^0)$ by rotating about the extrusion axis, meaning counter clockwise 90^0 after every odd numbered pass and clockwise 90^0 after every even numbered pass.

Route C: The billet is rotated 180 ° around its axis after each pass. Material elements are deformed at odd-numbered passes and restored to their original forms at each even numbered pass.

Route B_C: In this sequence, the billet is rotated 90^0 counter clockwise after each pass. This route is the most effective in obtaining highly refined microstructures.

Route E: This is a hybrid route defined that is defined as two route C passes followed by a 90° rotation and then additional two route C passes. This route produces a high amount fully worked material and uniformly refined microstructure with a high fraction of high angle boundaries [78].

N: Number of Passes
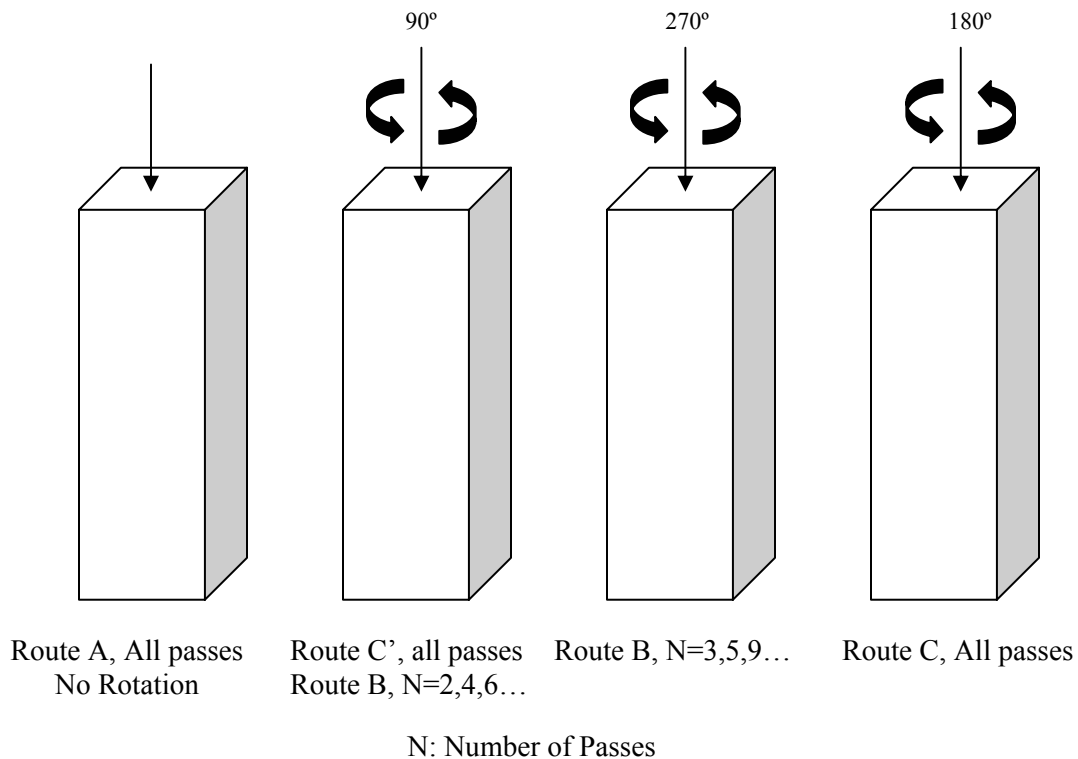
Fig. 2.2. ECAE routes described by respective rotations between each pass.

Usually, in the first ECAE pass many dislocations are introduced within the grain by the high level of applied strain. These dislocations then rearrange into low energy dislocation structures for minimizing the internal energy. In subsequent passes, subgrains with low angle grain boundaries (GB) form inside the original grains by the conversion of dislocation structures. Subgrain boundaries are not clearly defined indicating an instable state. With the increase in number of passes, more dislocations are introduced into these subgrains. These dislocations are absorbed by the subgrain boundaries and eventually increase their misorientation. As a result, low angle GBs evolve into well defined high angle GBs and the level of grain refinement increases [8, 79-81].

Attention has been given to the effectiveness of the various ECAE routes in producing grain refinement in bulk samples of various pure metals and alloys [8, 79, 82-84]. It was found that with the same number of passes, the grain refinement increases and the aspect ratio decreases passing from routes A to B_A to C and to B_C [9, 85, 86]. The aspect ratio represents the grain morphology; grains with low aspect ratio are more equiaxed. These investigations have relied mainly on transmission electron microscopy (TEM) and selected area electron diffraction (SAD) methods as a means of assessing the relative fraction of high-angle boundaries associated with grain refinement. The advantage of following routes with abrupt strain paths stems from the fact that each new strain path produces a dislocation pattern of its own and intersecting dislocation patterns help refining the grain size. With this idea, a few microstructural mechanisms have been proposed. Iwahashi et al. [9] explained the superiority of route B_C among the others by the availability of two sets of intersecting shear planes giving way for grain subdivision. Similarly, Segal [10] indicated that during route B_C shear bands with various orientations forming after each pass construct a spatially uniform network in the material. Zhu et al. [86] suggested that the combinations of shear plane with texture and crystal structure play a significant role in grain refinement. The theory was explained specifically for fcc materials but similar arguments can be deduced for other crystal systems.

Due to the anisotropic characteristics of the microstructure developed in ECAE, one needs to keep track of the specific material plane observed on the extruded billet. The flow plane, transverse plane and the longitudinal plane are indicated by F, T and L respectively throughout this study as shown in Fig. 2.3.
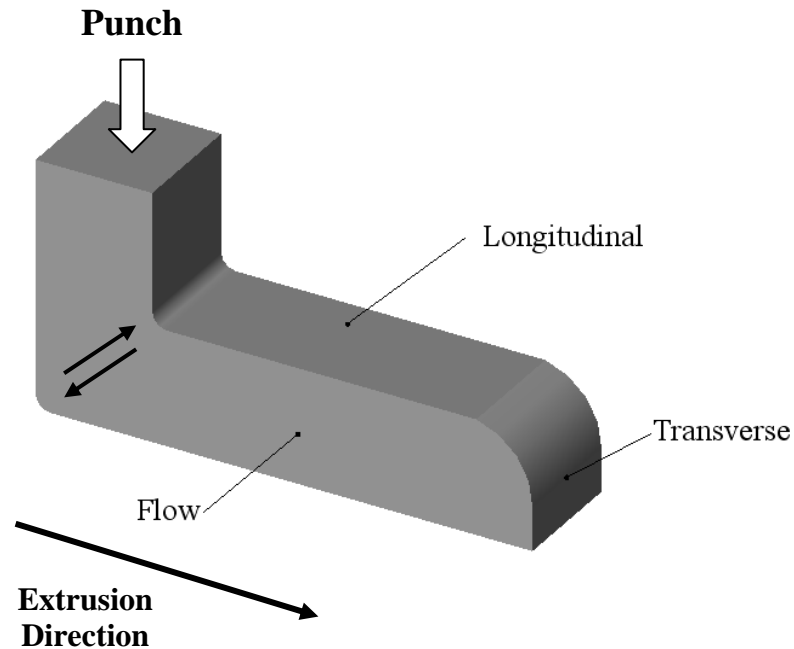
Fig. 2.3. Definition of the deformation planes on an extruded billet.

2.3. Large Strain Deformation Processing and Its Effect on Microstructure

Large strain deformation processing takes advantage of the materials to sustain plastic deformation up to high strain levels. During straining, dislocations commonly organize themselves into mosaic patterns consisting of regions of low dislocation density separated by regions of high dislocation density, which are called dislocation boundaries. These low energy dislocation structures reflect a state of lowest internal energy. The density of dislocations, and the spacing of the boundaries have been used as microstructural parameters related to the flow stress [87]. Microstructures are the result of these heterogeneous distributions of stored dislocations. In general, two types of dislocation boundaries may result from plastic deformation of crystalline materials, which subdivide the grains on two size scales [88]. At the smallest scale of approximately a few microns, statistically stored dislocations subdivide the grains into a cell type microstructure of approximately equiaxed and low dislocation density cells, separated by high dislocation density walls also known as incidental dislocation boundaries (IDBs) as noted by Kuhlmann-Wilsdorf and Hansen [89].

Geometrically necessary boundaries (GNBs) are formed as the result of different active slip systems or different magnitudes of plastic slip among neighboring regions (cell blocks) of individual grains, which leads to the division of grains into cell-blocks [90]. Dislocations stored in these boundaries are the geometrically necessary dislocations needed to accommodate lattice misorientations across the GNBs [88, 90, 91]. For fcc and bcc materials GNBs were formed either parallel to the active crystallographic planes or approximately parallel to the maximum stress direction in the grains. [29, 45, 92]. Tendency of GNB formation can develop depending on the grain orientation as studied in detail by Hansen and coworkers [25, 28, 93, 94]. With increasing strain, misorientation across both IDBs and GNBs increase due to the rotation of cell block to accommodate strain. Generally, the increasing rate of misorientation across GNBs is higher than that of IDBs. Moreover, with deformation, the distance separating GNBs reduce more rapidly than the distance separating IDBs [95]. Factors such as purity, crystal structure, deformation temperature and stacking fault energy (SFE) also influence the development of IDBs and GNBs [96].

A macroscale grain subdivision can also occur in which a single crystal or a polycrystal with large grains is subdivided into deformation bands, consisting of alternate bands with positive and negative lattice rotations. Deformation banding may commence at the initiation of and continue throughout large strain plastic deformation and become the dominant mechanism of grain subdivision [97-99]. As a consequence of this process, adjacent regions of a grain experience lattice rotation towards symmetrically related final orientations. These regions, or zones, of different lattice orientation become ribbon-like in shape during deformation. Material purity, deformation process, and crystallographic texture are the major factors affecting the characteristics of this macroscopic subdivision [100]. For instance, Duggan, et al. [100] have recently investigated the nature and origin of deformation banding in polycrystalline FCC metals. According to these authors, the occurrence of this phenomenon is dependent on the initial grain size and it predominates mainly in coarse-grained materials. The initial grain orientation and rolling reduction are also factors and deformation banding can commence either at the onset of plastic deformation or at some larger strain [101]. Banding is favored by the simultaneous

occurrence of dynamic recovery, which enables the rearrangement of the dislocations in the band interiors into low energy arrays, thereby reducing the stored energy [102].

Directionality of the deformation microstructure caused by the formation of cell blocks, IDBs, GNBs, deformation bands and in the presence of second phase particles; their directionality and voids at the particle–matrix interface was shown to cause flow stress anisotropy [30, 35, 96, 103]. During ECAE, several strain path changes occur and thus during repetitive passes a new imposed strain state would result in the formation of new deformation bands with different orientations. It has been shown that the evolution of microstructure including the length, thickness of the deformation bands and misorientation across them was highly correlated with the route applied [40, 94]. The interaction of newly formed dislocation boundaries and deformation bands with the previously formed ones is effective in refining the microstructure. Additionally, these dislocation arrangements were found to be highly effective in blocking slip depending on their misorientation [30, 35].

2.4. Effect of Processing Induced Microstructure on Mechanical Behavior

As explained in the previous section, plastic deformation causes the formation of dislocation patterns. The morphology of these patterns depends on the material, grain orientation, and the deformation conditions including temperature, strain level and strain rate. The transient flow behavior in between the path changes is affected by how the mobile dislocations gliding during the second strain path interact with the already formed substructure after the initial straining. Old substructures are modified significantly. The modification does not happen instantaneously but rather evolves as the materials are strained following the new strain path causing a transient behavior in the stress-strain curve. By the time the old dislocation substructure disintegrates, and the new substructure starts forming, the material eventually tends towards the monotonic stress-strain curve characteristic of the new strain mode.

Examples of transient behavior have been documented in a number of materials deformed by various strain path change experiments [46, 47, 104]. The most common strain path change tests are cross and reversal tests. The cross tests are achieved when the strain rate vector of the subsequent path is perpendicular to the previous path, while

the reversal tests occur when the strain rate vector of the subsequent path is parallel to the previous path but acts in the reverse direction. The effect of a cross path change on stress-strain response is realized by a spike in the curve and is attributed to the barrier effect imposed on the dislocations gliding on the newly activated slip systems by the old dislocation substructure. A reversal test on the other hand is realized by an initial drop in yield stress followed by a region of zero or low strain hardening and is attributed to the reverse glide of dislocations originally trapped by internal stresses or tangled in the dislocation substructures. As expected, the orientation of the newly activated system heavily depends on the direction of straining and therefore microstructures containing previously formed dislocation boundaries behave differently with different directions of applied strain. This results in an anisotropic mechanical behavior.

2.5. Deformation Mechanisms in Hcp Materials

The two main deformation mechanisms of slip and twinning are in competition against each other when metals deform plastically [41, 105]. The extent of each slip or twinning depends on many intrinsic factors such as crystal structure, SFE, purity and grain size and extrinsic factors such as strain, strain rate and temperature [41]. Deformation by slip occurs on a distinctive lattice plane, where atomic displacements on each plane can ultimately be much larger than the lattice spacing. Gradual crystal reorientation is induced by slip deformation. Slip occurs when shear stress exceeds a critical value for one definite slip plane, and the atoms move an integral number of atomic distances along the slip plane. Slip occurs most readily in specific directions on certain crystallographic planes. Generally, the slip plane is the plane of greatest atomic density and slip direction in the closest pack direction within the slip plane. Since the planes of greatest atomic density are also the most widely spaced planes in the crystal structure, the resistance to slip is generally less for these planes than for any other set of planes. The slip plane together with the slip direction establishes the slip system. The critical value where slip starts on a slip system is called the critical resolved shear stress (CRSS). A dislocation reverses its motion when stress is applied in opposite directions, with a CRSS independent of the sense of its motion [106].

In hcp metals, the only plane with high atomic density is the basal plane (0001). The diagonal axes $<11\bar{2}0>$ are the close packed <a>directions. For Zinc, Cadmium, Magnesium and Cobalt, slip occurs on the (0001) plane and in the $<11\bar{2}0>$ direction. [107]. In contrast, the easy slip system in hcp metals such as Ti and Zr is prismatic slip. Prismatic slip takes place on the $\{10\bar{1}0\}$ planes and in the $<11\bar{2}0>$ directions [1, 108]. The shift in easy slip system for different hcp materials can be explained by the Peierls-Nabarro model stemming from the change in the relative packing densities of prism and basal planes [41, 109]. For c/a ratios less than 1.633 which represents the ideal packing according to the hard sphere model; the relative packing density of the prism planes is higher than that of the basal planes, and the critical resolved shear stress on the prism planes is much lower than that on the basal planes [110].

Table 2.1

Common slip and twinning systems observed in hcp materials.

Deformation Mechanism	Shear Plane, $\vec{n}$	Shear Direction, $\vec{b}$
Prismatic Slip	$\{10\bar{1}0\}$	$<11\bar{2}0>$
Basal Slip	$\{0001\}$	$<11\bar{2}0>$
Pyramidal <a> Slip	$\{10\bar{1}1\}$	$<11\bar{2}0>$
I. Pyramidal <c+a>	$\{10\bar{1}1\}$	$<11\bar{2}3>$
II. Pyramidal <c+a>	$\{11\bar{2}2\}$	$<11\bar{2}3>$
$\{10\bar{1}2\}$ Tension Twin	$\{10\bar{1}2\}$	$<\bar{1}011>$
$\{11\bar{2}1\}$ Tension Twin	$\{11\bar{2}1\}$	$<\bar{1}\bar{1}26>$
$\{10\bar{1}1\}$ Compression Twin	$\{10\bar{1}1\}$	$<\bar{1}012>$
$\{11\bar{2}2\}$ Compression Twin	$\{11\bar{2}2\}$	$<\bar{1}\bar{1}23>$

Other slip systems in hcp metals include <a> slip on first order $\{10\bar{1}1\}$ pyramidal planes, <c+a> slip (along $<11\bar{2}3>$ directions) on first order $\{10\bar{1}1\}$ and second order $\{11\bar{2}2\}$ pyramidal planes. However, pyramidal slip on second order is rare. The possible slip systems available in hcp metals are listed in Table 2.1 along with the common twinning modes. They are also presented in Fig. 2.4. The available slip systems in hcp crystals are generally far from accommodating homogeneous deformation at ambient conditions. Ideally, five independent slip systems are needed to accommodate the homogeneous deformation of polycrystalline materials [111].
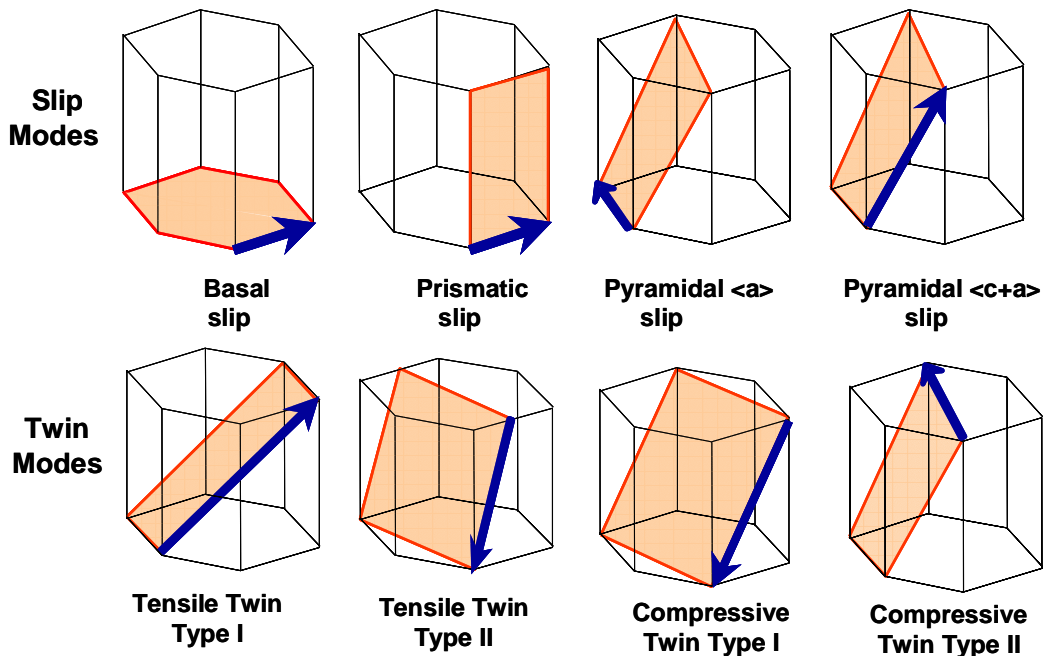
Fig. 2.4. Common slip and twinning systems observed in hcp materials.

Combination of basal <a> slip and prismatic <a> slip provides only four independent slip systems, which is exactly the same as those provided by pyramidal <a> slip [110]. Pyramidal <c+a> slip, which in principle provides the additional independent slip systems, is difficult to activate at room temperature because of its high CRSS [43,

112] and easy dissociation into sessile <c> dislocations to suppress continuous slip [113]. It is also crucial to point that pyramidal <c+a> slip is the only deformation mechanism that can accommodate applied strains along basal poles. At elevated temperature, the activation of pyramidal <c+a> slip and other non-basal slip occurs at lower CRSS, reducing flow stress and increasing formability[114]. The low formability of hcp metals at room temperature mainly arises from the limited number of available deformation systems. Along the same lines, ductility in hcp materials is quite sensitive to orientation.

Deformation twinning on the other hand, is a homogeneous shear evenly distributed over a three-dimensional region. The crystal structure of resulting twins is identical to that of the parent matrix, but with a different orientation [115]. The total shear deformation from twinning is small and limited [105, 115]. A twinning mode is activated only under tension or compression (not both), depending upon the atomic structure. Deformation twins are typically in the shape of thin lenticular plates, as a result of the energetic barriers to the formation of twins [116]. Two main energy factors influence the formation of a twin. One of them is the introduction of a new surface and the resulting surface energy. The other is the strain energy created at the twin-matrix interface due to the plastic shear in the twinned area. The misfit between the matrix and the twin should be accommodated by elastic distortion of the matrix. This naturally requires energy, and is minimized when the twin is narrow and long. It is expected to have high aspect ratio twins when they are formed with a high shear strain. It is found that while fcc and bcc twins are thin, the twins in hcp metals are thicker [105, 117].

Mechanical twinning in metals with highly symmetric crystal structure is less common. Cubic metals, where many symmetrically equivalent slip systems with low CRSS are available, slip is the preferred method of accommodating strain. The occurrence of twinning in bcc metals is favored by the lack of slip activity at low temperature or high strain rate deformation [105]. This can be rationalized by the need of thermal activation to overcome the high Peierls stress in bcc metals, where Peierls stress has a strong negative temperature dependence. The occurrence of twinning in fcc metals is assisted by sufficiently low SFE because twins can be nucleated from stacking faults, according to defect-assisted nucleation theory for twins [118]. Moreover, low SFE suppresses cross slip and prepares conditions favorable for twinning. It was reported that

the stress required for twinning rises with increasing SFE for copper base alloys [118]. Twinning was also commonly observed in low SFE austenitic steels [119-121].

2.5.1. Deformation Twinning in Hcp Materials

Given the fact that limited number of slip systems exist in hcp materials, importance of deformation twinning is even higher in this class of materials. Ductility and formability of hcp metals and alloys are significantly correlated with the operation of twinning. Especially, for extensions or contractions along <c> axes, the need for twinning is much more apparent since pyramidal <c+a> slip is the only available deformation mode that can operate in these instances. Moreover, the orientation changes resulting from twinning may place certain slip system in a favorable orientation and enhance slip activity.

Deformation twins are formed by a homogeneous simple shear of matrix lattice. During the homogeneous shear of matrix lattice, cooperative atom movement occurs [105, 118]. Generally, small motions, called shuffles or reshuffles, of individual atoms are needed to recover original crystal lattice in twins, besides the simple shear. Four kinds of twinning modes are commonly observed in hcp metals as listed in Table 2.1. [41]. The magnitude of shear for each mode is determined by the axial ratio c/a. The relative complexity of atom shuffling for each twinning mode is different and among the four twin modes listed, $\{11\bar{2}1\}$ twins involve the simplest shuffling [122].

The most prominent twinning mode in hcp metals takes place on $\{10\bar{1}2\}$ planes. This twin type operates in all hcp materials [123]. The twinning elements for this twin mode are displayed in Fig. 2.5, where $\{10\bar{1}2\}$ is twinning plane K_1, $<10\bar{1}1>$ is twinning direction η_1, and the plane of shear S is $\{1\bar{2}10\}$. Conjugate twinning plane K_2 and direction η_2 are crystallographically equivalent to K_1 and η_1. K_1 experiences no displacement during twinning, whereas K_2 is rotated. Twinning shear of this mode changes sign at the ideal axial ratio value. For c/a = 1.633, the plane of shear becomes square such that twinning shear becomes zero and no twin of this mode can be formed [122]. Twins in hcp materials have dual character according to the c/a ratio of the hcp

crystal. For instance, the $\{10\bar{1}2\}$ twin helps to extend the crystal along basal poles and thus named as a tension twin for hcp materials such as Zr, Ti and Mg. Whereas, the same twin mode contracts the <c> axes when activated in hcp materials with c/a ratios less than 1.633. In this case, it is named as a compression twin [41].
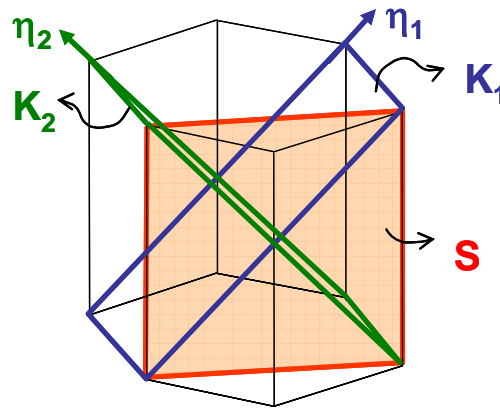
Fig. 2.5. Twinning elements for the twinning mode $\{10\bar{1}2\}<10\bar{1}1>$.

2.5.2. Factors Affecting Nucleation and Growth of Twins

Nucleation and growth of twins are affected by material and deformation conditions like temperature, strain rate, strain level, grain size and impurity level [105, 124, 125]. There is still debate whether the occurrence of twinning depends upon a CRSS, because of conflicting experimental evidence [126-130]. A large scatter in CRSS of Zn single crystals was observed in [129]. They argued that slip is a prerequisite for twinning and thus, no single CRSS can be determined for twinning. It is also suggested that stress for nucleation and growth should be measured differently, due to much lower stress for growth than that for nucleation [117, 124, 131]. Meyers et al. [132] offered a possible explanation for observations in [129]. They argued that the scatter could be due to the stress concentration from surface notches, internal defects, etc., but not from dislocation pile-ups. For many different materials, it has been frequently reported that twinning always occurs on the systems with the highest resolved shear stress [130, 133].

Hence, it is proper to assume that operation of a certain twin mode is dictated by its CRSS.

Twinning generally shows increased activity at lower temperatures due to less increase in the stress required for twinning compared to the increase in the stress required for slip. Decrease in deformation temperature may also lead to the formation of planar dislocations, which reduce the ability of a material to cross-slip causing the early onset of twinning. It is found that twinning stress is not sensitive to temperature for many metals based upon experimental data from the literature, including both single and polycrystals [132]. In contrast, CRSS for twinning was reported to increase with increasing temperature for many fcc and hcp metals [128, 134]. Negative temperature dependence was reported for $\{10\bar{1}1\}$ twinning mode [41].

Twinning stress is very sensitive to strain rate and under shock loading or severe deformation conditions deformation by twinning is frequently observed. Fcc materials with high SFE do not twin under normal conditions, however twinning has been observed in shock loaded Al-Mg alloys at low temperatures. This was attributed to the solid solution strengthening together with the greater increase in flow stress at low temperatures under dynamic loading than stress required to activate twinning [135]. Similarly in pure Zr deformed by the split Hopkinson bar technique readily twinned [136, 137].

The Hall-Petch relation for twinning is similar to that suggested for slip as seen in Eq. (4).

$$\sigma_y = \sigma_0 + k.d^{-1/m} \tag{4}$$

σ_y is the yield or flow stress, σ_0 is frictional resistance to the motion of twins, d is mean grain diameter. Here m depends on the twin thickness and can be as small as 1 [138]. Slope k, the Hall-Petch coefficient, is larger for twinning than for slip [122]. For zirconium it was reported that slope k for twinning was 10 times that for slip [137]. Koike [139] also confirmed that the slope k for twinning was larger than that for slip, by studying AZ31 magnesium alloys of different grain sizes subjected to tension.

Additionally the size of a twin is restricted by the grain size, and shorter twins are observed in refined structures. Small grain sizes tend to suppress twinning nucleation [134, 140]. Lahaie et al. [141] confirmed this by investigating Mg alloys of grain sizes 1

μm and 15 μm subjected to tension and compression. They found that twins were absent in samples of fine-grains (1 μm), while twinning occurred in samples of coarse grains (15 μm). Meyers et al. [142] exhibited this by carrying out shock compression experiments on copper at 35 GPa. Twins were profuse in samples with grain sizes of 117 and 315 μm, and no evidence of twins appeared in samples with a grain size of 9 μm. Furthermore, twin thickness is affected by grain size, with thicker twins accompanying large-grained samples [140].

The chemical composition is also an important parameter, in a sense that it affects the stacking fault energy (SFE) and the mobility of the screw dislocations. Lower SFE values are obtained with the addition of substitutional solute atoms, leading to increased twinning activity [105, 117, 143]. Also, increasing the aluminum or oxygen content in pure Ti impedes mechanical twinning [122, 144].

2.5.3. Twin-Slip and Twin-Twin Interactions

Twinning as an obstacle to slip and growing twins, act in the same way as grain boundaries and cause strengthening. When a twin penetrates a slip band with a high density of dislocations, individual dislocations interact with the twin interface. Inversely, penetration of slip dislocations into a twin forming an obstacle to slip path is also common. A growing twin interacting with a glide line changes the orientation of the slip within the twin due to the twinning shear. It is also possible that the slip dislocations dissociate into other dislocations in the obstacle twin. If the incident dislocations form a pile up pressing against the twin interface, the twins may branch or even fragment. Twin-twin interactions occur when annealing twins or existing deformation twins meet a growing deformation twin. The amount of shear by incident twin transferred beyond the existing twin depends on the interactions taking place. The incident twin (I) can cross the obstacle twin (O) by forming a secondary twin (S) in the crossed region [105]. Two conditions are necessary for this to happen as explained by Cahn [117]. The K_1 planes of I and S must intersect that of O in the same direction and the direction η_1 the magnitude and sense of shear in I and S must be the same. Both twin-slip and twin-twin interactions may be responsible for microcracks formed in the vicinity of the intersections due to high stress levels.

2.6. Crystallographic Texture

During deformation processing, grains rotate towards stable orientations. For instance, it is known that in tension, the tensile axis tends to rotate towards the slip direction, while in compression the compression axis rotates towards the slip plane normal. Thus, deformation processing is a major source of crystal rotation to a preferred orientation. The grain reorientations also take place during recrystallization of the deformed material with the resulting textures referred to as annealing textures [145, 146]. The presence or absence of a preferred or common orientation among numerous grains in the material defines the crystallographic texture. Properties that are affected strongly by the presence of texture are Young's modulus, yield strength, Poisson's ratio, ductility, toughness, magnetic permeability. Deformation texture is dependent on crystal structure, chemical composition, the nature (strain path), rate, amount and temperature of the deformation [146, 147].

The most common method to represent crystallographic texture is to present the orientation distribution of crystallographic planes either in specimen reference frame or in crystal reference frame. In the specimen reference frame, the crystallographic distribution is called a pole figure showing the relative intensity of all diffracting planes along a particular sample direction. In the crystal reference frame, the distribution of the crystallographic intensity is called an inverse pole figure showing the variation in pole density of one particular set of crystallographic planes [146, 148]. A pole figure is constructed assuming that pole intensities of the materials for a given orientation are proportional to the volume fractions of that orientation, and that the pole intensities are proportional to the measured signal intensity [146, 148].

The last method of texture representation is the orientation distribution function (ODF). This representation of orientations is typically prepared by plotting three Euler angles, φ_1, Φ and φ_2, in a rectilinear coordinate system, which represents rotation angles needed to reorient the cube axes of the lattice into coincidence with the reference axes. The Euler angles are defined using Bunge's convention [146]. Thus, φ_1 is the first rotation and it is about the x3 (or Z) axis; the second rotation, Φ, is about the x1 (or X) axis; and the final rotation, φ_2, is also about the x3 (or Z) axis. The ranges of the Euler angles necessary to represent all possible orientations depend on lattice symmetry.

The textures of cold rolled hcp materials can be categorized into three groups according to their c/a ratios. For c/a ratio greater than 1.633 such as zinc and cadmium, textures with basal poles tilted 15° to 25° away from the normal direction toward the rolling direction are exhibited. For c/a ratios close to 1.633 such as magnesium or cobalt, [0001] fiber textures tend to form. For c/a ratios lower than 1.633 such as zirconium and titanium, textures with basal poles tilted 20° to 40° away from the normal direction toward the transverse direction and [1010] poles are aligned with the rolling direction [1, 146, 149]. Additionally, hcp metals are known to develop a simple $<10\bar{1}0>$ fiber texture that is parallel to the axi-symmetric direction during wire drawing and extrusion at low temperatures [97, 146].

Torsion textures demonstrate the lattice orientation under simple shear and therefore gives insight about texture formation after ECAE. For fcc materials three different ideal orientations for shear texture have been proposed[146, 150]. The torsion textures are generally visualized in the coordinate system composed of shear direction, radial direction and shear plane normal. The 'A' partial fiber can be indexed as {111}<uvw>, the 'B' partial fiber as {hkl}<110> and the 'C' orientation as {001}<110>. The 'C' position is a special variation of the 'B' fiber texture. Recent work revealed the existence of another fiber. In the [111] pole figure it appears similar to the 'A' fiber but is rotated 90° about the pole figure center. One particular component, which is sometimes predominant in this 'D' fiber, is {112}<110>.

Variation of torsion texture with material has been investigated. It has been shown that high stacking fault energy materials such as nickel and copper exhibit a strong 'B' fiber and a weak but non-zero intensity 'A' fiber texture [146]. For silver, similar B fiber texture exists and the A fiber is absent and replaced by the 'D' fiber. The strength of the 'D' fiber is dominated in Ni60Co. For copper deformed at 400 ^{o}C, it is seen the dominant fiber 'A' is replaced by 'D' [151].

Much less research has been carried out regarding the torsion texture development of bcc materials. One prominent example studied the texture development of IF steel stabilized with Ti and Nb during room temperature torsion tests both experimentally and theoretically [152]. Similarly, there is very limited literature regarding the torsion texture of hcp materials. Torsion textures for hcp metals in tube form are dependent on the ratio

of the reduction in wall thickness (R_w) to reduction in diameter (R_i). For $R_w/R_i = 1$, the texture is similar to a fiber texture whereas, for $R_w/R_i > 1$, the texture is similar to a rolling texture [146, 147]. Recently, Sanchez et al. [153] focused on the texture development of Zircaloy during fixed end torsion tests at 750 ^{o}C. The basal pole figures indicated an approximate fiber rotated from the shear direction in the counter clockwise direction around the radial direction.

2.6.1. Texture and Anisotropy

A single crystal is characterized by the periodic arrangement of atoms or in space. This always generates a dependence of the crystal properties on the chosen direction, which is called anisotropy of the single crystal. The anisotropy of a polycrystalline material considerably depends on the preferred orientations of the enclosed crystallites. There can be two extreme cases. On one side, all crystallites might have the identical orientation. Then the anisotropy of the polycrystal equals to that of the single crystal. On the other side, all orientations might occur with the same probability. Then the behavior of the polycrystalline material is isotropic even though every single crystallite shows an anisotropic behavior [146, 148, 154].

Textured materials where there is a tendency for certain preferred orientations exhibit anisotropic mechanical and physical properties. Mechanical anisotropy of a textured metal is usually described by the ratio of the true strains along the width to thickness directions in uniaxial tensile test. This ratio is a measure of resistance of the material to contraction in its thickness direction and is called the Lankford coefficient. If it is less than 1, the material contracts more in thickness than in width, and material with ratio greater than 1 exhibits a higher resistance to wall thinning. This parameter defines the resistance to wall thinning of an anisotropic material and thus control the formability which is of importance to the material manufacturers [146, 148].

Mechanical testing for plastic anisotropy after deformation processing involves reloading the processed metal in different directions and recording yield strength. The experimental methods for characterizing the mechanical anisotropy depend on the geometry of the material and are based on either the stress formulation or the contractile strains. An evaluation of the flow stresses along the three orthogonal directions can be

used in the Hill's quadratic yield function for the generalized stress [155, 156]. Alternatively, if the principal stress directions are coincident with the anisotropy axis, the shear terms are zero. Then, a direct evaluation of lateral contraction following longitudinal tensile plastic deformation along different angles to the rolling direction would yield R and P, respectively, as a function of the major tensile strain.

However, anisotropy in mechanical response is not limited to difference in plastic flow along different straining directions. For a given direction of straining, there is a positive and negative sense, for instance, compression and tension testing along the sample's long axis. Firstly, especially for hcp materials twinning mode depends on the sense of loading. Secondly, each sense, compression or tension or shear, imposes a different type of strain path change and hence can lead to a different flow response due to the effect of processing induced microstructure on the newly activated dislocations as mentioned previously.

2.7. Polycrystal Plasticity Models

Polycrystal models represent materials by an aggregate of crystals or grains with preferred orientation distribution, called crystallographic texture as defined previously in this Section 2.6 [146]. Each grain deforms based on crystal plasticity, where slip and twinning mechanisms are activated to accommodate imposed deformation. Interaction between grains are modeled by Full Constraints (FC) [157], Relaxed Constraints (RC)[158], or Self Consistent (SC) [159] approaches.

No interaction is considered in the FC approach, because of the enforcement of homogeneous deformation. Homogeneous deformation is provided by the activity of minimum five independent slip systems. The FC approach can result in high stress discontinuity and preference over large CRSS deformation mechanisms in hcp materials. This causes the deviation of predicted texture from experimental observations, as revealed by analyzing the plastic anisotropy of rolled zircaloy-4 [160]. The FC approach is mainly employed to model the plastic response of cubic metals with small to mild plastic heterogeneity.

In the RC approach, three independent slip systems are required for flat grains to accommodate arbitrary deformation, where both shears on the flat plane are not required

and therefore are relaxed [111, 158]. These strain components are relaxed at the expense of forcing the corresponding stress components in each grain to be in equilibrium. The relaxation of required slip systems introduces better prediction of slip and twinning activity than the FC approach, because the local boundary conditions acting upon flat grains are better represented [157]. Therefore, prediction of texture evolution at large strains is more reasonable in RC approach.

The aggregate behavior in polycrystal models is represented by a collection of orientations. Each orientation represents all the grains oriented in that orientation. In the SC approach, each orientation is treated as an inhomogeneity embedded in the aggregate, while the aggregate is represented by a homogeneous effective medium (HEM). The properties of the HEM are uniform and are not known as a priori. Self consistent (SC) means that the imposed external stress and strain should be consistent with the average of the aggregate. Interaction between an orientation and the HEM is given explicitly, depending on the applied stress, the overall response of HEM and the orientation itself. This is provided by an interaction equation that relates the stress and strain rate deviations of a grain with respect to the respective macroscopic averages. Because the neighborhoods of all grains with the same orientation are identical, topology, localization, and correlation effects are not addressed properly in the SC approach [146].

2.7.1. Viscoplastic Self -Consistent Modeling Framework

The viscoplastic self-consistent (VPSC) approach is an application of the SC approach[42]. In VPSC, the initial texture, the hardening parameters in single crystal level, and the imposed boundary conditions are specified by users. Dislocation slip is represented by a rate dependent constitutive law. Deformation is simulated by imposing successive incremental steps. The texture is represented by weighted orientations, where a weight denotes the volume fraction of those grains oriented in the same orientation. The interaction of each grain with its surroundings is addressed explicitly by considering the anisotropy of both grains and surroundings, by means of a self-consistent method and a modified (viscoplastic) Eshelby equivalent inclusion approach [159, 161].

The VPSC approach is advantageous in comparison to other classical methods in terms of providing a degree of adjustment to grain-matrix interaction. VPSC can be

thought of as a balance between the FC and the RC models enabling a more realistic approach by treating each grain as an ellipsoidal inhomogeneity embedded in and interacting with a HEM representing the aggregate. The formulation results in an interaction equation that relates the stress and strain rate deviations in the grain with the overall stress and strain rate of the homogeneous aggregate. This enables the model to account for deviations in the grain behavior from the average behavior of the polycrystal. VPSC also accounts for the plastic anisotropy of each grain; each grain is allowed to deform differently depending on its morphological and crystallographic orientations with respect to the surrounding HEM. Typically, grains unfavorably oriented for accommodating an imposed strain will deform less than those favorably oriented. This is especially important in modeling the texture evolution of low symmetry crystals such as hcp [42, 162]. The details of the present VPSC model can be found in literature [42, 159, 161, 163, 164].

Deformation in VPSC is handled according to the evolution of critical resolved shear stresses (CRSS) for each slip or twinning mode. Each CRSS evolves with the accumulated strain in each grain according to an extended Voce law [165] covering hardening stages II through IV.

$$\tau_V(\Gamma) = \tau_0 + (\tau_1 + \theta_1\,\Gamma)\big[1 - \exp(-\theta_0\Gamma/\tau_1)\big] \tag{5}$$

where τ_0, τ_1, θ_0, θ_1 are material parameters and Γ is the accumulated shear in a grain at time t: τ_0, $(\tau_0 + \tau_1)$, θ_0, θ_1 are the initial CRSS, back-extrapolated CRSS, initial hardening rate and asymptotic hardening rate, respectively.

$$\Gamma = \int_0^t \sum_s \left|\dot{\gamma}^s\right| dt \tag{6}$$

Additional coupling between slip and twin systems are introduced via latent hardening.

$$\dot{\tau}_h^{\alpha} = \frac{\partial \tau_V}{\partial \Gamma} \sum_r h^{sr}\dot{\gamma}^r \tag{7}$$

In equation (3) h^{sr} indicates the hardening of systems s due to shear rate taking place in system r. For the specific case of s as a slip system and r as a twin system; h^{sr} corresponds to the interaction between a slip and twin system and reflects the strengthening in a slip system s due to the barrier effect imposed by twin system r. Thus,

the latent hardening parameters coupling slip and twin systems are generally selected to be considerably higher than the ones representing slip-slip interactions.

Twinning is accounted for by utilizing a predominant twin reorientation (PTR) scheme in the present model [166]. PTR scheme defines the real volume fraction of twinning for a total of r crystals in the polycrystal aggregate as [166]

$$f_R = \sum_r f^r \sum_{t_i} (g^{r,t_i} / s^{t_i}) \qquad (8)$$

where g^{r,t_i} is the accumulated twinning shear associated with each twinning system t_i over the deformation steps in each crystal, s^{t_i} is the characteristic shear of the twin system and f^r is the volume fraction of the crystal in the aggregate. Whenever a whole crystal is reoriented by twinning, the effective twin volume fraction is updated as

$$f_E = \sum_r f^r \Delta^r \qquad \Delta^r = 0 \text{ when the crystal is untwinned}$$
$$\Delta^r = 1 \text{ when the crystal is twinned} \qquad (9)$$

At every deformation step, the fraction accumulated in the individual twinning systems of each grain $g^{r,t_i}/s^{t_i}$ is compared with a threshold value f_T that follows the empirical relation

$$f_T = A_1 + A_2 \frac{f_E}{f_R} \qquad (10)$$

where A_1 and A_2 can be determined from single crystal experiments or fitted to a known polycrystal response with known internal parameters. Eq. (10) prevents grain reorientation until a threshold value A_1 (around 10-20% grain volume) is accumulated in a twin system and then raises the threshold to A_1+A_2 (around 40-60% grain volume). The characteristics of this scheme are that it favors the reorientation of crystals using the most active twinning systems. In addition, the self-adjusting nature of the scheme guarantees the reoriented volume fraction, f_E to coincide with the real volume fraction, f_R. Whenever f_E is larger than f_R, the threshold f_T increases and inhibits further reorientation by twinning until the real volume fraction catches up with the effective one [166]. This approach results in the formation of twin fractions consistent with the shear activity of twins.

CHAPTER III
EXPERIMENTAL METHODS

3.1. Initial Materials and Processing Details

The as-received materials used in this study are listed below.

Commercial purity (CP) Grade 2 Ti (composition wt%: 0.15 O, 0.006 N, 0.002 H, 0.041 Fe, 0.008 C, Ti balance)

CP Grade 4 Ti (composition wt%: 0.3 O, 0.009 N, 0.0028 H, 0.206 Fe, 0.012 C, Ti balance)

Ti-6Al-4V (Ti64) Alloy (composition wt%: 6 Al, 4 V, 0.4 Fe, 0.1 C 0.05 N, 0.02 O, 0.015 H, Ti balance)

High Purity Zr (composition wt ppm: 35 Hf, 50 Fe, 20 Al, 50 V, 50 O, 20 N, 22 C)

ECAE of the above materials were carried out following different processing routes, temperatures and deformation rates. The details regarding the processing schedules for each material are presented in its respective chapter. Different extrusion temperatures were necessary to achieve ECAE at minimum possible deformation temperatures for different temperatures. Higher extrusion temperatures were necessary for Ti64 due to its limited ductility, whereas high purity Zr was extruded without localization at room temperature.

The as-received Ti bars were coated with a graphite base lubricant before extrusion. Ti64 rods with 10 mm diameter were placed in 25.4×25.4 mm cross section stainless steel cans before extrusion. Ti and Ti64 billets were heated in a furnace to the deformation temperature where they were held for one hour before extrusion and 30 minutes in between ECAE passes. Billets were transferred to the 25.4 × 25.4 mm cross section, 90° angle ECAE die which was preheated to 300 °C for extrusion. Extruded billets were quenched in water. Zr bars in contrast were extruded at room temperature. Prior to extrusion, bars with a cross section of 8×8 mm cut from the clock-rolled and annealed plate were inserted into 25.4×25.4 mm cross section nickel cans and extruded for a single pass. Shielding the extrusion materials (Ti64 and Zr) with cans was done to prevent shear localization, to minimize tool wear, to conduct a smoother extrusion yielding uniformly deformed billets and due to die inlet channel dimensions

3.2. Microstructure Evaluation Methods

Optical microscopy (OM), scanning electron microscopy (SEM) and transmission electron microscopy (TEM) are the main methods used to investigate the microstructure of the as-received and as-processed research materials. Optical microscopy has only been utilized to investigate as-received microstructures. Due to the high dislocation density and the refined grain size of the as-processed materials, SEM and TEM are utilized for microstructural investigations. All OM samples were mechanically ground down to 1200 SiC grit. Ti64 samples were polished with 3 microns and 1 micron diamond paste and then with 0.05 micron alumina powder, sequentially. They were chemically etched with Kroll's reagent (3 ml HF + 6 ml HNO_3 in 100 ml distilled water). Polishing of pure Ti samples was carried out in two steps by first using 9 microns diamond suspension and then 0.05 micron colloidal silica mixed with 30% H_2O_2. Etching was also carried out with Kroll's reagent. OM for Zr samples followed a similar polishing schedule as for Ti and they were etched with a solution of 45 H_2O : 45 HNO_3 : 10 HF before examination.

SEM was used to examine the microstructure of ECAE processed and annealed Zr. Characterization was held in an FEI XL30 SEM. Specimens were mechanically ground down to an 800 grit SiC finish and chemically polished with a solution of 45 H_2O : 45 HNO_3 : 10 HF. For Ti64, TEM investigations were carried out in a JEOL 2010 microscope operated at a nominal voltage of 200 kV. Samples were prepared by grinding, mechanical polishing of slices down to 100 μm and punching 3 mm diameter thin foils. Thin foils were twin-jet electropolished with a 20 vol. % H_2SO_4 in a methanol solution before examination. Ti samples were examined using a Philips CM200 microscope operated at a nominal voltage of 200 kV. TEM foils which are prepared by grinding and polishing down to 100 μm were electropolished with a 5 vol. % $HClO_4$ in methanol solution. Zr samples were also examined in a Philips CM200 microscope operated at 200 kV. The same electropolishing recipe for Ti is used to prepare the thin foils for Zr.

3.3. Crystallographic Texture Measurement
3.3.1. X-Ray Diffraction

After metallographic preparation, samples are mounted on the texture goniometer, which simply is a rotating and tilting stage. A sample thickness of 1 mm and 10 mm×10

mm area is generally sufficient for reliable measurements. In addition, for ECAE processed samples, the sample has to be cut from the uniformly deformed region of the billet, and it has to be marked showing the extrusion direction. First, a θ-2θ scan is done to determine the exact position of the peaks. Then the source and the detector are positioned for reflection from one particular set of planes, i.e. a certain pole. This is followed by rotating the sample about two mutually perpendicular axes, namely parallel to the plane of the sample and normal to the plane of the sample. The tilting of the sample is between 0° to 85° in the reflection measurement mode. This is done to obtain the concentration of that specific pole in different directions with respect to the sample axes. The sample may be oscillated in its plane to have a scan over a relatively large area, up to about $1cm^2$ [146]. Measuring texture with x-rays has both advantages and disadvantages which are summarized below.

X-Ray Diffraction (XRD) can be used to give a picture of the overall or macro-texture especially with sample oscillation. It provides better statistics as compared to orientation imaging microscopy (OIM) techniques due to its higher depth of penetration. Sample preparation is relatively easy and measurements are relatively fast. One pole figure can be acquired in between one to two hours. As for the disadvantages, the reflection method provides orientation information up to an angle of 85° from the center of the pole figure. The remaining 5° has to be completed by a software, the most common being popLA, using information about sample symmetry, crystal symmetry, and other pole figures. Otherwise, a transmission method has to be used to complete the outer ring of the pole figure.

Additionally XRD cannot give information about microtexture, i.e. preferred orientation in a very small area of the order of a few hundred microns. This prevents to obtain the orientation of individual grains and misorientations between adjacent grains, or orientation changes at grain boundaries and twin boundaries. Moreover, it cannot show the orientations of micro-constituents in a multiphase material. The X-ray texture measurements in this study were conducted by a Philips X'Pert system with Cu-Kα radiation. The pole figures were completed and plotted using the popLA package [167].

3.3.2. Neutron Diffraction

Neutron diffraction is also used to study crystallographic texture for an average macrotexture in a similar way to that of x-rays. Compared to the x-ray diffraction, interaction of neutrons with shell electrons is much weaker, and therefore, there is much lower absorption and much higher penetration depth for neutrons. There are some advantages for neutron diffraction. Firstly, because of resonance scattering, different isotopes of the same elements may have different scattering amplitude and can be separated by neutron diffraction. Secondly, since light elements are of similar scattering magnitude to those of heavy elements, neutron diffractions are also used for light element detection. In addition, since the depth of penetration is very high, there is no need for metallographic preparation. However due to the limited availability of the neutron sources neutron diffraction is only used for texture studies for which XRD is not effective. Such as in the need of greater depth of penetration or in the case of irregularly shaped, large grained specimens, specimens with small volume fraction of second phases, porosity, low crystal symmetry, and multiphase system [146, 168, 169].
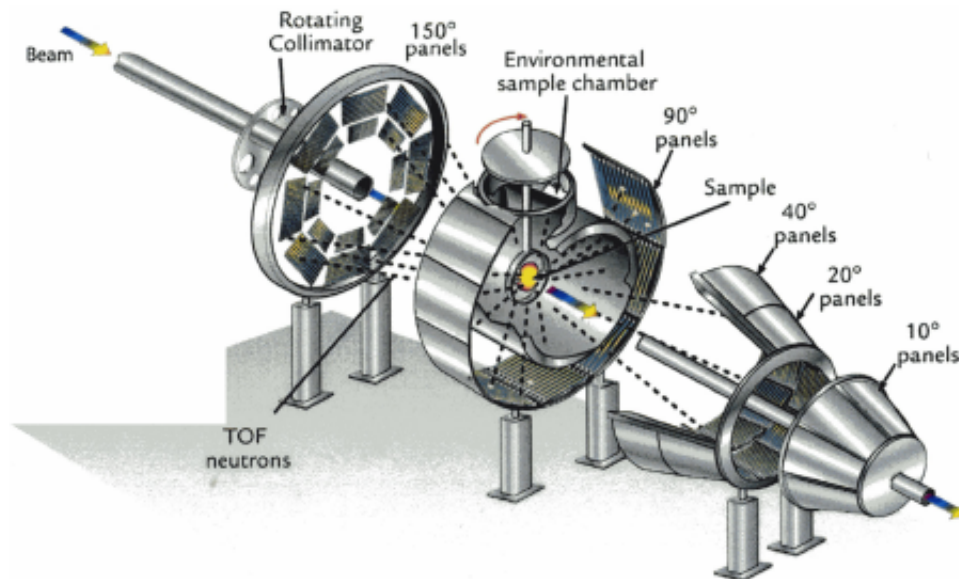
Fig. 3.1. The HIPPO diffractometer used for the neutron diffraction texture measurements at Los Alamos Neutron Science Center (LANSCE) [170].

The texture measurements in this study were performed in the High Pressure Preferred Orientation (HIPPO) diffractometer at the pulsed neutron source of the Manuel Lujan Jr. Los Alamos Neutron Science Center (LANSCE) [170]. Fig 3.1 explains the neutron flight path at HIPPO. No metallographic preparation was necessary for measurements. Samples with dimensions of 4 mm x 4 mm x 8 mm were placed in the chamber and measurements were conducted at room temperature. Due to HIPPO's large detector coverage, rotation around the vertical axis is sufficient to obtain an orientation distribution function (ODF). Total neutron beam time was about 60 minutes per sample orientation at an average proton current of 100 microamperes. 98 histograms obtained from four different sample orientations for diffraction angles of 150°, 90° and 40° were refined using GSAS software to obtain the given ODF using a spherical harmonics approximation [171]. From the ODF, individual pole figures were recalculated. 8th order spherical harmonics description of the ODF was sufficient to describe the data. No sample symmetry constraints were imposed on the analysis. Pole figures were plotted using the popLA package [167].

3.3.3. Electron Backscatter Diffraction

The backscattered electrons from a specimen, which is placed in a conventional SEM and tilted to an angle of about 70° from the horizontal, are captured on a phosphor screen of an electron backscatter diffraction (EBSD) camera. A background is measured over a relatively large area. This background is subtracted from the backscattered pattern and the resultant Kikuchi pattern is captured. The Kikuchi bands are analyzed using a computer software to determine the orientation of the crystal at that point. Each pattern is analyzed several times, and resulting solutions, in the form of the Euler angles φ_1, Φ, and φ_2, are then ranked in the software. The pattern is then assigned a best-fit solution and an indication of the quality of the solution, which is called the Confidence Index (CI) [172, 173].

A schematic diagram explaining the geometry of the electron backscattering diffraction is shown in Fig. 3.2. The three important parameters necessary to calibrate the Kikuchi patterns and hence to index the patterns are; specimen to screen distance, specimen tilt angle and specimen height or working distance in the camera. For general

EBSD work the specimen to screen distance is fixed. Tilting the sample is required to reduce the path length of the back-scatter electrons in the sample and thus to improve pattern contrast, but tilting beyond about 80° causes excessive anisotropy of the sampled volume and distortion of the uncorrected image. An angle of about 70° is a good compromise between image contrast and anisotropy of the sampled volume. A beam scan may be done over areas of the order of 5-500 μm^2 with a step size of 0.01 μm and above, which yields a detailed "orientation map" of the scanned area. Therefore, the method is sometimes referred as orientation imaging microscopy (OIM) [172, 174]. A stage scan can be used to scan a larger area of the order of 10mm^2.

The main advantage of EBSD is that it can give information about the orientation of, and misorientation between, individual grains, orientation relationships between two phases, rotation or tilt angle at grain and kink boundaries (grain boundary character distribution). Demonstration of grain boundary character distribution is of paramount importance in UFG materials [94]. Since UFG materials generally develop their grain structure from well developed dislocation cell boundaries, using the EBSD technique can provide valuable information regarding the evolution of the microstructure.
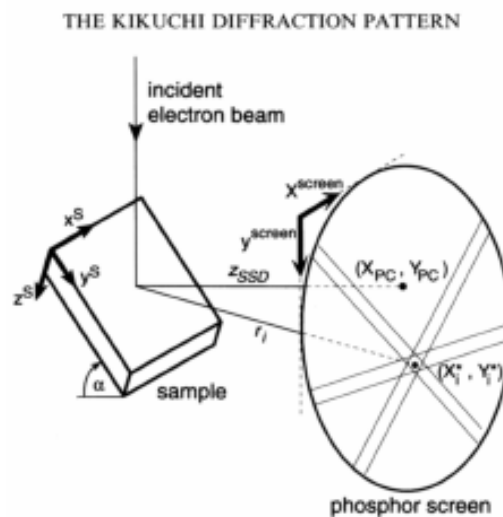
Fig. 3.2. Formation of Kikuchi bands on the phosphor screen used in an EBSD system [173].

Moreover, from only one scan, complete pole figures for any pole can be obtained. This is because the method analyzes the Kikuchi patterns to calculate the full orientation of a crystal at the point where the beam strikes. If a scan is carried out over a fairly large area, macro-texture can also be obtained. However this might take several hours increasing the time and monetary cost of the acquisition. Since EBSD collects signals from a surface layer of a few nm only, it does not give statistical information through the depth of the sample. Moreover, great care has to be taken in sample preparation so as to get an extremely smooth surface (roughness about 0.05 μm) without causing subsurface deformation which would cause the Kikuchi patterns to be very hazy [172, 174].

Similarly, utilizing EBSD on severely deformed materials is challenging due to the very high dislocation density present in the microstructure. Therefore, generally short time annealing treatments might be necessary before observation. Using EBSD on severely deformed materials requires a very tedious metallographic preparation. The OIM maps from the ECAE processed and annealed Zr samples were acquired using FEI XL30 SEM equipped with a TexSEM Laboratories (TSL) data acquisition system. Annealing at 400 $^\circ$C for 1 hr was necessary to decrease the dislocation density and acquire indexable patterns. The orientation data was analyzed using TSL OIM analysis software. Samples for EBSD were prepared using the same recipe as described for their SEM observations previously.

3.4. Mechanical Testing

Mechanical behaviors of the as-received and as-processed samples were explored using an MTS 810 servo-hydraulic test frame controlled with a Teststar II system. The tests were conducted using displacement control during loading and force control during unloading. Monotonic tension and compression tests were performed at the quasi-static strain rate regime (10^{-4} to 10^{-3} s^{-1}). The tension samples had a dog-bone shape with a gage section of 1.5 mm x 3 mm x 8 mm. The compression samples were rectangular blocks with dimensions 4 mm x 4 mm x 8 mm. The sample dimensions are presented in Fig. 3.3. and they were cut into the respective shapes by using wire electro-discharge machining (EDM). Before the experiments, the samples were ground and polished to remove the

residue layers formed during EDM. Especially for compression samples, the surface flatness is very critical for reliable axial compressive experiments. Also, Teflon tapes were used for lubrication between the compression platens and the specimen surface to reduce frictional effects. Strains were measured using a miniature 3 mm gage length extensometer directly attached onto the gage sections of the specimens. Experiments were repeated on two to three companion specimens to check repeatability.

DIA 1.56 mm
2X DRILL
THROUGH

9.00 mm

3.00 mm

8.00 mm

R2.00 mm

3.50 mm

3.50 mm

7.00 mm

7.00 mm

Thickness: 1.50 mm

8.00 mm

4.00 mm

Thickness: 4.00 mm
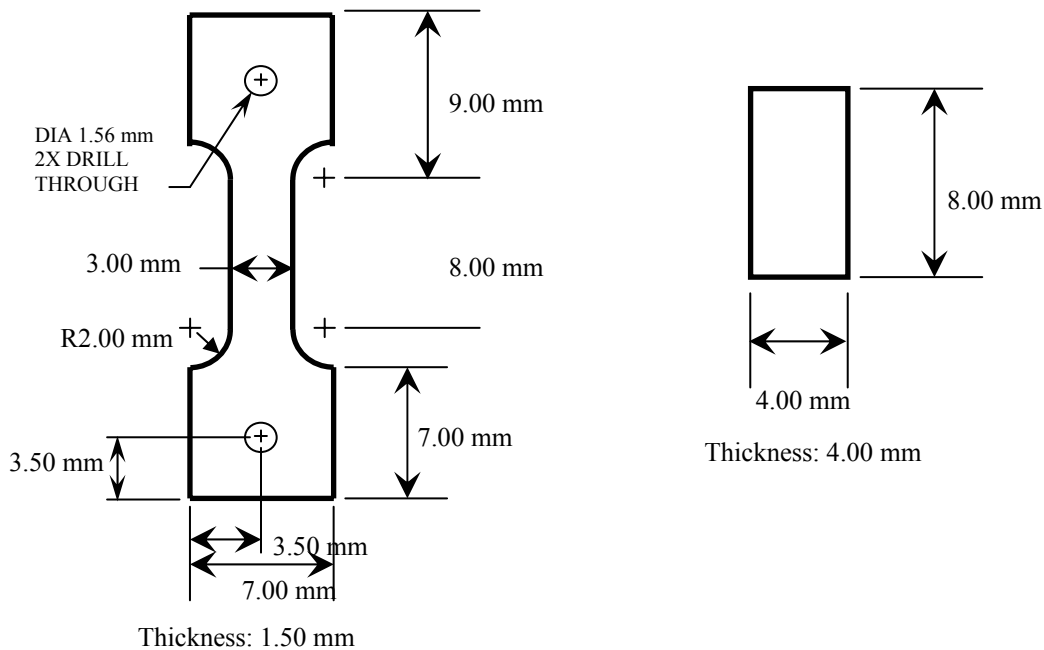
Fig. 3.3. Schematics showing the dimensions of the (a) tension and (b) compression samples used in this study.

A digital image correlation (DIC) system was used during certain Zr compression experiments. DIC is a technique that compares digital images of a specimen surface before and after deformation to deduce its two-dimensional surface displacement field and strains [175]. It consists of recording the images during an experiment using a CCD camera and post-processing them in a computer. To minimize intensity change during the experiment, directed light sources were used to illuminate the specimen. The DIC method works best when the starting image contains a random pattern that can carry the specimen

deformation exactly. To create such a random pattern on the current specimens, spray paint was used. First white paint provided a bright background and then black spray paint gave a high contrast speckle pattern. The black paint was applied by spraying parallel to the specimen surface and letting paint droplets fall randomly on the specimen. In addition, since the field of view of the CCD camera is fixed and only the lower grip of the load frame moves, the region of interest on the specimen has a significant upward displacement. Thus, the size of the specimen must be carefully chosen to ensure that enough portion of the originally undeformed image remains inside the camera's field of view for all subsequent deformation.

CHAPTER IV

EFFECT OF STRAIN PATH CHANGES ON THE MICROSTRUCTURE, TEXTURE AND FLOW BEHAVIOR OF UFG PURE TITANIUM

4.1. Background

Commercial purity titanium has a hexagonal close packed (hcp) structure with a c/a ratio, also called the axial ratio, (1.587) less than the ideal (1.633). The axial ratio of hcp materials dictates the relative packing density of the prism planes. This in turn affects the ratio of critical resolved shear stresses on the prism and basal planes. It is also important in identifying the sense of shears in active deformation twinning systems [41, 105].

Titanium and its alloys are used in many applications ranging from aerospace to biomedical; however the use of commercial purity Ti has been limited due to its comparably low strength. Pure Ti, especially in biomedical applications, presents an advantage owing to its good corrosion resistance, higher inertness and biocompatibility. Pure Ti has been processed using a number of SPD techniques to produce UFG microstructures leading to enhanced physical and mechanical properties [13, 176-178]. Even though SPD alone is a viable method for improving strength levels [13, 85], many engineering applications require higher strength combined with high ductility. In this respect, there are a number of studies where the severely deformed pure UFG Ti is subjected to a second thermo-mechanical treatment step to further increase the strength levels with better ductility [176-178]. Generally, this second step consists of a conventional deformation method with suitable post deformation heat treatment.

Stolyarov et al. investigated the grain refinement and corresponding mechanical properties in pure Ti subjected to ECAE [85], ECAE followed by cold rolling [176] and ECAE followed by cold extrusion [178]. All extrusions in these studies were carried out in a temperature range of 400 to 450 °C. They found out that route B_c led to the formation of an equiaxed and effectively refined microstructure [85]. Further cold rolling and cold extrusion resulted in improved yield and tensile strengths, the former with higher strength levels [178] They also presented the mechanical properties of ECAE processed Ti parallel and perpendicular to the extrusion direction. Although the observed anisotropy

was attributed to the texture formed after ECAE, they did not elaborate on the interplay between texture and resulting mechanical properties [85]. Bengus et al. [179] also reported asymmetric response during compressive straining of eight pass ECAE processed pure Ti, parallel and perpendicular to the extrusion direction. Higher compressive yield strength in samples perpendicular to the extrusion direction was explained by the effect of strong texture on the active deformation mechanisms. However, they neither mentioned the ECAE route applied nor did they carry out texture measurements. In another study, the discrepancy in mechanical behaviors observed during straining of ECAE processed Ti parallel and perpendicular to the extrusion direction was attributed to the different mobility of grain boundary dislocations in the two cases as opposed to the crystallographic texture effect [180]. Given these controversies, there is a clear need for a systematic study revealing the mechanisms behind the observed flow anisotropy in SPD processed Ti.

Texture evolution after ECAE has been studied in a number of hcp materials such as pure Ti and Zr and Mg alloys [181-184]. Among these, the ones focusing on Ti clearly presented strong texture formation after various ECAE routes [181-184]. Nevertheless, these studies lack discussion on the relationship between texture and resulting mechanical properties. Although the microstructure of ECAE processed plus rolled pure Ti has shown to be anisotropic [177], its effect on flow properties has not been studied. The present study aims to fill this gap by demonstrating the effect of orientation on tensile properties of the lower temperature ECAE processed plus cold rolled Ti and investigating the underlying mechanisms causing notable flow anisotropy. Additionally, microstructural evolution along with the improved mechanical properties of the ECAE processed and ECAE processed plus cold rolled samples are presented to determine the most efficient route in obtaining UFG Ti with favorable mechanical properties as comparable to that of commercial coarse grained Ti64.

4.2. ECAE Processing of Ti

Commercial purity (CP) grade 2 Ti (composition wt%: 0.15 O, 0.006 N, 0.002 H, 0.041 Fe, 0.008 C, Ti balance) initially hot rolled with an average grain size of 110 μm, was used as the starting material. Effect of oxygen concentration on ECAE of Ti was also

demonstrated on CP Grade 4 Ti (composition wt%: 0.3 O, 0.009 N, 0.0028 H, 0.206 Fe, 0.012 C, Ti balance). The main difference between grade 2 and grade 4 Ti is the higher oxygen content in the latter. The average starting grain size was 70 μm for CP Grade 4 Ti. The initial microstructures for CP Grade 2 and Grade 4 are shown in Fig. 4.1.

The as-received Ti bars were extruded in a 90° angle ECAE die which was preheated to 300 °C. Extrusions took place at a rate of 1.27 mm/sec. Between each pass the billets were heated in the furnace for 15 to 30 min at the deformation temperature. Following each extrusion pass, the billets were water quenched to maintain the microstructure achieved during ECAE. Table 4.1 lists the Ti processing details carried out in this study. The minimum deformation temperature which allowed processing without shear localization and macroscopic cracking was determined to be 300 °C for grade 2 Ti and 350 °C for grade 4 Ti. The deformation temperature for grade 2 Ti is lower than previous studies where Ti was deformed via ECAE [176-178]. Low processing temperatures were crucial in preventing possible recrystallization and partly achieved using the sliding walls concept which helps reducing the die frictional effects [185]. Using this method, a number of difficult-to-work materials were processed without macroscopic localization [120, 186, 187].
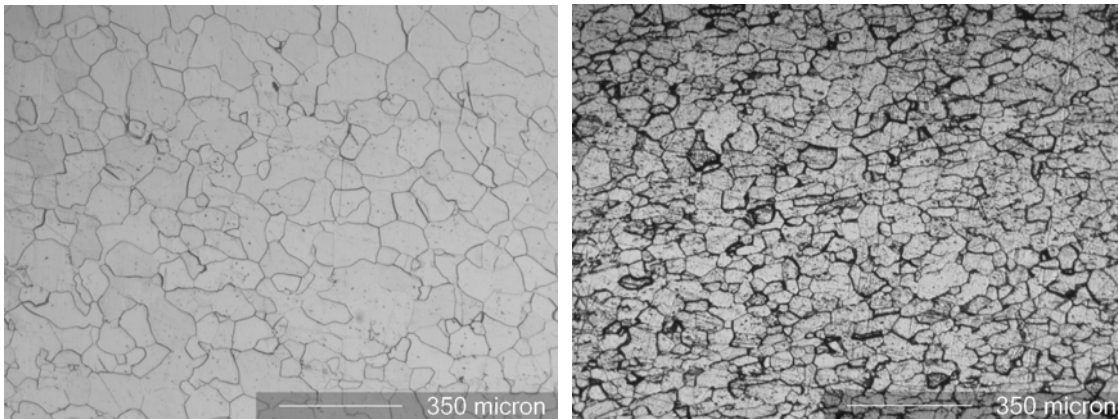
Fig. 4.1. Optical microscopy images showing the as-received microstructures of (a) CP Grade 2 Ti, (b) CP Grade 4 Ti.

Table 4.1

Summary of the commercial purity Ti ECAE processing details.

ECAE of Project Materials								
Material Composition (wt %)	Extrusion Route	Initial Billet Dimensions (in)	Initial Condition	Extrusion Temperature	Heat Treatment	Extrusion Rate (in/sec)	Maximum Recorded Load (kip)	Comments
CP Grade 2 Ti	1A	1x1x6 (approx.)	As received	RT	1hr	0.05	n/a	Failed
CP Grade 2 Ti	1A	1x1x6 (approx.)	As received	200°C	1hr	0.05	241.3	Failed
CP Grade 2 Ti	1A	1x1x6 (approx.)	As received	250°C	1hr	0.05	244.5	Failed
CP Grade 2 Ti	1A	1x1x6 (approx.)	As received	300°C	1hr	0.05	330.2	Failed
CP Grade 2 Ti	1A	1x1x6 (approx.)	As received	300°C	1hr	0.05	300.1	Failed
CP Grade 2 Ti	8B$_C$	1x1x6 (approx.)	As received	350°C	1hr + 30 min	0.05	239.1	Succesful
CP Grade 2 Ti	8E	1x1x6 (approx.)	As received	300°C	1hr + 30 min	0.05	226.8	Succesful
CP Grade 2 Ti	12E	1x1x6 (approx.)	As received	300°C	1hr + 15 min	0.05	289.3	Succesful - Front portion of the billet cracked
CP Grade 4 Ti	4E	1x1x6 (approx.)	As received	350°C	1hr + 30 min	0.05	273.3	Succesful -Stopped Due to High Load
CP Grade 4 Ti	5E	1x1x6 (approx.)	As received	400°C	1hr + 30 min	0.05	264.9	Succesful - Stopped Failure after 5 th pass
CP Grade 4 Ti	8E	1x1x6 (approx.)	As received	450°C	1hr + 30 min	0.05	205.7	Succesful
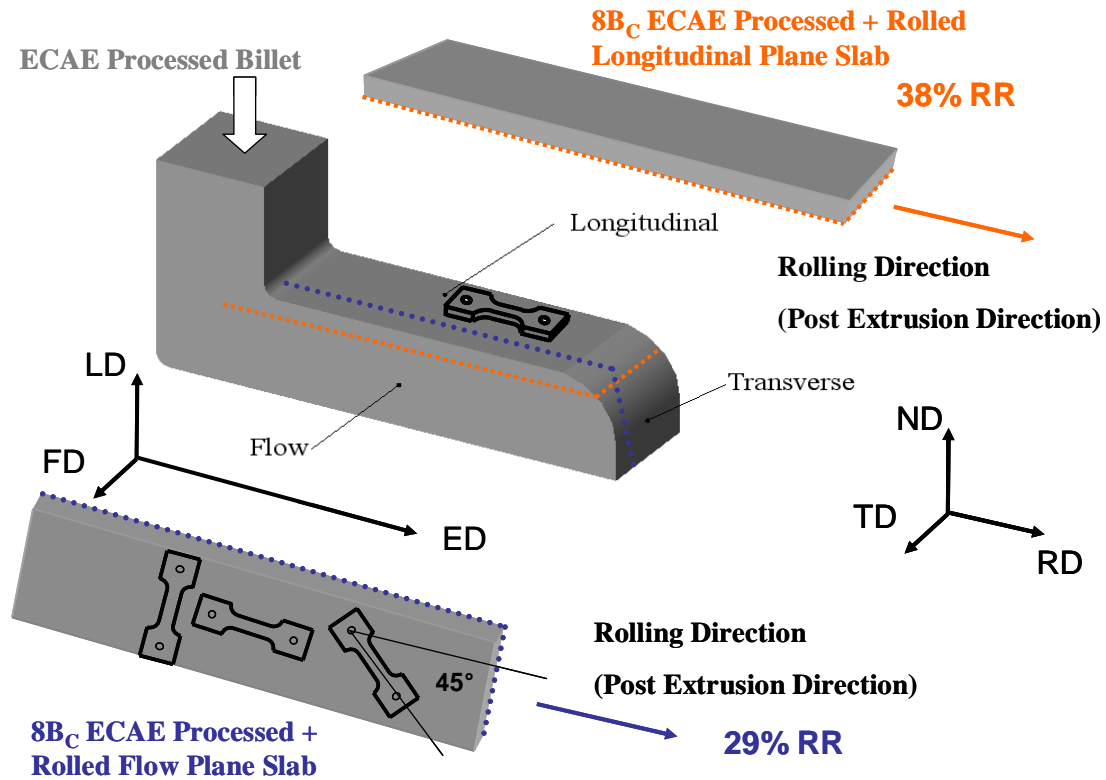
Fig. 4.2. Schematic describing the orientation of the rolled slabs and the tensile specimens used in characterizing the mechanical behavior of the ECAE processed plus rolled Ti. ED, LD and FD denote the extrusion, longitudinal and flow directions, respectively. RD, ND and TD denote the rolling, normal and transverse directions, respectively.

Following the $8B_C$ extrusion of CP grade 2 Ti, slabs for cold rolling were sliced from the sections parallel to the longitudinal and flow planes of the extruded billet (Fig. 4.2.2). The longitudinal plane slab was cold rolled to 38% thickness reduction while the flow plane slab was cold rolled to 29% thickness reduction, both parallel to the previous extrusion direction. The cold rolling process was conducted without intermediate annealing and was terminated as soon as small edge cracks initiated. Room temperature tension tests at a strain rate of 5×10^{-4} s^{-1} were conducted both on the extruded billets (all extrusions) and extruded plus cold rolled slabs (only the $8B_C$ extrusion). The tension samples from the rolled slabs were cut along three orientations to reveal the orientation dependence of mechanical properties, namely parallel, perpendicular and 45° to the

46

rolling direction. The orientations of the rolled slabs and the tension samples are summarized in Fig. 4.2.

4.3. Microstructural Evolution

Fig. 4.3(a) demonstrates the TEM micrographs of the 8B$_C$ ECAE processed billet on the flow plane. It is seen that the microstructure consists of both equiaxed and slightly elongated grains. The elongated grains have their long axes almost parallel to the direction of shear. While the average grain size is 220 nm determined by the linear intercept method, there are some grains with sizes up to 500 nm containing poorly defined internal dislocation arrangements. It is also noted that the microstructure consists of a mixture of grains with low angle and high angle boundaries typical of ECAE processed materials. This is suggested by the selected area diffraction (SAD) pattern having a high number of clustered spots.

ED	500 nm

ED	5 µm

(a)   (b)
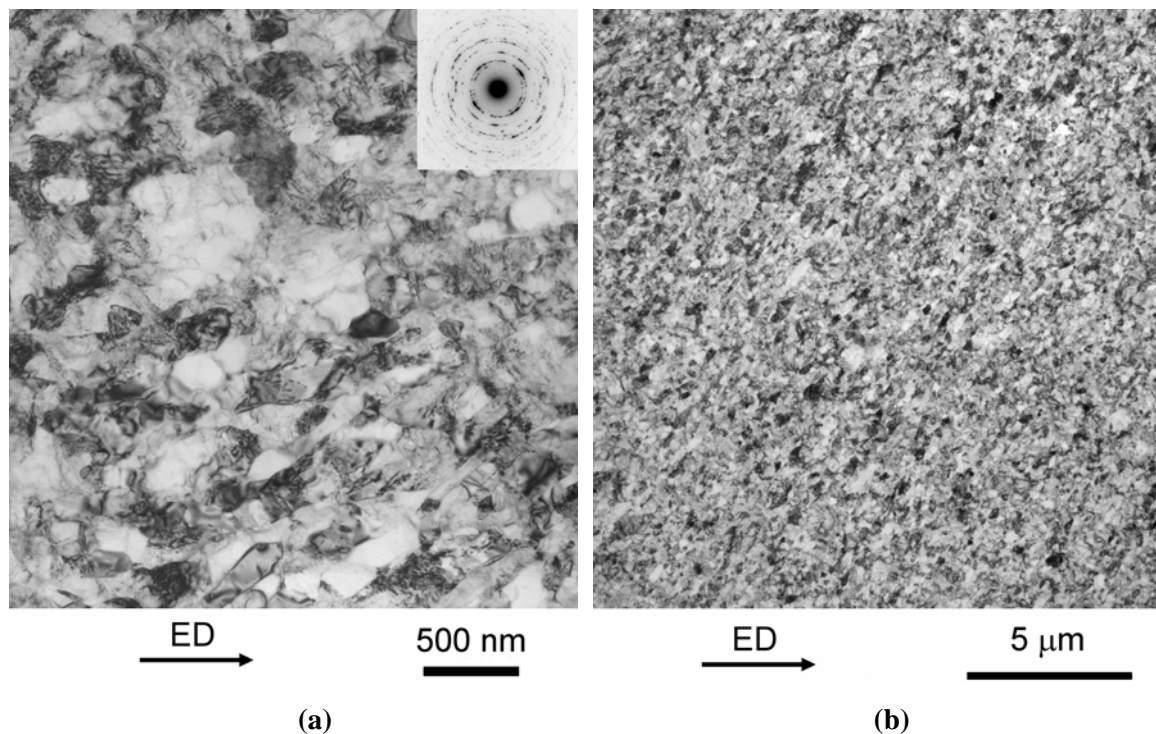
Fig. 4.3. Bright-field TEM image from the flow plane of Ti after eight ECAE passes at 350 ^{o}C, following Route B$_C$. ED represents the extrusion direction.

Fig. 4.3(b) shows a low magnification TEM image from the same cross section where a uniformly refined microstructure is clearly noticeable. Again, the preferential alignment of the grains at an angle to the extrusion direction is apparent. By contrast, the transverse plane displays a higher percentage of equiaxed grains mostly under a size of 250 nm as seen in Fig. 4.4(a). Moreover the grains are aligned in a nearly random manner. This is clearly visible in Fig. 4.4(b).

LD   500 nm   LD   5 μm

(a)   (b)
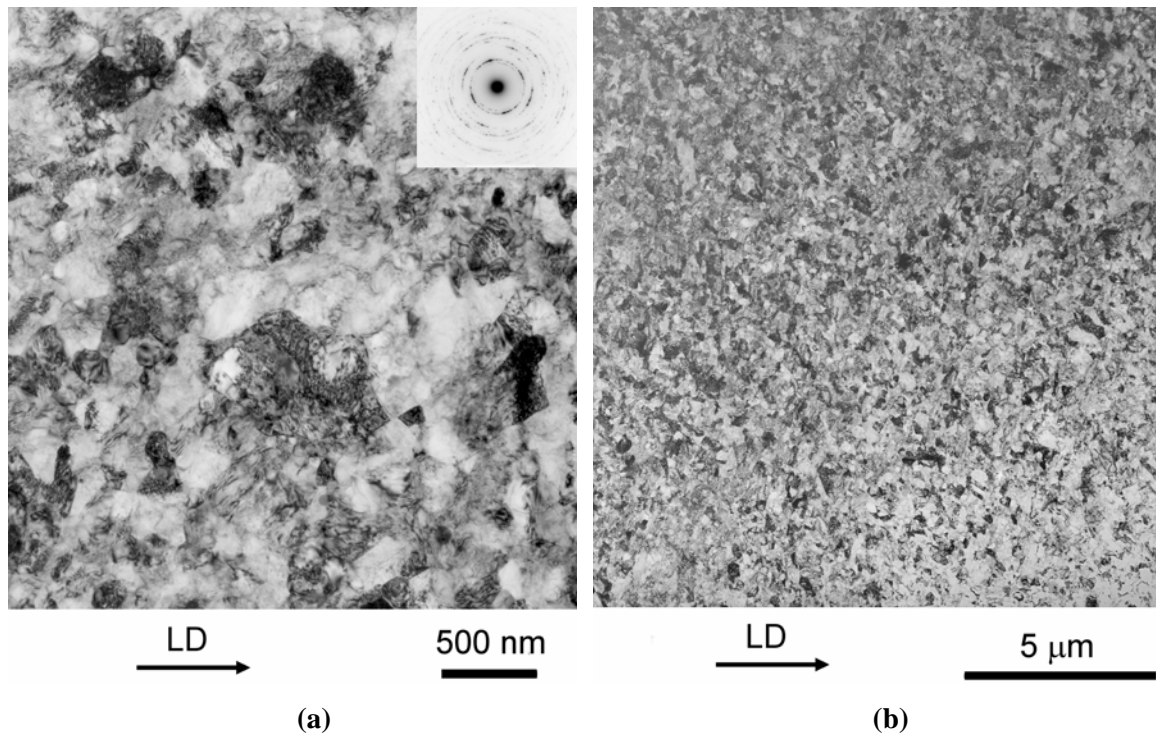
Fig. 4.4. Bright-field TEM image from the transverse plane of Ti after eight ECAE passes at 350 ^{o}C, following Route B_C. ED represents the extrusion direction.

The TEM images taken from the normal plane of the rolled flow plane slab (Figs. 4.5(a) and 4.5(b)) demonstrate the presence of elongated grains having an angle of 20° with the rolling direction as indicated by the dotted line. Although there is no visible refinement in the grain size after rolling, higher dislocation density is prevalent.

RD ← 500 nm

(a)

RD → 5 µm

(b)
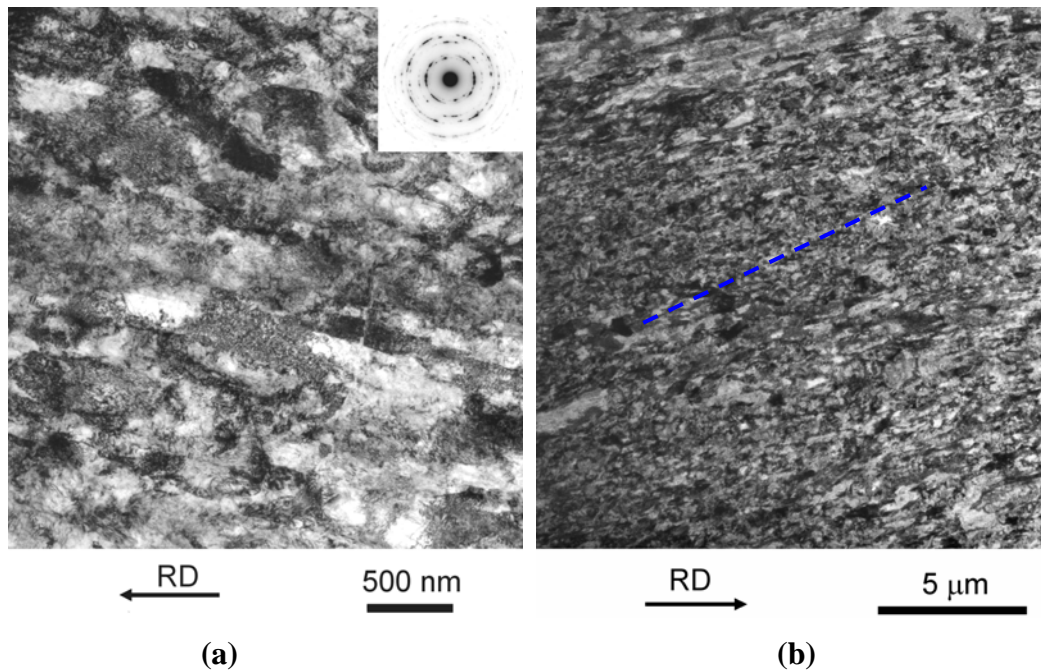
Fig. 4.5. Bright-field TEM image from the normal plane of Ti after 8B$_C$ ECAE at 350 ^{o}C plus rolled on the flow plane to 29% RR. RD shows the rolling direction.

RD ↓ 500 nm

(a)

RD ↓ 5 µm

(b)
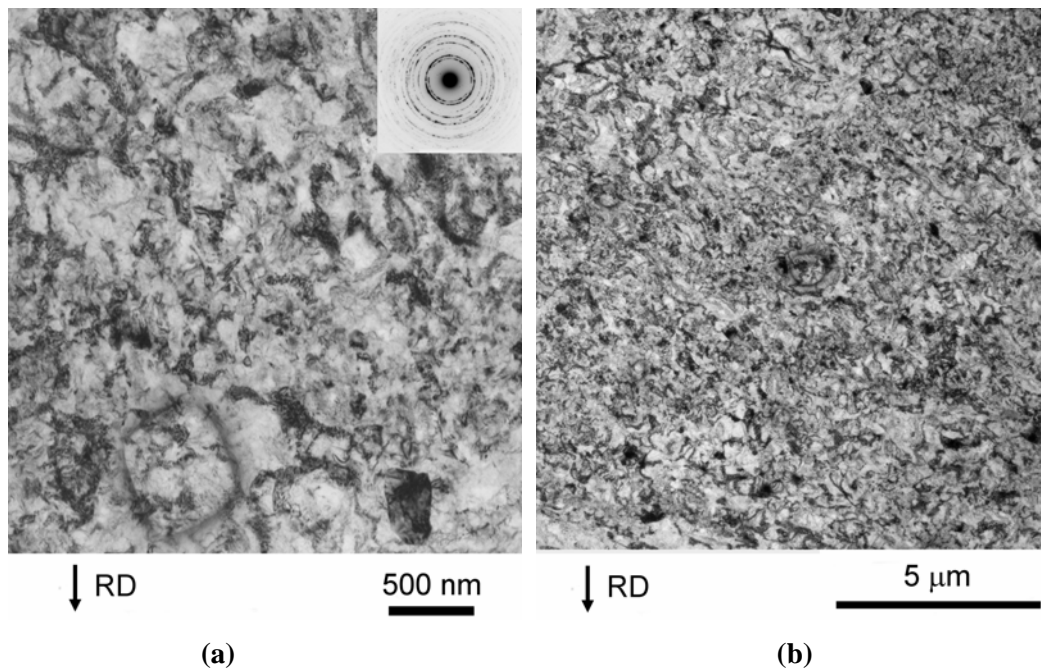
Fig. 4.6. Bright-field TEM image from the normal plane of Ti after 8B$_C$ ECAE at 350 ^{o}C plus rolled on the longitudinal plane to 38% RR. RD shows the rolling direction.

The microstructure of the rolled longitudinal plane slab is exhibited in Figs. 4.6(a) and 4.6(b). Again, the TEM images are taken form the respective normal plane. Grains and subgrains in the nano to submicron range along with areas free of distinct features are present. The SAD pattern contains a typical ring structure indicating boundaries with high angles of misorientation and nearly random local texture.

4.4. Mechanical Behavior after ECAE and Post-ECAE Cold Rolling

Fig. 4.7 shows the stress-strain response of the as-received, $8B_c$ ECAE processed and $8B_c$ ECAE processed plus cold rolled tension specimens. As mentioned earlier the extrusion took place at 350 °C., while rolling was carried out at room temperature. The processed and processed plus cold rolled tension specimens were tested along the extrusion and rolling directions, respectively.
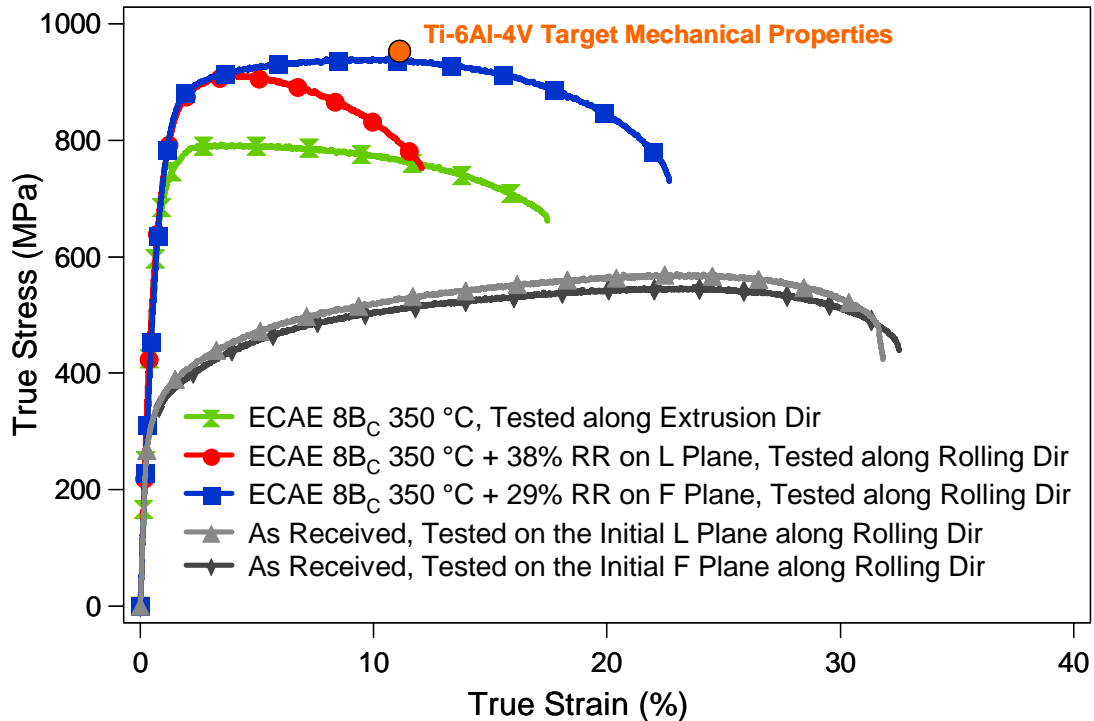
Fig. 4.7. True stress – true strain response of the as received, $8B_C$ ECAE processed and $8B_C$ ECAE processed plus rolled CP Grade 2 Ti at room temperature.

It is seen that ECAE alone doubled the yield strength of as-received grade 2 Ti while maintaining a fracture strain around 17% when tested along the extrusion direction. However, softening starts at an early strain of 4%. Straining of the as-processed plus cold rolled specimens along the rolling direction (previous extrusion direction) resulted in notable increases in the ultimate tensile strength levels. The 29% rolled flow plane slab specimens demonstrated the highest ultimate tensile strength combined with the highest ductility amongst the processed materials. In spite of its higher rolling reduction, the 38% rolled longitudinal plane slab specimens tested along the rolling direction displayed both lower ultimate tensile strength and lower ductility than the 29% rolled flow plane slab due to early plastic instability. The possible reasons for this substantial difference are elaborated in Section 4.5. With these results, ECAE processed grade 2 Ti was elevated to the strength and ductility performance of commercial mill annealed Ti64 alloys [188]. This could open new frontiers in the applicability of pure Ti in more strength demanding environments and replace the widely used expensive alloys.

4.5. Anisotropy in ECAE Processed and Cold Rolled Slabs

The effect of specimen orientation on the stress-strain response is depicted in Figs. 4.8(a) and 4.8(b) for the flow and longitudinal rolled plane slabs, respectively. Rolled flow plane slab specimens demonstrated the highest yield and ultimate tensile strengths when tested parallel to the rolling direction. It is clear that the most promising mechanical properties are obtained during tensile testing of this material perpendicular to the rolling direction due to its highest ductility with reasonable strength values. Although the specimen prepared at 45° to the rolling direction has the same ductility with that of the parallel specimen, it has a considerably lower strength value. In contrast to the flow plane slab, the 38% rolled longitudinal plane slab exhibited the highest tensile strength when tested at 45° to the rolling direction due to its comparably deferred necking, as seen in Fig. 4.8(b). The highest yield strength is observed during straining of the specimen perpendicular to the rolling direction. Underlying mechanisms for anisotropy will be discussed in detail in Section 4.10.
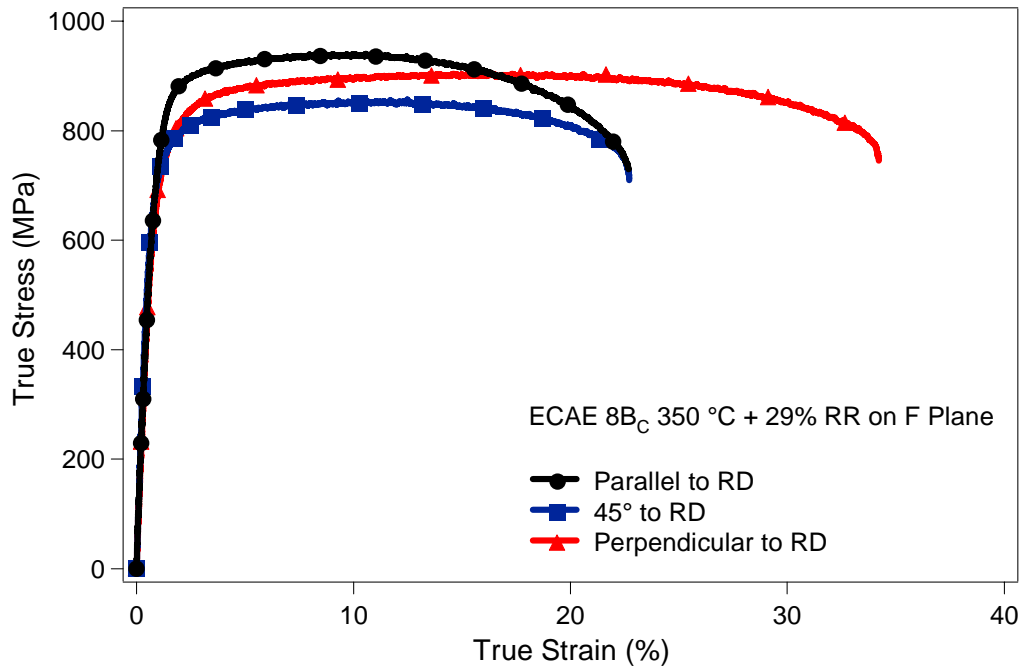
(a)
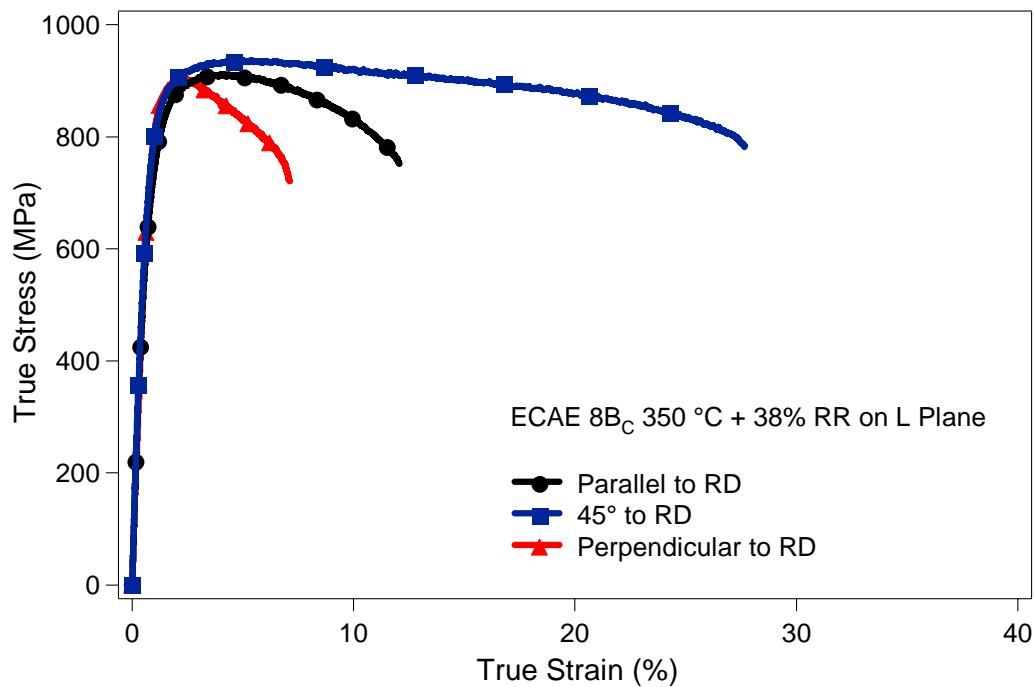
(b)

Fig. 4.8. Effect of tensile specimen orientation on the mechanical properties of the $8B_C$ ECAE processed plus (a) rolled flow plane slab, (b) rolled longitudinal plane slab at room temperature.

Table 4.2

Summary of the results of the mechanical experiments conducted at room temperature on the as-received, $8B_C$ ECAE processed and $8B_C$ ECAE processed plus cold rolled CP Grade 2 Ti.

Processing Condition		Average Grain Size (nm)	Yield Strength (MPa)	Ultimate Tensile Strength (MPa)	Fracture Strain (%)
As-received, Initial Flow Plane, Parallel to ED		-	307 ± 11	532 ± 18	33 ± 1
As-received, Initial Longitudinal Plane, Parallel to ED		-	313 ± 14	571 ± 21	32 ± 3
ECAE $8B_c$ at 350 °C, Parallel to ED		220 ± 40	665 ± 16	793 ± 15	18 ± 2
ECAE $8B_c$ at 350 °C + Rolling on the Flow plane to 29% reduction	Parallel to RD	120 ± 20 (Minor axis) 415 ± 40 (Major axis)	754 ± 19	940 ± 23	23 ± 3
	45° to RD		653 ± 20	857 ± 26	23 ± 2
	Perpendicular to RD		624 ± 11	904 ± 19	34 ± 3
ECAE $8B_c$ at 350 °C + Rolling on the Longitudinal plane to 38% reduction	Parallel to RD	140 ± 30	625 ± 17	912 ± 27	12 ± 2
	45° to RD		668 ± 15	937 ± 24	27.7 ± 2.5
	Perpendicular to RD		725 ±10	905 ± 16	7.6 ± 1.4

The mechanical test results of the ECAE processed and ECAE processed plus rolled specimens are summarized in Table 4.2. All the tension specimens from the rolled longitudinal plane slab soften at an earlier stage of plastic deformation as compared to the ones from the rolled flow plane slab. This can be attributed to its more equiaxed structure leaving limited room for strain hardening mechanisms to operate upon further straining [189]. It can also be explained by the possibly higher population of high angle boundaries and stronger texture observed on the rolled flow plane slab as suggested by Hoppel et al. for UFG aluminum [190]. Rolling on the flow plane is an important strain path change after ECAE, while rolling on the longitudinal plane is a less severe path change. Thus, it is expected that the newly activated systems during rolling on the flow plane would cut through the dislocation substructure previously formed during ECAE. This might result in an effective microstructural refinement of the rolled flow plane slab, leading to increased hardening during subsequent post-rolling tension experiments.
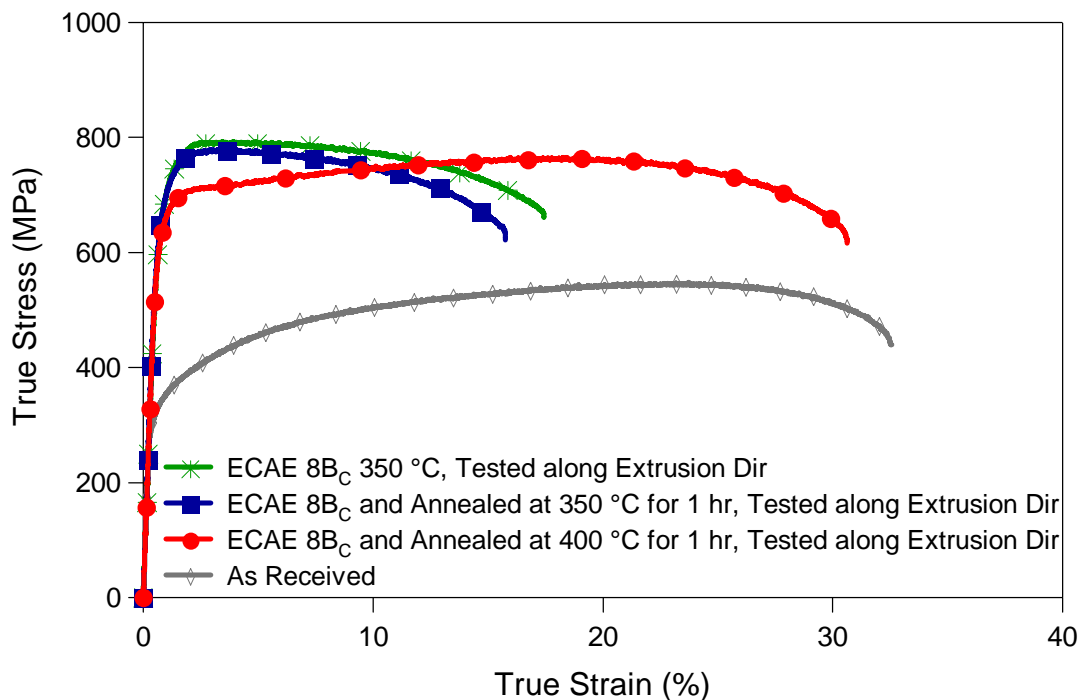
Fig. 4.9. True stress – true strain tensile response of the $8B_C$ ECAE processed and $8B_C$ ECAE processed plus annealed CP Grade 2 Ti at room temperature.

4.6. Effect of Post-ECAE Annealing

Annealing of the tension specimens were also carried out to further improve the mechanical response with the goal of higher ductility without sacrificing strength. Annealing of the $8B_C$ ECAE processed samples showed that one hour treatment at 400 °C was effective in creating a microstructure that balances high tensile strength and high ductility as seen in Fig. 4.9. The ductility of this sample (~ 31%) almost reaches to that of the as-received material. In contrast, the 350 °C heat treatment did not improve the ductility. The heat treatment condition providing optimized mechanical properties depends on the amount of recovery of the microstructure in study. Apparently, the recovery kinetics of the 350 °C and 400 °C heat treatments are different. Similarly in Fig. 4.10, one hour annealing treatments at 350 °C and 400 °C improved the tensile ductility levels for $8B_C$ ECAE processed plus cold rolled tension specimens on the flow and longitudinal planes, respectively. Annealing treatment results are summarized in Table 4.3 and will be elaborated in more detail in Section 4.10.
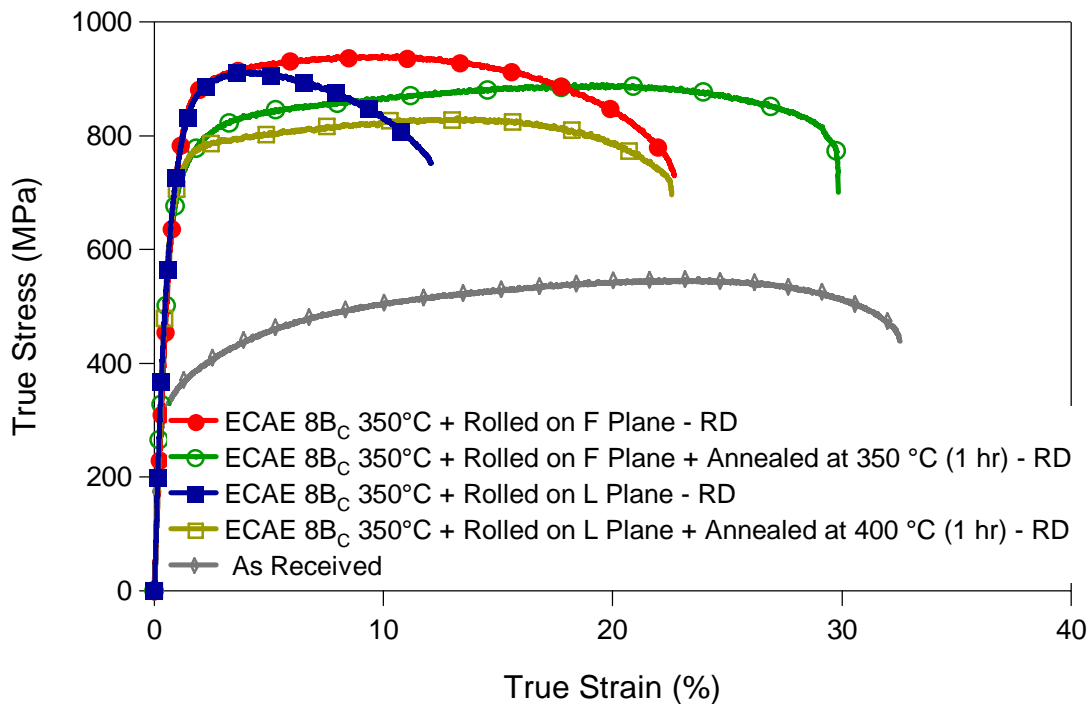
Fig. 4.10. True stress – true strain tensile response of the $8B_C$ ECAE processed and $8B_C$ ECAE processed and cold rolled plus annealed CP Grade 2 Ti at room temperature.

Table 4.3

Summary of the results of the mechanical experiments conducted at room temperature on the ECAE processed and ECAE processed plus annealed CP Grade 2 Ti and CP Grade 4 Ti following various routes.

Material	Processing	Yield Strength (0.2% offset) (MPa)	UTS (MPa)	Fracture Strain (%)
CP Ti, Grade 2	As-received	307 ± 11	532 ± 18	33 ± 1
	ECAE 8B$_C$ at 350 °C	665 ± 16	793 ± 15	18 ± 2
	ECAE 8B$_C$ at 350 °C + Annealed at 350 °C for 1 hr	651 ± 9	779 ± 13	15.8 ± 2.5
	ECAE 8B$_C$ at 350 °C + Annealed at 400 °C for 1 hr	626 ± 14	765 ± 12	30.6 ± 2.8
	ECAE 8B$_C$ + Rolled 29% RR on F Plane - Parallel to RD	754 ± 19	940 ± 23	23 ± 3
	ECAE 8B$_C$ + Rolled 29% RR on F Plane + Annealed at 350 °C for 1h - Parallel to RD	617 ± 12	890 ± 17	29.8 ± 3.2
	ECAE 8B$_C$ + Rolled 38% RR on L Plane - Parallel to RD	625 ± 17	912 ± 27	12 ± 2
	ECAE 8E at 300 °C	620 ± 3	760 ± 8	20.7 ± 4.2
	ECAE 8E at 300 °C + Annealed at 400 °C for 1 hr	627 ± 12	722 ± 10	17.9 ± 2.8
	ECAE 12E at 300 °C	564 ± 21	771 ± 17	22.8 ± 1.1
CP Ti, Grade 4	As-received	531 ± 6	792 ± 9	24.8 ± 2.1
	ECAE 8E at 450 °C	758 ± 8	947 ± 13	25 ± 3
	ECAE 8E at 450 °C + Annealed at 350 °C for 1 hr	783 ± 14	947 ± 11	21± 2
	ECAE 8E at 450 °C + Annealed at 400 °C for 1 hr	695 ± 15	927 ± 18	28.7 ± 2.3

4.7. Effect of ECAE Processing Route

In quest for achieving the best mechanical response, alternative ECAE routes were applied to Ti. Specifically, route E which gives a high yield of fully processed

material with equiaxed microstructure is followed. It was possible to process Ti at temperatures as low as 300 °C following route 12E. Fig. 4.11 demonstrates the tensile response of 8 and 12 passes ECAE processed grade 2 pure Ti.

It is seen that route E slightly decreased the strength levels; however, the apparent increase in ductility levels and strain hardening rates are noticeable. Moreover, route E increases the extent of uniform deformation. The lowering of strength levels is surprising considering the lower extrusion temperature. When increasing the number of passes from 8 to 12, tensile ductility is somewhat improved without any change in the strength levels. A positive attribute is that the strain hardening rate increased after 12 passes. Thus, among the routes investigated 12 passes following route E at 300 °C yields the desired combination of strength and ductility. The flow response of the annealed 8E billet was not satisfactory due to its lower ductility than the as-processed billet. Results are summarized in Table 4.3.
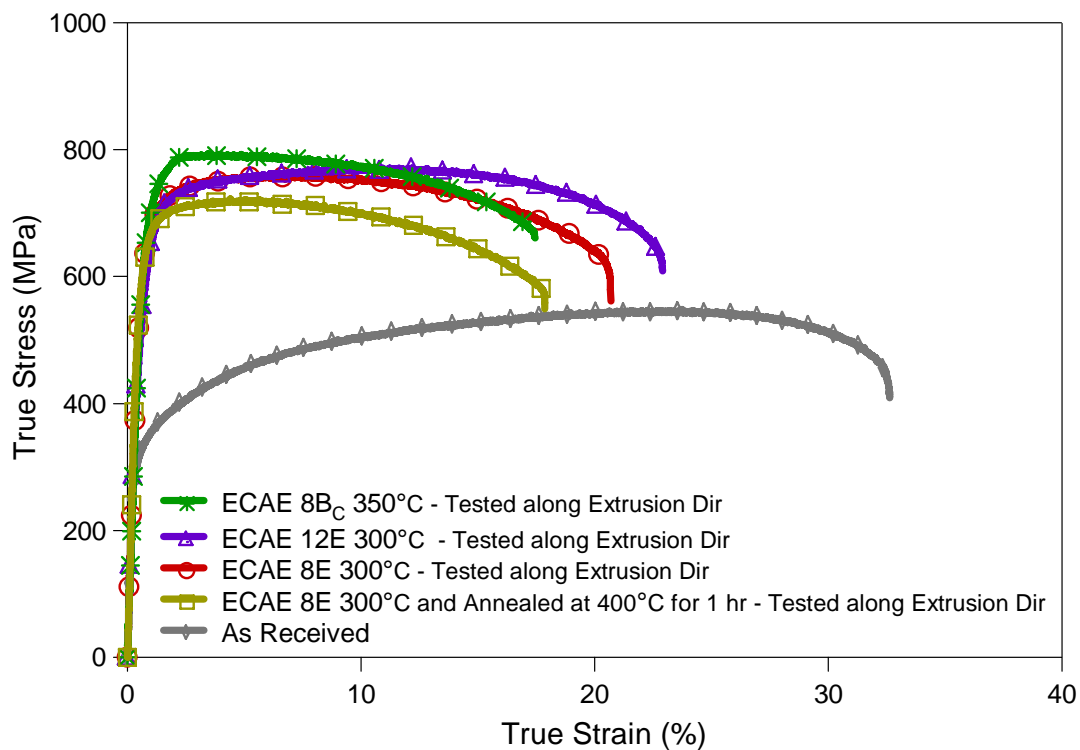
Fig. 4.11. True stress – true strain response of the as received and ECAE processed CP Grade 2 Ti following various routes at room temperature.

4.8. Effect of Impurity Content

Commercial purity grade 4 Ti extrusions have been performed to investigate the effect of impurity content on the mechanical response of UFG Ti. These extrusions were more challenging due to the higher oxygen content of this material resulting in lower ductility of the material. Relatively low ductility and the high strain hardening rate of the as-received grade 4 Ti is shown in Fig 4.12. Thus, extrusions were held at higher temperatures than those used for grade 2 Ti. Route E was followed to yield more fully worked material with highly refined microstructure.
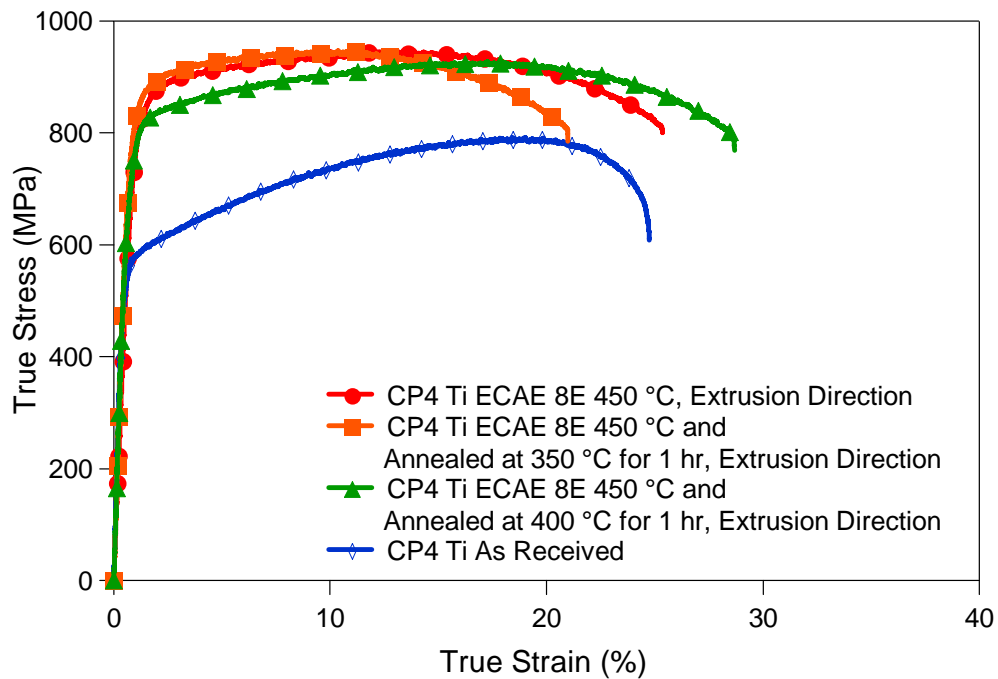
Fig. 4.12. True stress – true strain response of the as received, ECAE processed and ECAE processed plus annealed CP Grade 4 Ti at room temperature.

The stress-strain response of the 8E 450 °C extruded and extruded plus annealed specimens is illustrated in Fig. 4.12. It is seen that ECAE of this material considerably improved the yield strength without any loss in ductility. Although the hardening rate decreased considerably after ECAE, the uniform elongation is still in excess of 10%. Post

processing annealing treatment at 350 °C for one hour did not show any effect on the stress-strain response. Annealing at 400 °C for the same amount of time increased the hardening rate leading to higher uniform elongation at the ultimate tensile strength with a small decrease in the strength values. Heat treatments at higher temperatures (450 °C to 500 °C) are possible methods to obtain even higher failure strain values. The mechanical test results of UFG grade 4 Ti are summarized in Table 4.3.

4.9. Crystallographic Texture Evolution during ECAE and Cold Rolling

Texture development of Ti after $8B_c$ ECAE and ECAE plus rolling is shown in Fig. 4.13 along with the initial texture via inverse pole figures. The direction markings on the as-received inverse pole figures of Fig. 4.13(a) indicate the orientation of the initial billet with respect to the ECAE processed billet. Also the rolled inverse pole figures were arranged to have the same sequence of sample directions with respect to that of the ECAE billet. Namely the RD, TD and ND of the rolled flow plane slab correspond to the ED, LD and FD of the previously extruded billet. Similarly, the RD, ND and TD of the rolled longitudinal plane slab correspond to the ED, LD and FD of the previously extruded billet.

It is seen that the as received material has a weak texture with a high percentage of its $(11\bar{2}0)$ poles aligned along the extrusion direction. After ECAE, the texture gets stronger with the $(20\bar{2}3)$ poles along the longitudinal direction. The main texture strengthening is achieved during rolling, especially for the flow plane slab with less spread texture. The flow plane slab has its $(20\bar{2}1)$ poles mainly aligned with the rolling direction. For the longitudinal plane slab, the texture is weaker and the ND direction is aligned with the $(10\bar{1}2)$ and $(11\bar{2}4)$ poles.

Comparing the texture evolution of the ECAE processed sample with the ECAE plus rolled samples draws interesting conclusions. It is seen that although the ECAE processed sample has strong texture components along LD, and very weak texture along ED; rolling on the flow plane formed components along the rolling direction (previous ED) while there are no strong components left in the transverse direction (previous LD).

In contrast, rolling on the longitudinal planes almost preserves the texture formed during the extrusion process. This anomaly can be ascribed to the abrupt change in loading path imposed during rolling on the flow plane as opposed to a comparably monotonic strain path when rolled on the longitudinal plane [45, 46, 191]. This might also explain the early softening in the rolled longitudinal plane slab as mentioned earlier in Section 4.5.
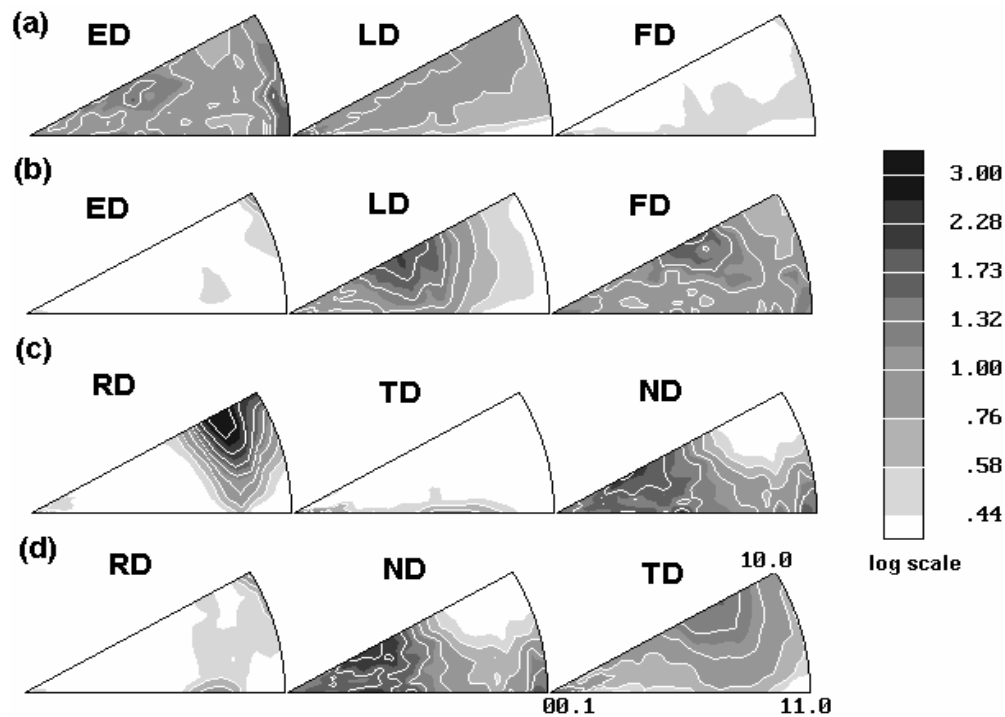
Fig. 4.13. Inverse pole figures showing the texture evolution of the (a) as-received, (b) 8B$_c$ ECAE processed, (c) 8B$_c$ ECAE processed plus rolled on the flow plane, (d) 8B$_c$ ECAE processed plus rolled on the longitudinal plane specimens. ED: Extrusion Direction, LD: Longitudinal Direction, FD: Flow Direction, RD: Rolling Direction, TD: Transverse Direction, ND: Normal Direction.

4.10. Discussion of the Results

In an attempt to investigate whether crystallographic texture is the sole reason causing in-plane anisotropy in the 8B$_c$ ECAE processed and 8B$_c$ ECAE processed plus rolled samples, average yield strength values of the rolled samples in three straining

directions were measured. Average flow strengths obtained along 0°, 45° and 90° experiments were divided by the corresponding Taylor factors (M) and plotted against the change in the angle to rolling direction as shown in Fig. 4.14. Taylor factors were calculated from the measured textures utilizing a VPSC crystal plasticity model. Details regarding the VPSC model have been explained in Section 2.7.1
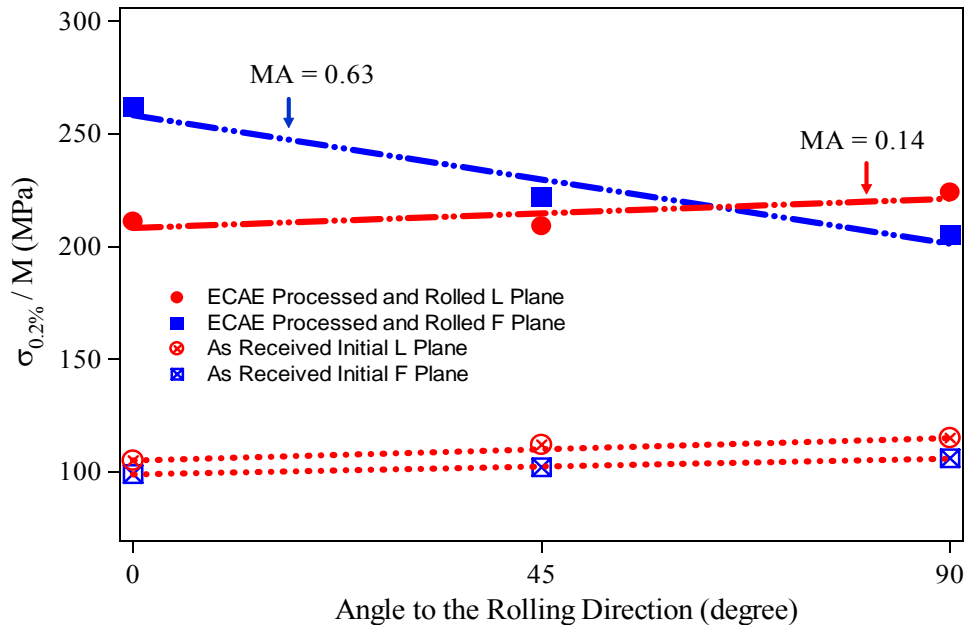
Fig. 4.14. Variation of the crystallographic texture corrected yield strengths with angle to the rolling direction. M represents the Taylor factor, MA represents the magnitude of anisotropy and is explained in detail in the text.

In predicting the Taylor factors, a combination of slip and twinning systems commonly observed in Ti during room temperature straining were assumed to be operative. For accurate predictions, the selection of critical resolved shear stress (CRSS) levels is important. Earlier studies on titanium single crystals concluded that prismatic slip is the preferential deformation mode [192, 193]. Interstitial alloying elements such as oxygen and nitrogen have a profound effect on the CRSS levels of the active deformation systems. It is known that oxygen strongly suppresses twinning, additionally pyramidal slip along <c+a> is harder in the presence of interstitial atoms due to the extended core

structure of these dislocations. Moreover, the difference between the CRSS levels of prismatic and basal slip along <a> gets smaller with increase in alloying concentrations. TEM studies on a cold-rolled α Ti alloy showed that prismatic slip is the easiest system to activate and pyramidal slip along <c+a> is the hardest [194]. Philippe et al. [194] used a Taylor type model to predict the cold rolling texture of Ti with an initial grain size of 35 μm having a similar chemical composition with the Ti used in the present investigation. Their results were in good agreement with the experimental observations up to 80% rolling reduction.

In the present study, Taylor factors of the as-received Ti are simulated using the following relative CRSS values:

$$\tau_{\{prism\}} = 1; \ \tau_{\{basal\}} = 5; \ \tau_{\{pyr<c+a>\}} = 12; \ \tau_{\{(10\bar{1}2) \ Twin\}} = 9; \ \tau_{\{(11\bar{2}2) \ Twin\}} = 10$$

These values are the same as the ones used in [194]. Gray [195] reported a greater propensity for twinning in large grain sized Ti. Therefore, one would expect to observe a less pronounced twinning activity during straining of a fine grained Ti which was previously ECAE processed and rolled. For simulating the Taylor factors of the ECAE processed and rolled Ti, CRSS levels for twinning are slightly increased while keeping CRSS levels for slip the same as used in simulating the as-received Ti.

After eliminating the texture effects with the simulated Taylor factors, the in-plane variation of yield strengths are demonstrated in Fig. 4.14. Since the effects of texture are eliminated, the remaining anisotropy might be attributed to the directionality of the microstructure evolved during the two step ECAE plus cold rolling deformation. For the rolled slabs, the contribution of processing induced microstructure to the yield strength anisotropy is quantified by the slopes of the linear fit lines. The slope of a linear fit line is named as the magnitude of anisotropy (MA) factor. As expected, the as-received material shows no sign of microstructure based anisotropy. The rolled longitudinal plane slab appears to be almost isotropic, while the rolled flow plane slab has a noticeable trend in yield strengths when rotating from 0° to 90° orientation indicated by the high magnitude of its MA factor.

Higher anisotropy in yield strengths of the rolled flow plane slab can be explained by the microstructural evolution during processing. As already demonstrated in Figs. 4.5 and 4.6 that as opposed to the rolled longitudinal plane slab where there is little tendency

to form a directional deformation substructure, the flow plane slab contains a lamellar structure having a macroscopic orientation. The apparent discrepancy in microstructural evolution can be explained by the fact that the formation of certain dislocation boundaries and their macroscopic alignment and orientation with respect to slip planes are correlated with crystallographic texture evolution both in coarse grained materials and their UFG counterparts [28]. The orientation dependence of microstructure evolution was observed in coarse grained and UFG copper. According to the orientation of the tensile axis, the microstructure evolved to either one set of extended planar dislocation boundaries parallel to {111} slip plane, two sets of intersecting less straight or even wavy extended dislocation boundaries, or an equiaxed cell structure during uniaxial straining [28].

The microstructure of the rolled flow plane slab contains elongated subgrains with low to high angle boundaries delineated by lamellar dislocation substructures as seen in Fig. 4.5. This oriented structure is believed to be the underlying factor causing higher anisotropy with the following mechanism. Orientation of the dislocation boundaries with respect to the straining direction affects the boundary spacing on the active slip plane. Since boundaries act as obstacles for slip, variations in the boundary spacing influence the mean free path of dislocations during subsequent deformations. The mean free path of dislocations determines the contribution of dislocation boundaries to flow anisotropy [30, 196, 197]. Considering this length-scale effect through a Hall-Petch type formulation, the magnitude of yield strength anisotropy can be dictated by adjusting the critical shear stress of the slip systems [30, 35]. Yield strength anisotropy was also predicted via crystal plasticity models incorporating the effect of dislocation substructure to hardening laws through internal variables [29, 45, 198]. It is worth mentioning that texture affects not only the onset of plastic flow but also the evolution of strength upon deformation. Thus, crystallographic texture and directional deformation substructure should also be responsible for the different strain hardening behaviors and ductility values exhibited with the change in loading direction during tensile testing of the $8B_c$ ECAE processed plus rolled slabs.

A two-fold increase in yield strengths of the CP grade 2 Ti is obtained after 8 passes following route B_c. Other extrusion routes were also conducted and the positive attribute of route E in increasing ductility was exhibited. Thus, extrusions on CP grade 4

Ti were only carried out following route E. Higher impurity content, mainly oxygen, in grade 4 Ti increases the CRSS levels of all slip systems. Though, the relative increase in CRSS for prism slip is much higher than that for basal slip. This might cause a shift in the primary slip system from prismatic slip to basal slip in grade 4 Ti. Moreover, Williams et al. [199] found a transition from a uniform distribution of dislocations to planar type slip with increasing oxygen concentration in titanium. Propensity for twinning is also strongly linked with impurity content and is reduced by increasing impurity content. Strain localization associated with planar slip and reduced twin formation are the main reasons for low formability. In summary, one expects to observe a different microstructural evolution during ECAE of grade 4 Ti as compared to that for grade 2 Ti. This can be one of the reasons for the apparently higher strain hardening rate of UFG grade 4 Ti.

It was demonstrated that annealing treatments on the specimens processed by ECAE and ECAE plus cold rolling are effective for obtaining better ductility levels with a small decrease in strength levels. The main idea of annealing treatments is to remove the excess dislocation density while preserving the UFG structure obtained via ECAE. Thus, the optimum annealing temperature that will only decrease the excess dislocation density without abnormal grain growth should be found. The microstructure after annealing should restore the dislocation storage ability of the material, increase strain hardening rate and eventually improving its ductility. Thus, it depends on the dislocation density of the as-processed microstructure. For instance, one hour heat treatment at 350 °C was sufficient to improve the ductility of the $8B_c$ rolled flow plane slab, whereas temperature was elevated to 400 °C to obtain a comparable effect in the $8B_c$ rolled longitudinal plane slab. A similar explanation is due at this point for choosing 400 °C over 350 °C as the annealing temperature to increase ductility in UFG grade 4 Ti obtained via 8E ECAE. The 400 °C one hour annealed sample exhibited a fracture strain higher than that of the as-received material.

4.11. Conclusions

This chapter focused on the evolution of microstructure and resulting mechanical behavior of ECAE processed CP Ti with different impurity contents and via various processing routes. Grade 2 Ti billets are subjected post-ECAE cold rolling for achieving

higher strengths. After processing annealing treatments were conducted to improve ductility levels. Possible mechanisms responsible for the plastic flow anisotropy encountered during tensile testing of the $8B_c$ rolled slabs along different directions were identified. The following conclusions can be drawn:

1. ECAE of CP Ti resulted in grain refinement down to submicron regime leading increased strength levels. Grade 2 Ti was uniformly deformed at temperatures as low as 300 °C following route 8E, whereas grade 4 Ti was deformed at 450 °C with the same route. UFG grade 2 Ti exhibited a more than two times increase in yield strength over the as-received material. UFG grade 2 Ti following 8 passes of route E showed improved ductility with a slight decrease in strength over route B_c with the same number of passes.

2. Annealing treatments on the UFG grade 2 and grade 4 Ti are beneficial for restoring the strain hardening ability of these materials. For specific annealing temperatures and durations, UFG grade 2 Ti exhibited two times higher yield strength and similar ductility with the as-received material, while UFG grade 4 Ti exhibited 1.5 times higher yield strength and higher ductility than the as-received material.

3. Post-ECAE rolling of the $8B_c$ processed CP grade 2 Ti on the longitudinal plane resulted in an equiaxed and refined microstructure. The mechanical behavior showed slight in-plane flow stress anisotropy, while significant variations occurred in the fracture strains.

4. The most promising mechanical properties bringing together a high ductility (23%) combined with high strength levels (YS ~ 754 MPa and UTS ~ 940 MPa) were obtained through straining of the rolled flow plane slab perpendicular to the rolling direction. This material exhibited mechanical properties comparable to those of commercial Ti64. With its directional substructure, the in-plane anisotropy of the yield strengths in the rolled flow plane slab was much more pronounced than that observed in the rolled longitudinal plane slab.

5. Crystallographic texture becomes stronger during the post-ECAE deformation (cold rolling). The discrepancy in the texture evolution between the rolled flow

and longitudinal planes is believed to be associated with the more abrupt change in strain path during rolling on the flow plane.

6. The noticeable yield strength anisotropy of the rolled flow plane slab cannot be explained by the sole effect of crystallographic texture. Instead, it is attributed to the existence of a microstructure consisting of oriented subgrain/grain boundaries. In contrast, lack of microstructure based yield strength anisotropy in the rolled longitudinal plane slab is coincident with its equiaxed microstructure having no preferred alignment of the subgrain/grain boundaries making mean free path of dislocations uniform.

4.12. Suggestions for Future Work

Although pure Ti has been ECAE processed to improve its mechanical properties, a detailed study on the post-processing annealing treatments to further enhance the ductility levels without a significant loss in strength levels deserves attention. Such a study should also include the respective microstructural changes with applied heat treatments. A controlled heat treatment study may lead to the formation of a bimodal microstructure combining both high strength and high ductility.

One interesting phenomena was the lower strength levels obtained via the lower temperature extrusions following route E. Normally, one expects to observe higher strength levels during lower temperature processing due to limited recovery mechanisms. The reason for this anomaly can be attributed to the different textures evolved during route E processing and needs further exploration.

As explained thoroughly, further cold rolling on the $8B_c$ processed billet was carried out to take advantage of a strain path change, further refine grain size and improve the resulting mechanical behavior. Following the same methodology on the 8E processed billets receives merit, because since they have a higher ductility they can endure higher thickness reductions. Eventually, this might provide a high strength high ductility end material. Cold rolling can also be applied to the ECAE processed UFG grade 4 Ti for further grain refinement. However, this might present processing challenges due to the limited formability of this material.

CHAPTER V

EFFECT OF STRAIN PATH CHANGES ON THE MICROSTRUCTURE, TEXTURE AND FLOW BEHAVIOR OF UFG TI-6AL-4V ALLOY

5.1. Background

Ti-6Al-4V (referred as Ti64) is a two phase (α+β) alloy widely used in aerospace and biomedical applications due to their low density, high strength, toughness, good elevated temperature properties and formability. They combine the strength of alpha (α) alloys with the ductility of beta (β) alloys, and their microstructure and properties can be varied widely by appropriate heat treatments and thermo-mechanical processing. For Ti64, at temperatures above 985 ºC, the alpha phase transforms into a bcc crystalline structure, called the beta phase. Alloying elements can stabilize the β phase so that both α and β can exist at room temperature. In Ti-6Al-4V, aluminum serves as the α stabilizer and the vanadium stabilizes the β phase [188, 200].

For fully lamellar microstructure which is formed by slow cooling from above the the β transus temperature; α colony size, the width of the lamellae, and the character of the interlamellar interface are important factors affecting the mechanical behavior of this alloy [200, 201]. These microstructural features have also shown to be effective in determining the fatigue behavior of Ti64. According to Lutjering [200], the bimodal microstructure, globular primary α and transformed β decorated with lamellar α and β, should exhibit a higher yield stress, a higher ductility, an improved high cycle fatigue strength and a slower crack propagation rate of microcracks as compared with a fully lamellar microstructure. Nevertheless, due to low volume fraction of the beta phase (β) (<10%) in the present material, the deformation behavior is dominated by the alpha (α) phase which has an hcp structure with limited number of slip systems [200, 202]. Although slip in bcc β has an effect on the deformation of Ti64, majority of the plastic strain is accommodated by the hcp α phase and texture evolution is not noticeably affected by slip in β [202].

Deformation processing and resulting texture evolution of hcp materials have been a topic for a number of studies. However only few focused on Ti64, and other than

the study by DeLo et al. [203], there has been no work on the texture evolution of ECAE processed Ti64. Although pure Ti has been severely deformed using ECAE as noted in the previous chapter, the attempts on refining the microstructure of Ti64 using SPD techniques have been limited [22, 186, 204-206]. The main obstacle behind exploration of SPD characteristics of this material is its limited ductility, shear localization and need of very high loads for processing. Few of the works on the ECAE of Ti64 focused on the formability behavior at different temperatures [22, 206]. Semiatin et al. [22] reported shear localization and surface cracking of colony α Ti64 during non-isothermal ECAE at temperatures as high as 900°C. Another attempt [206] achieved successful ECAE processing of Ti64 with different initial microstructures at 600 °C focusing on microstructural refinement and its relation to processing parameters. Other than ECAE, Ti64 has also been investigated after deformation with other SPD techniques. Sergueeva et al. [204] and Mishra et al. [204] demonstrated substantial refinement of the primary α phase in a commercial Ti64 using high pressure torsion (HPT) leading to enhanced superplasticity.

A number of studies concentrated on the texture evolution of the hcp materials such as pure Ti and Zr and Mg alloys during ECAE which are easier to process than Ti64 [181, 184, 207]. The only texture evolution study on the ECAE processed Ti64 is the work by DeLo et al. [203]. They investigated the texture evolution near or above α/β transus temperature. Except few of the aforementioned works [186], there is no detailed work on the deformation systems activated during SPD including twinning, their effect on texture evolution and resulting room temperature mechanical properties. The present study aims at addressing some of these issues.

As shown in the previous chapter, ECAE processing of CP Ti led to substantial improvements in the mechanical behavior. In this chapter, the effects of second phase on ECAE processing, resulting microstructure and texture evolution are demonstrated. Indeed, the present author achieved uniform ECAE processing of Ti64 at temperatures as low as 550 °C where significant improvement in mechanical properties were indicated [203]. The effects of extrusion temperature (from 550 °C up to 800 °C) on ECAE microstructure and room temperature mechanical behavior of the extrudates were studied. Unexpected stress-strain response of UFG Ti64 after two ECAE passes at 800 °C, as

compared to that of lower temperature extrusions gave way a thorough examination of the microstructure and texture evolution in the samples processed at this temperature.

5.2. ECAE Processing of Ti-6Al-4V

The Ti-6Al-4V (Ti64) alloy (composition wt%: 6 Al, 4 V, 0.4 Fe, 0.1 C 0.05 N, 0.02 O, 0.015 H, Ti balance) was received in the form of cylindrical rods with a diameter of 10 mm, fabricated by blending powder, cold isostatically pressing at 380 kPa and vacuum sintering at 1230 °C for 4 hrs. This was followed by hot isostatically pressing at 100 kPa and 900 °C for 2 hrs followed by furnace cooling. This procedure resulted in a coarse colony lamella α microstructure with an average colony size of 70 μm and the α plate size of 17 μm as demonstrated in Fig. 5.1(a).

Fig. 5.1. (a) Optical micrograph of as-received Ti64. (b) Extruded Ti64 after a single pass at 800 °C.

Prior to extrusion, Ti64 rods were inserted into 25.4×25.4 mm cross section stainless steel cans and were heated to 800 °C (0.55 T_m) for 1 hour. ECAE was conducted non-isothermally at an extrusion rate of 12.7 mm/sec corresponding to an approximate strain rate of 1 s^{-1}, using a 90° angle die, preheated to 300 °C. Multiple ECAE passes were performed without billet rotation between the passes (route A). Following the extrusion, the billets were water quenched to assist in maintaining the microstructure

achieved during ECAE. Fig. 5.1(b) demonstrates a single pass extruded billet without any indication of localized deformation.

Samples for room temperature tension and compression experiments were prepared such that the tension samples were oriented parallel to the extrusion direction and the compression samples were oriented perpendicular to the extrusion direction. Fig. 5.2 illustrates the orientations of the samples with respect to the extrusion direction. The strain in all instances was measured using a miniature 3 mm gage length extensometer. A strain rate of 10^{-3} s^{-1} was applied during both tensile and compressive loading.
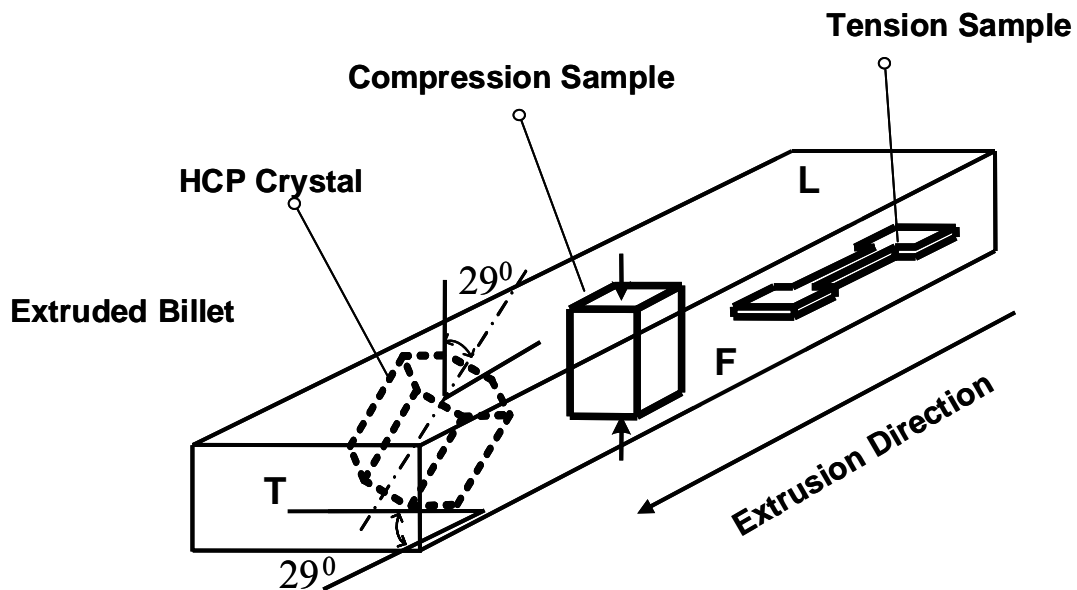
Fig. 5.2. The schematics of the Ti64 tension and compression samples cut from the extrudates showing their orientation with respect to the extruded billet. The representative hcp crystal demonstrates the orientation of the basal poles with respect to the billet coordinate system after ECAE.

5.3. Microstructural Evolution

The as-received material has a coarse lamella colony α structure without distinct prior β phase boundaries as shown in Fig. 5.3. The α colonies have near equiaxed morphology with lamellar plates separated by thin β strips. TEM observations (Figs. 5.4

through 5.7) on the samples processed at 800°C following route A single pass (1A) and two passes (2A) revealed an apparent deformation twinning activity. The propensity of twinning increases with the number of ECAE passes as evidenced by the higher volume fraction of the fine twin structure in the 2A sample (Figs. 5.6 and 5.7). Indexing the selected area diffraction (SAD) patterns from the twinned regions revealed that all the twins observed in both the 1A and 2A samples are from the $\{10\bar{1}1\}$ twin system. In addition, twin intersections of different variants of the same mode in the 2A sample display the severity of twinning (Figs. 5.6 and 5.7). The twin thickness is less than 30 nm and multiple twin variants form a nano-twin network.

Extensive TEM observations on multiple thin foils from the different regions of the billets demonstrated that the $\{10\bar{1}1\}$ twinning is the only twin mode observed and acts as an important deformation mechanism. No other significant twin modes were detected. The volume fraction of twins after the first ECAE pass is estimated to be around 10 to 15%, while after the second pass this ratio reaches almost 30-40%. The average α grain size, α plate thickness and β grain size calculated from optical micrographs and TEM images are tabulated in Table 5.1.

Increase in the propensity of twinning with number of passes has two implications. Firstly, although the extrusion temperature is very high, the dynamic recovery/recrystallization seems not to be very effective in fully annealing the deformation twinning structure and the formation of large recrystallized grains. Therefore, the second pass leads to further twinning to accommodate applied strain possibly because of the hardening of slip systems, i.e. higher strength levels lead to the formation of mechanical twinning [208, 209]. This demonstrates that the microstructure achieved after one pass must be relatively thermally stable. Secondly and more importantly, the crystallographic texture achieved after one pass may be more favorable for twinning activity during the second pass as compared to the initial random texture.

In contrast to commercial purity Ti where twinning is occasionally observed in quasistatic loading at ambient temperature, mechanical twinning in Ti64 has not been observed except when the strain rate is very high as in shock loading experiments [210, 211] or when the deformation takes place at cryogenic temperatures [211, 212]. This

might be due to the fact that in general, alloying additions of both substitutional and interstitial elements such as Al and O suppress twinning in Ti [144, 213] More recently, Williams et al. [144, 213] showed that compression twinning becomes increasingly hard to nucleate in Ti-Al single crystals with Al content above 5 wt. %. Johnson et al. [210] revealed that occurrence of deformation twins in Ti64 increases at high strain rates and/or low temperatures. This was attributed to the increase in flow stress at high strain rates and low temperatures [210]. Liu et al. [214] studied the microstructural evolution on the surface layer of Ti64 after sliding wear experiments. At low sliding velocities, the surface layer consisted of a fine grained structure with high dislocation density. In contrast, at higher velocities, many deformation twins were observed pointing the effect of strain rate on the twin nucleation. All of these studies demonstrated that the nucleation of deformation twinning in Ti64 is highly stress and strain rate dependent.
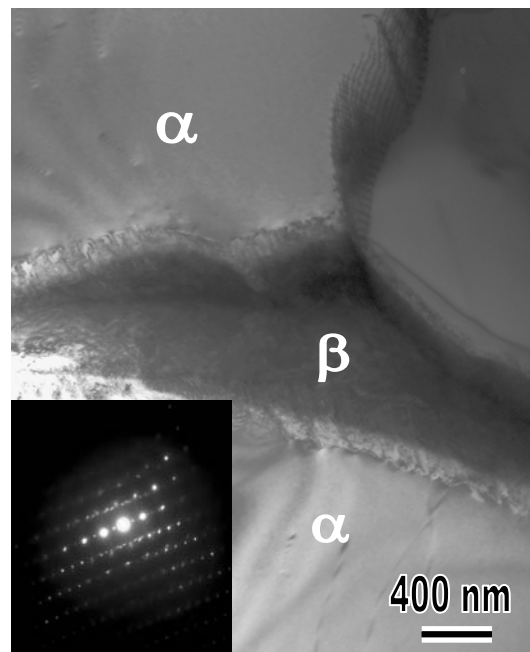
Fig. 5.3. Bright-field TEM image of the as-received Ti64, demonstrating regions of α and β phases.

Table 5.1

Summary of the results of the mechanical experiments conducted at room temperature and the evolution of microstructural size parameters before and after ECAE of Ti64. σ_y: yield strength; ε_f: tensile fracture strain; $d\sigma/d\varepsilon$: strain hardening coefficient, UTS: ultimate tensile strength.

Processing Conditions	Microstructural Parameters			Tension Experiments				Compression Experiments	
	Average α grain size (nm)	Average α plate thickness (μm)	Average β grain size (nm)	σ_y (MPa)	UTS (MPa)	ε_f (%)	$d\sigma/d\varepsilon$ (MPa)	σ_y (MPa)	$d\sigma/d\varepsilon$ (MPa)
As Received	-	17 ± 3.5	330 ± 18	911 ± 15	1182 ± 8	19.5 ± 0.8	1408 ± 25	1021 ± 21	2417 ± 32
800°C, ECAE 1A	425 ± 30	9.7 ± 0.4	105 ± 9	941 ± 25	1149 ± 11	5.6 ± 0.4	2953 ± 36	1088 ± 13	2539 ± 28
800°C, ECAE 2A	350 ± 22	7.3 ± 0.3	115 ± 13	1040 ± 12	1257 ± 16	9.1 ± 0.5	3078 ± 30	1285 ± 17	3241 ± 23

(a)

(b)

(c)
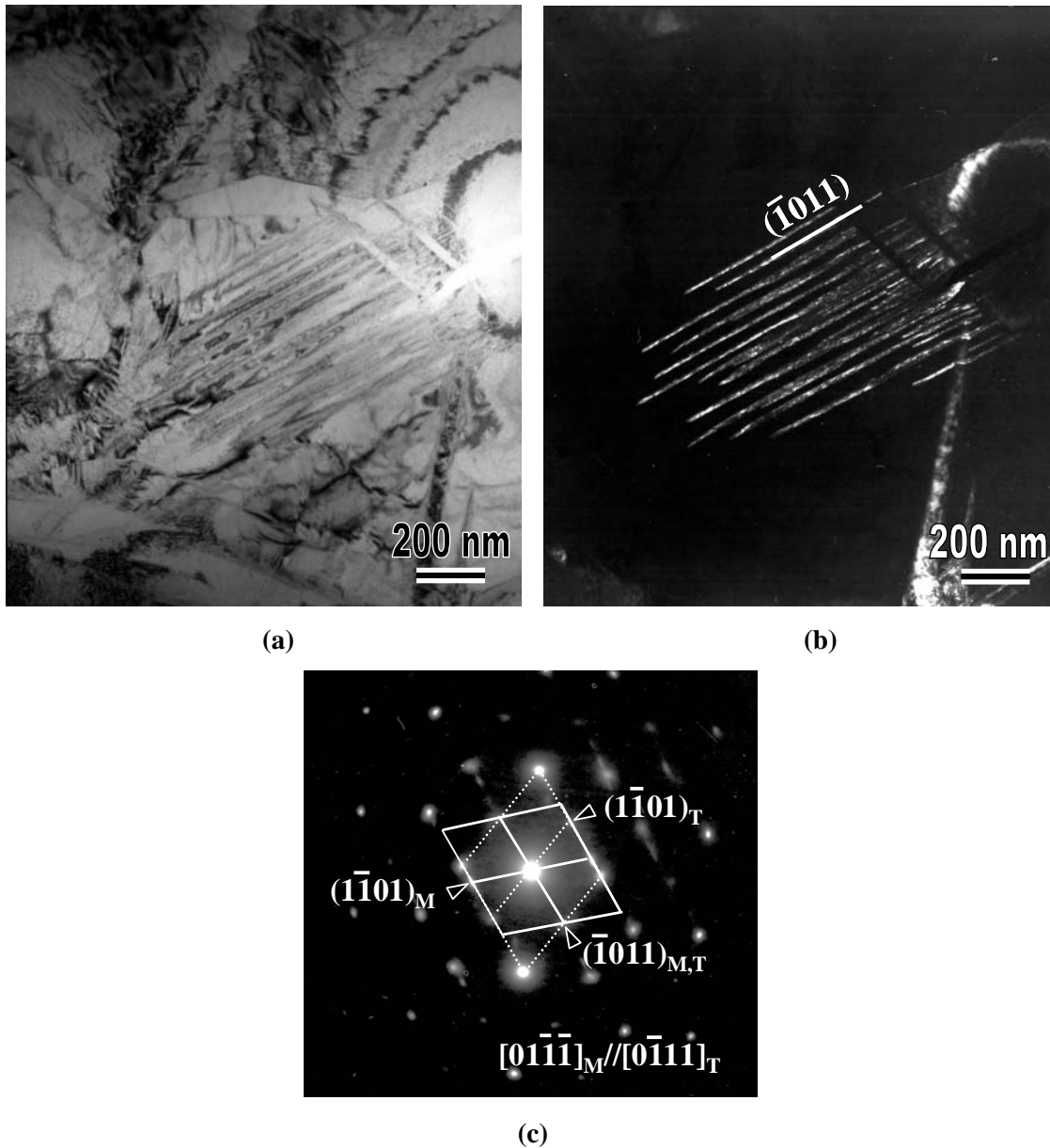
Fig. 5.4. (a) Bright-field TEM image of Ti64 after one ECAE pass at 800 ^{o}C. (b) Corresponding dark-field image displaying a fine twin system. The diffraction pattern in (c) is taken from the twinned region in (a), with the reciprocal vector $\mathbf{g}_{\bar{1}011}$ perpendicular to the twining plates in the image. The twinning plane is identified as $(\bar{1}011)$. The subscript M stands for the matrix and T is for twins.
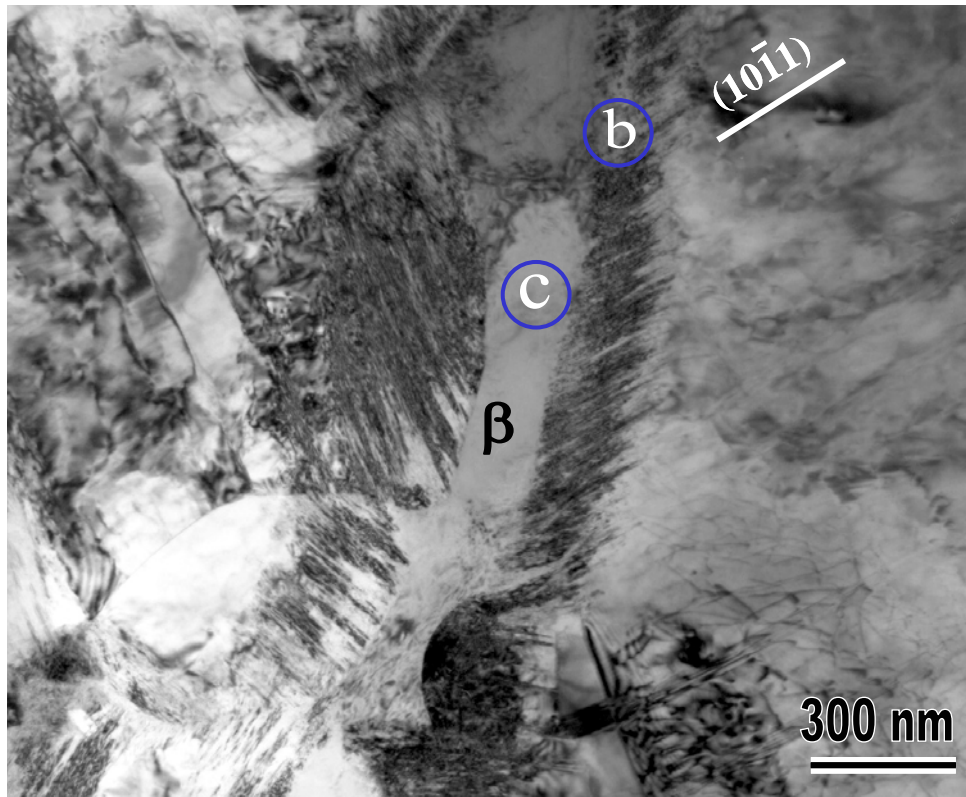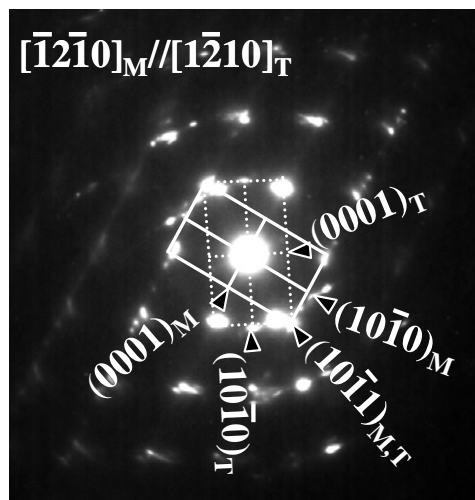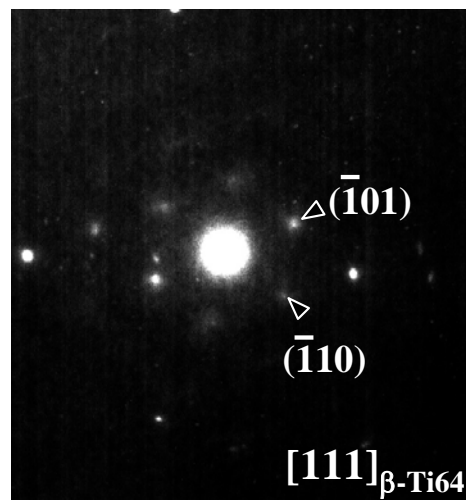
Fig. 5.5. (a) Bright-field TEM image of Ti64 after one ECAE pass at 800 $^{\circ}$C; (b) diffraction pattern taken from the circled area marked with a letter b in (a), displaying twins on the $(10\bar{1}1)$ plane; (c) diffraction pattern from the β phase with no twins.
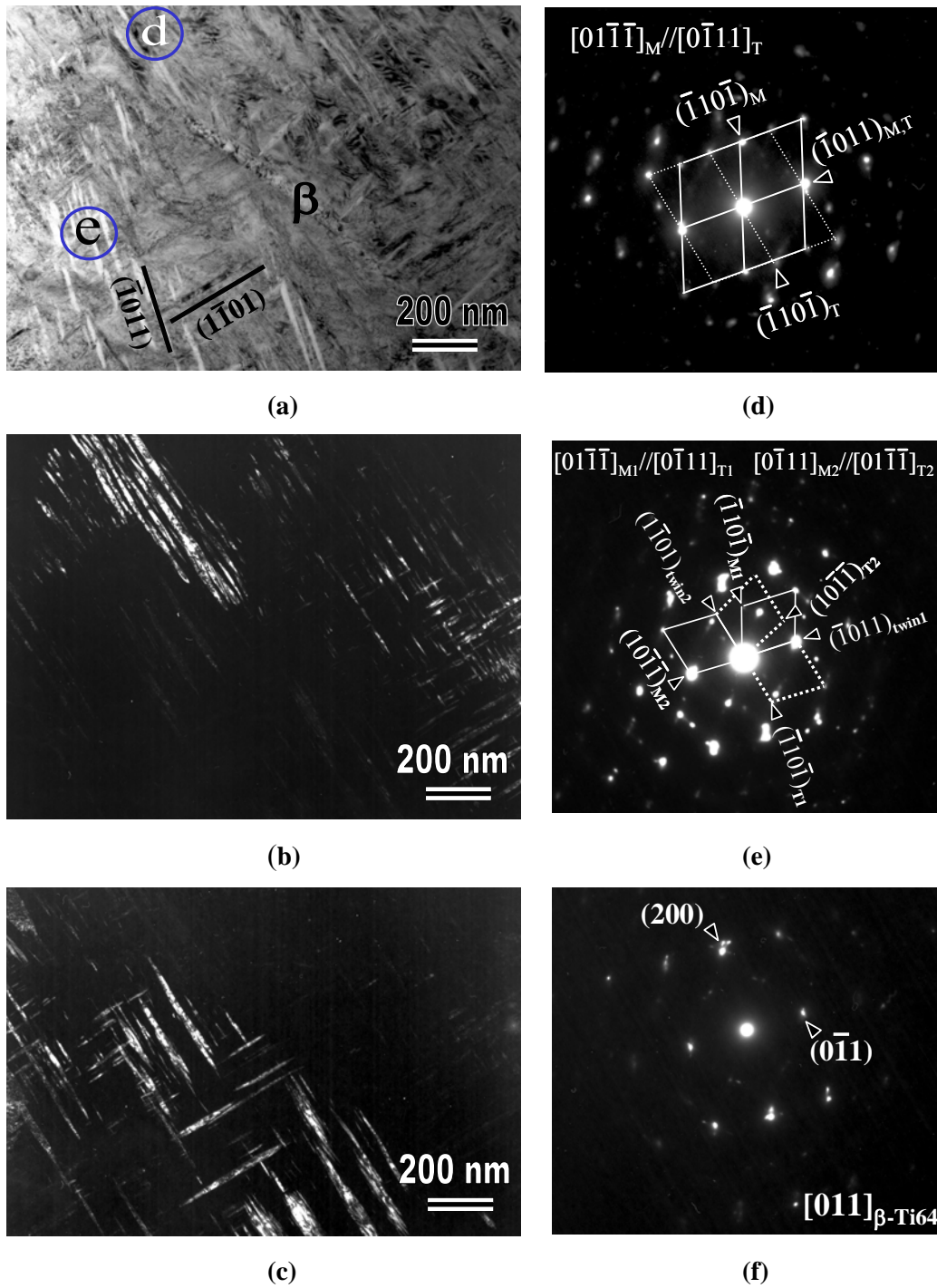
Fig. 5.6. (a) BF TEM image of Ti64 - ECAE 2A at 800 °C. The DF images in (b) and (c) show fine twins in the two α grains above and below the β phase, respectively. The DP in (d) is from the area d in (a), identifying twins from the $(\bar{1}011)$ plane; and the DP in (e) is from the area e in (a), showing two twin systems, $(\bar{1}011)$ and $(1\bar{1}01)$. The DP in (f) is taken from the β phase separating the two α grains as indicated in (a).
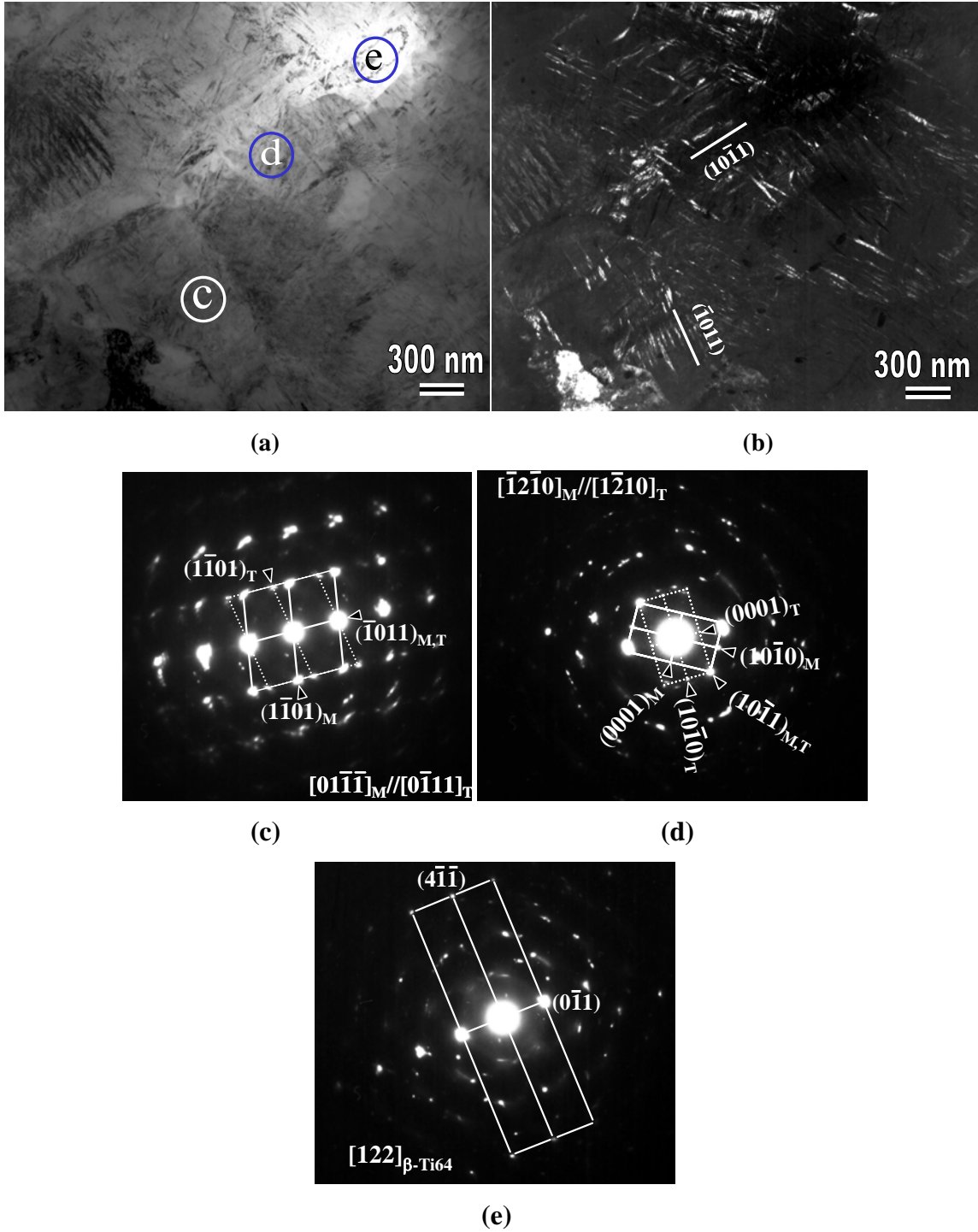
Fig. 5.7. (a) BF TEM image of Ti64 after two ECAE passes at 800 °C, following Route A. (b) DF image showing twins. (c) DP from the circled area c in (a), exhibiting twins on the $(\bar{1}011)$ plane. (d) The DP from the circled area d in (a), displays twins on the $(10\bar{1}1)$ plane. (e) The DP from the β phase separating the two α grains.

It should be emphasized that twinning in Ti64 at such high temperatures and moderate strain rates is reported for the first time. There has been only one study demonstrating twinning activity during quasistatic deformation of Ti64 at ambient temperature [214]. Although twinning is not usually expected at room temperature under quasistatic loading, the aforementioned study utilized samples with very strong transverse texture, stressing the importance of texture on the activation of mechanical twinning in unexpected conditions

The present twinning mode was also observed in Ti single crystals above 400 °C under compression loading parallel to c axis [44]. This activity was attributed to the fact that, while twin nucleation stress for $\{11\bar{2}2\}$ twins (another compressive twin mode) continues to rise with increasing temperature; twinning stress for $\{10\bar{1}1\}$ twinning decreases with increasing temperature in contrast to most hcp twinning modes [41, 44, 105]. Thus, Paton et al. [44] reported $\{11\bar{2}2\}$ twins below 300 °C and $\{10\bar{1}1\}$ twins above 400 °C, and the activity of $\{10\bar{1}1\}$ twins disappeared at temperatures above 800 °C. The only other study where $\{10\bar{1}1\}$ twinning was activated as a major deformation mechanism was during ECAE processing of CP Grade 2 Ti at 350 °C [215].

5.4. Mechanical Behavior after ECAE

Room temperature monotonic experiments on the ECAE processed samples exhibited increased tensile and compressive yield strengths compared to the as-received material as shown in Fig. 5.8 and Table 5.1. The higher tensile and compressive yield strengths of the 2A sample as compared to that of the 1A sample are notable. Moreover, higher ductility of the 2A sample in spite of being heavily worked is interesting (Fig. 5.8(a)). Follansbee et al. [211] reported that increased twinning activity during high strain rate deformation of Ti64 at room temperature coincided with decreased dislocation density, because of the role of twinning as a shear accommodation mechanism. This could increase the dislocation storage ability, providing higher ductility to the material. The higher ductility in the 2A sample could also be related to the refined α grain size and deformation accommodation due to grain boundary moderated mechanisms.
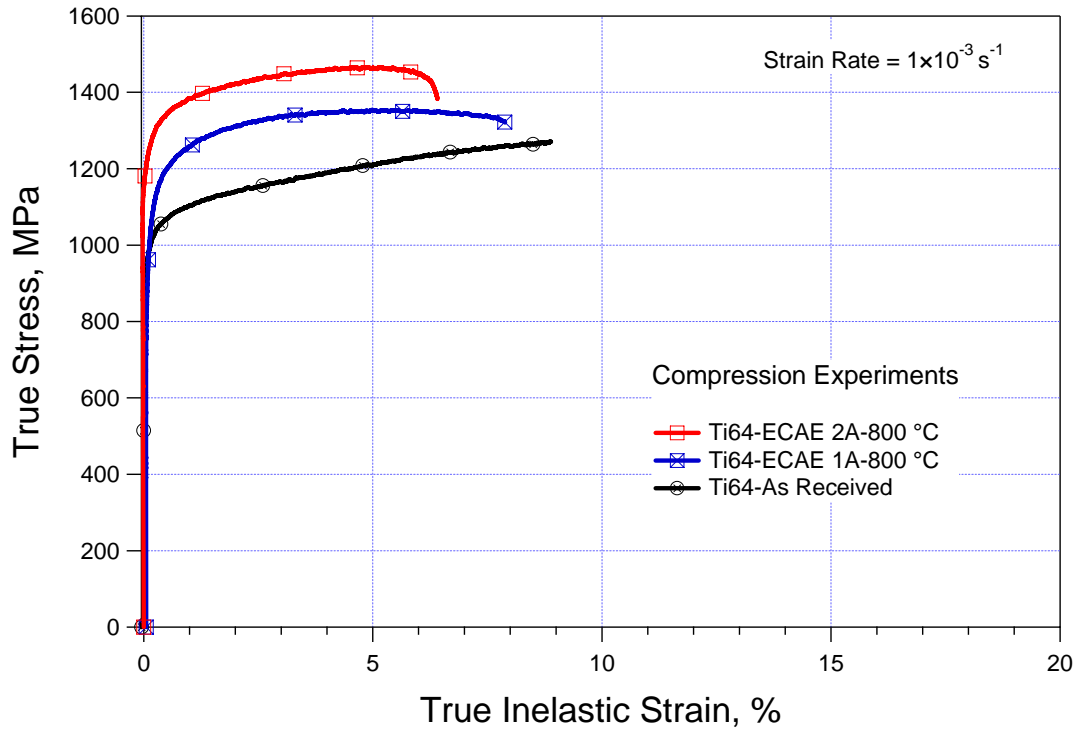
(a)
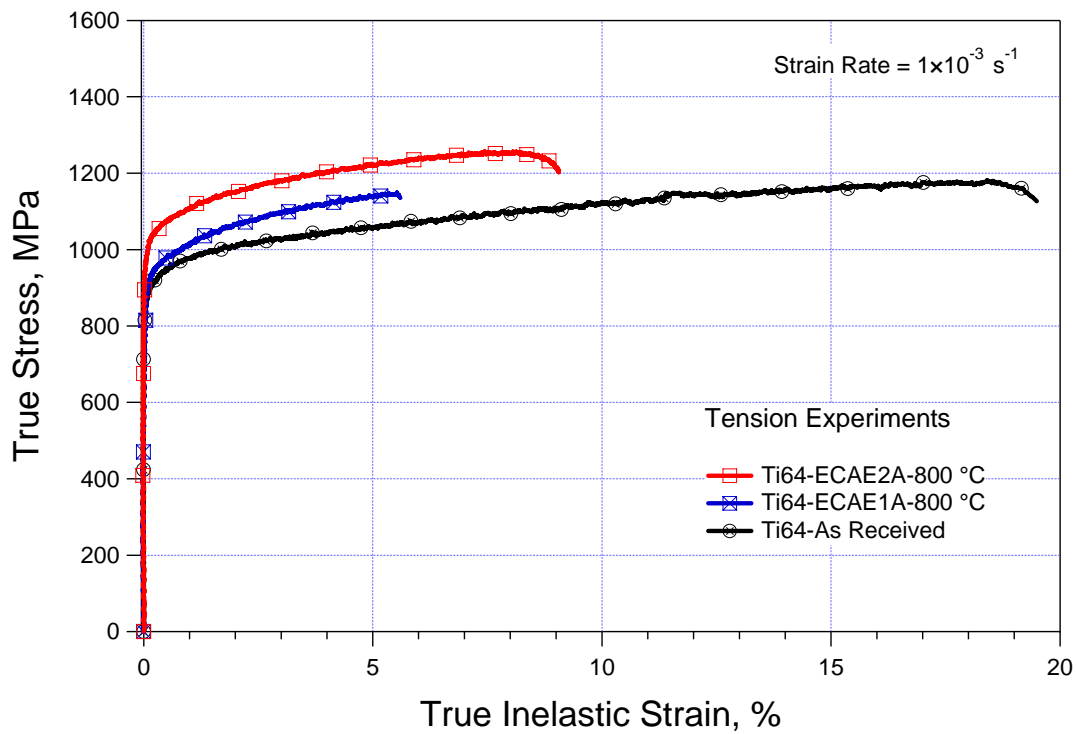
(b)

Fig. 5.8. (a) Tensile and (b) compressive true stress – true inelastic strain response of the as received and ECAE processed Ti-6Al-4V samples at room temperature.

Twin-twin and twin-slip interactions result in higher work hardening rate in the ECAE processed materials as compared to the work hardening in the as received material. In addition to mechanical twinning, grain refinement also contributes to the strength levels achieved in the present study since there is a significant refinement in the α grain and plate sizes as compared to the as-received material (Table 5.1). However, profuse twinning could contribute more to the high flow stress, since the considerable increase in the flow stress during the second pass can be easily correlated with the increase in the twin volume fraction.

Moreover, twin boundaries are known to act as slip obstacles leading to a so called effective grain size causing a similar effect with grain refinement. Considering that the twin thickness and the distance between the twin plates are on the order of few tens of nanometers (Figs. 5.6 and 5.7), twin boundaries may contribute to the strengthening significantly.

5.5. Crystallographic Texture Evolution during ECAE

Macro-texture evolution of Ti64 after one and two ECAE passes at 800 °C is presented in Fig. 5.9 using (0001) pole figures. Fig. 5.9(a) clearly displays a nearly random texture in the as received material.

After one ECAE pass, it can be seen that the basal poles were tilted towards the longitudinal direction (LD), making an angle of about 61° with the extrusion direction (ED) as shown by the orientation of the hcp crystal in Fig. 5.2 and by the pole figure in Fig. 5.9(b)). This texture evolution demonstrates that the basal planes are almost aligned with the long axes of the elongated grains which are shown to be 27° from the extrusion direction for the ECAE die used in the present study [186, 216]. The second pass extrusion tilted the c axes further towards the longitudinal direction. The low intensity components around the extrusion direction present after the first ECAE pass almost disappeared after the second pass as illustrated in Fig. 5.9(c). With these crystallographic texture features, single pass ECAE of Ti64 resembles that of pure Ti after one ECAE pass at 350°C [181, 215]. The deformation mechanisms leading to the observed texture evolution are addressed in Section 5.7.3.
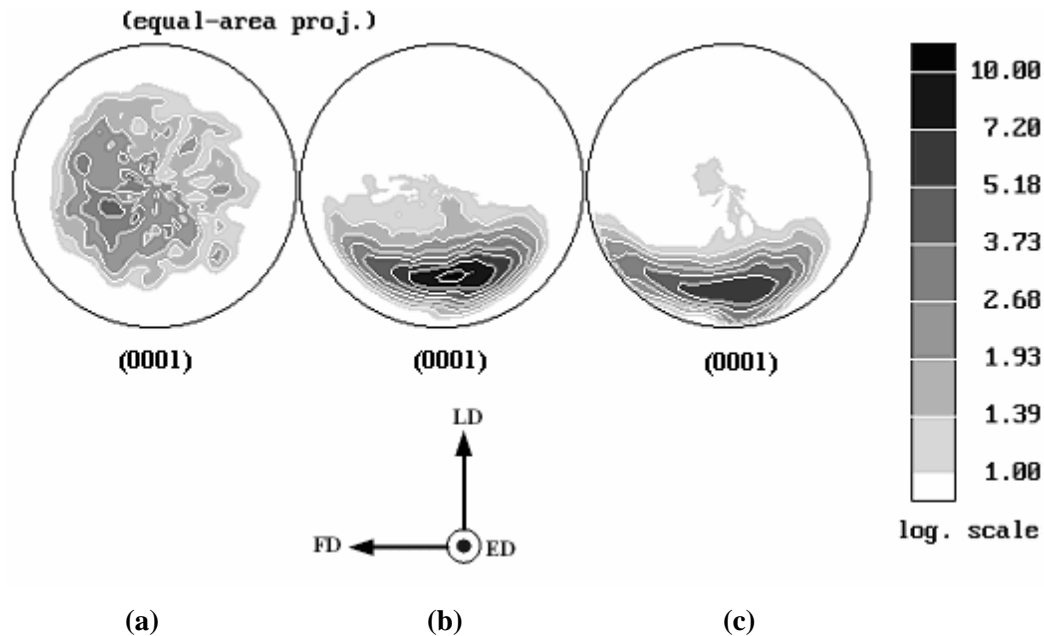
Fig. 5.9. Experimental (0001) pole figures of (a) as-received, (b) one pass ECAE, and (c) two passes ECAE processed Ti64. ED: Extrusion Direction; LD: Longitudinal Direction; and FD: Flow Direction.

5.6. Directional Anisotropy in Tension-Compression Response

There is a considerable variation in the yield strength levels during the tension/compression (T/C) experiments. The magnitude of this variation increases with the number of passes (Table 5.1). This variation is referred as a "T/C directional anisotropy" in yield strengths since the tension and compression experiments were conducted on samples oriented perpendicular to each other. This anomaly can not be attributed solely to the resulting ECAE texture and its effect on the activation of various deformation mechanisms during the straining of the tension and compression samples with different initial orientations (Fig. 5.2). This is because of the increase in the magnitude of the directional anisotropy even though texture does not change considerably between the passes. Factors other than texture should be in effect to explain this phenomenon. The reasons for this anomaly are discussed in more detail in Section 5.7.2.

5.7. Discussion

In the present study, the powder processed Ti64 with coarse lamella colony α structure was exposed to SPD via ECAE at $0.55T_m$. Significant amount of deformation twins with the $\{10\bar{1}1\}$ twin plane was observed and the volume fraction of the twins increased with increasing number of the ECAE passes. Twinning is not usually expected in Ti64 at high temperatures and low to moderate strain rates. In this section, some of the possible mechanisms are discussed to elucidate the rationale for the unexpected twinning at such high temperatures and a simple mechanistic model is proposed considering the effect of applied stress on the partial dislocation separation.

The ECAE process also led to the alignment of the basal planes with the long axes of the elongated grains. Deformation mechanisms that are responsible for this texture evolution are discussed in the following sections. A VPSC crystal plasticity framework will be used to reveal the relative importance of certain deformation mechanisms, in particular specific twinning modes on the aforementioned texture evolution. A significant directional anisotropy during tension/compression experiments was observed in the room temperature monotonic experiments. The impact of the processing induced deformation microstructure and resulting texture on the T/C anisotropy is also discussed.

5.7.1. Mechanism of Deformation Twinning at High Temperatures

Although pole mechanisms for twin nucleation in hcp metals were proposed earlier [126], it is found more recently that they are only able to account for twin growth [41]. Twin nucleation mechanisms in hcp crystals can be grouped into two types: homogeneous and heterogeneous. Homogeneous nucleation concepts dictate that a twin is created by homogeneous lattice shear in a region of high stress concentration [122]. $\{10\bar{1}2\}$ twins in zinc have been explained using this mechanism [129]. Twin formation due to non-planar dissociation of slip dislocations is suggested as a heterogeneous nucleation mechanism [217, 218]. Atomistic simulations for the nucleation of $\{11\bar{2}1\}$ twins in the hcp lattice demonstrated the possibility of such a mechanism [219]. Here, a possible mechanism for the nucleation of $\{10\bar{1}1\}$ twinning at high temperatures

considering the non-planar dissociation concept and the effect of applied stress on twin partials is discussed.

The occurrence of $\{10\bar{1}1\}$ twinning at high temperatures is attributed to the high stress and strain levels and strain rate imposed during ECAE, along with the favorable texture evolved during deformation. However, it was reported that the $\{10\bar{1}1\}$ twinning mode observed in low strain rate deformation in Ti provides a shear strain of only about 0.15 [44, 105]. With such a low shear strain compared to that of ECAE (~ 2 in each pass), it is clear that twinning mode active during ECAE must be different than that of observed under conventional deformation conditions and strain levels. Kim et al. [220] studied the different modes of $\{10\bar{1}1\}$ twinning in Ti and found out the modes with higher shear strains up to 1.2 during ECAE of Ti at 350°C. These modes are different from the previously observed $\{10\bar{1}1\}$ twins since they possess highly distorted core configuration leading to high interfacial energy. It is believed that similar $\{10\bar{1}1\}$ twin modes with high shear strain levels should also be operational in the present case. Activation of these special modes must have been promoted by the high stress levels reached during ECAE, since twins with high shear strains and high interfacial energy are difficult to nucleate.

It should be noted that although $\{11\bar{2}2\}$ twins have a higher twinning shear, $\{10\bar{1}1\}$ twinning was the only mode observed. This may have two implications. Firstly, the applied stress may favor the separation of the $\{10\bar{1}1\}$ twin partials while opposing that of the $\{11\bar{2}2\}$ partials because of texture. This possibility arises from the argument that high stress levels can affect the separation distance between twinning partial dislocations creating so called an effective stacking fault energy as explained below. Secondly, the attained stress level may not be high enough to activate $\{11\bar{2}2\}$ twins as the critical stress for $\{11\bar{2}2\}$ twin activation is a strong function of temperature [41, 44].

Under low strain loading conditions where the stress levels are low, and at high temperatures, Ti64 can easily cross-slip out of the basal plane with its relatively high

stacking fault energy (SFE). However at high strain rates and/or some other loading conditions where high stress levels can be achieved, the SFE might be altered due to the effect of applied stress on the partial dislocation separation. In fcc materials, the applied stress plays a significant role on partial dislocation separation resulting in an effective SFE. Marcinkowski and Miller [221] and later Copley and Kear [222] showed that in low SFE fcc materials, the applied stress changes the equilibrium separation distance of the Shockley partials. Since the partial dislocation separation and the SFE are inversely related, the applied stress creates an effective SFE as experimentally shown in low SFE austenitic stainless steels [223, 224]. Depending on texture and the stress level, the effective SFE can be quite low and lead to twin nucleation as observed in several occasions [187, 198].

This idea can also be extended to hcp materials. $\{10\bar{1}1\}$ twins can be nucleated in two energetically possible ways where non-planar dissociations occur [217, 218]. First, the AB 60° dislocations on the basal plane can dissociate into single or symmetric twinning partials on the $\{10\bar{1}1\}$ planes, as given by Eqs. (11) and (12) below, respectively. This process is described by a schematic in Fig. 5.10(a). Another reaction that makes $\{10\bar{1}1\}$ twinning possible is the dissociation of the [AB+φθ] screw dislocations on the $\{\bar{2}112\}$ planes into twinning partials on the $\{10\bar{1}1\}$ planes as shown in Eq. (13) [218].

$$\left(\frac{1}{3}[\bar{2}110]\right)_{(0001)} \rightarrow [\bar{1}012]_{(\bar{1}01\bar{1})} + \left(\frac{1}{3}[\bar{2}110]+[10\bar{1}0]+2[000\bar{1}]\right)_{(0001)} \quad (11)$$

$$\left(\frac{1}{3}[\bar{2}110]\right)_{(0001)} \rightarrow [\bar{1}012]_{(\bar{1}01\bar{1})} + [\bar{1}01\bar{2}]_{(\bar{1}01\bar{1})} + \left(\frac{1}{3}[\bar{2}110]+2[10\bar{1}0]\right)_{(0001)} \quad (12)$$

$$\left(\frac{1}{3}[\bar{2}110]+[0001]\right)_{\{\bar{2}112\}} \rightarrow [\bar{1}012]_{(\bar{1}01\bar{1})} + \left(\frac{1}{3}[\bar{2}110]+[10\bar{1}0]+[000\bar{1}]\right)_{\{\bar{2}112\}} \quad (13)$$

In Eqs. (11) and (13), the first group of Burgers vectors on the right hand side is the single twinning partial on the $(\bar{1}01\bar{1})$ plane, while the second group of Burgers vectors represents the residual dislocations on the initial slip plane [217, 218]. In Eq. (12), the first two terms on the right are the symmetric twinning partials on their

respective planes, and the last group of terms corresponds to the stair rod dislocation formed along the line of intersection of the planes where dissociation takes place [217, 218].
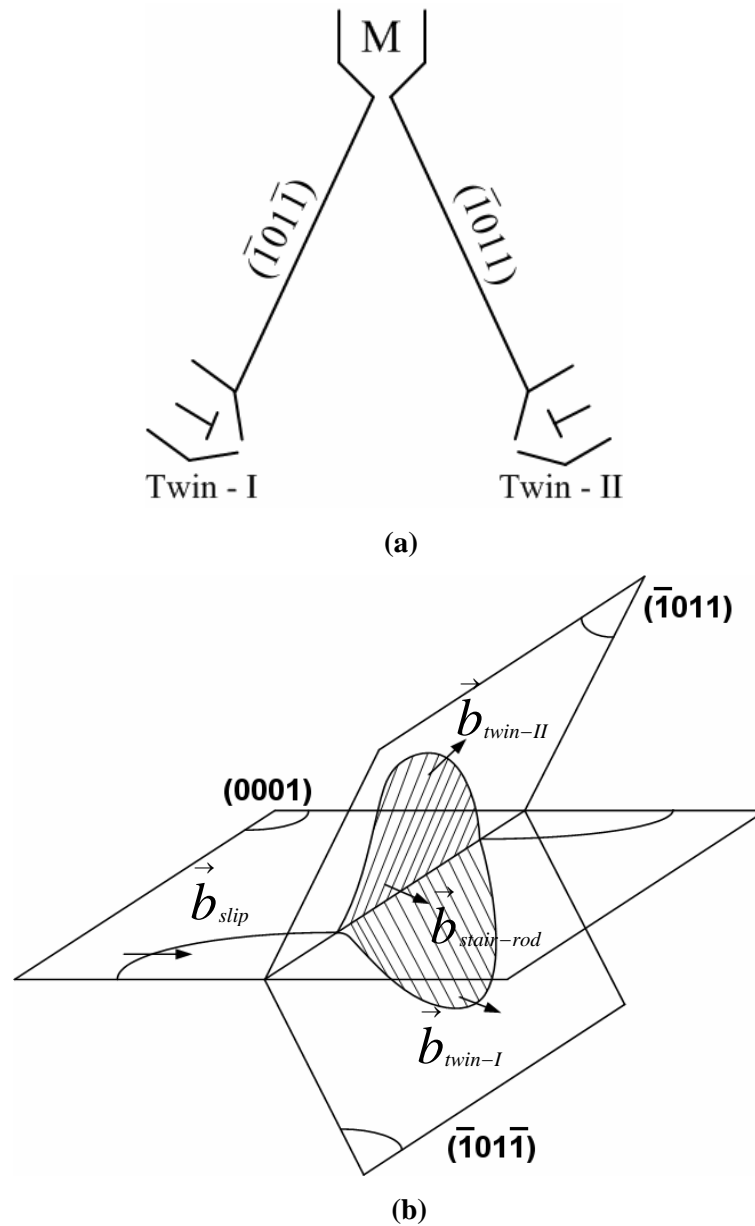
Fig. 5.10. Schematics of (a) the dissociation of AB 60° dislocations on the basal plane into symmetric twinning partials on the $\{10\bar{1}1\}$ planes; M symbol at the stair rod represents the mixed dislocation and (b) the symmetric non-planar dissociation mechanism.

Since the formation of $\{10\bar{1}1\}$ twinning requires dissociations on oblique planes; for the conservation of Burgers vectors, a residual stair rod dislocation is formed along the line of intersection between the initial glide plane and the twinning plane(s) as seen in Fig. 5.10(b). However, climb or glide of the stair rod dislocations require the formation of high energy fault and therefore are generally sessile. Thus, if the externally applied stress is high; the separation distance between the twinning partial and stair rod dislocation may change leading to a decrease or increase in the effective SFE. [43, 217, 218].

It is argued that during ECAE, high applied stress level increases the separation distance between the twinning partials and the stair rod dislocation. Therefore, twinning is more readily nucleated. The validation of this argument is simply possible if one can demonstrate a higher Schmid factor on the $\{10\bar{1}1\}$ twin partials during ECAE processing. Considering the dissociation presented in Eq. (11) and texture developed during the first ECAE pass, the twin partial on the $(\bar{1}01\bar{1})$ plane has a Schmid factor close to the maximum value of 0.5 during the second ECAE pass following route A. On the other hand, for example, further rolling of an hcp crystal with an existing strong rolling texture results in a Schmid factor of 0.42 for the same partial. Moreover, stress level reached during ECAE is generally higher than conventional processing methods because of the ease of imposing higher uniform strains. Thus, there is higher resolved shear stress on the twin partials during the second pass ECAE. This increases the separation distance between the sessile stair rod dislocation and the glissile twin partial possibly leading to the activation of twinning even at high temperatures.

Deformation twinning at high temperatures during ECAE is not unique to Ti64. The extensive activity of deformation twinning in low SFE fcc materials, such as 316L stainless steel, during ECAE at high homologous temperatures (>0.65 T_m) was also rationalized with a similar mechanism [208]. Indeed, deformation twinning in high SFE Al with nanograins was also attributed to the effect of high applied stress levels on the effective SFE [225, 226]. It should be noted that the present proposed mechanism is difficult to validate experimentally for hcp crystals and requires detailed TEM investigation. However, it is believed due to the similarities with other materials we have

studied under SPD conditions with different crystal structures that twinning can be a major deformation mechanism in unexpected conditions if high stress levels are achieved.

5.7.2. Mechanisms for Directional Anisotropy of Flow Strengths

There is a clear directional anisotropy between the yield strengths of the processed materials under tensile and compressive loading (Fig. 5.8). The magnitude of this directional anisotropy gets larger after the second ECAE pass. Two possible factors that may be responsible for the observed directional tension/compression (T/C) anisotropy are crystallographic texture and the processing induced deformation structure. During ECAE, the basal poles rotate towards the longitudinal direction and the prism poles rotate towards the extrusion direction of the extruded billets. It is important to note that the tension samples were oriented parallel to the extrusion direction and compression samples were oriented parallel to the longitudinal direction as previously shown in Fig. 5.2. Considering the loading directions and ECAE texture, the Schmid factors for tension and compression experiments were calculated using Los Alamos Polycrystal Plasticity (LaPP) code (a Taylor-based code) [146] and tabulated in Table 5.2.

According to Table 5.2, the slip modes have similar Schmid factors under both tension and compression, and thus, they should not cause any directional anisotropy assuming that no significant differences are present between the critical resolved shear stress (CRSS) levels of the different slip modes under tension and compression. If the CRSS levels of tension and compression twins are similar, then, one would expect higher twinning activity and lower yield strength under compression since the compression twin mode has higher Schmid factor than tension twins. However, the compression samples showed higher yield strength levels. In this argument, the prismatic slip was not considered as it is not expected to play an important role due to its low Schmid factor as compared to other slip modes.

It was reported that in rolled Ti64 samples [227, 228] along basal poles, compressive yield stresses are higher than tensile yield stresses because the CRSS for pyramidal <c+a> glide (main deformation mode along this texture) differs upon reversal of the load. In the present case, the same could be expected. Since the Schmid factors for main slip modes are the same for loading under both tension and compression, even

though loading directions (textures) are different, the reason for the present directional T/C anisotropy could be the asymmetry in the CRSS levels of the different deformation modes. Therefore, texture should not be the reason for the observed directional anisotropy. However, the asymmetry in the CRSS levels may not be the only reason either because the magnitude of directional anisotropy increases with the number of passes although the texture and thus Schmid factors do not change noticeably. This last argument assumes that the asymmetry in the CRSS levels does not change considerably with deformation.

Table 5.2

Maximum Schmid factors for the possible deformation mechanisms during tension and compression testing of the ECAE processed samples with the consideration of the resulting ECAE texture. CT: Compression Twin, TT: Tension Twin.

Mechanical Experiments	Active Deformation Mechanisms			
	Prism	Basal	Pyramidal $<a>$	Pyramidal $<c+a>$
Tension Experiments	0.33	0.36	0.45	0.44
Compression Experiments	0.1	0.36	0.45	0.46
Mechanical Experiments	$\{10\bar{1}1\}$ CT	$\{11\bar{2}2\}$ CT	$\{10\bar{1}2\}$ TT	$\{11\bar{2}1\}$ TT
Tension Experiments	0.13	0.11	0.39	0.04
Compression Experiments	0.45	0.34	0.12	0.21

It is recently shown that the different mechanical behavior of the ECAE processed copper samples during T/C experiments can not also be explained by only texture and strongly depends on the nature of the processing-induced deformation structure, i.e. type of grain/subgrain boundaries [196]. In the present work, it is claimed that the directional T/C anisotropy at room temperature in the ECAE processed Ti64 samples should also depend on processing induced deformation twin boundaries, dislocation substructures and boundary character since texture and the asymmetry in the CRSS levels can not explain this anomaly adequately.

In the present case, it is expected that compression of ECAE processed Ti64 results in a higher mechanical twinning activity compared to that of during tension tests due to the resulting texture and the orientation of the mechanical testing samples. This rationale can be supported by comparing the Schmid factors for tension and compression experiments of the ECAE processed Ti64. According to their Schmid factors, the most favorable deformation systems in tension are pyramidal <a> and pyramidal <c+a> slip, while in compression $\{10\bar{1}1\}$ twinning, pyramidal <a> and pyramidal <c+a> slip can be activated with almost equal importance (Table 5.2). This means an easier activation of twinning during compression considering that no distinction is made between the critical shear stress levels of the different deformation modes. Higher twin activity under compression would lead to higher flow stresses. The higher strain hardening of 2A sample in compression can be attributed to the pronounced twin-twin and twin-slip interactions.

It was reported that either $\{10\bar{1}2\}$ or $\{11\bar{2}1\}$ twinning is activated in samples with tensile loading axis perpendicular to the basal plane[214]. These twinning modes aide prismatic slip. In the present study, the majority of the grains have their c axes aligned 61° to the tensile loading direction. Thus, under tension, one might expect a lower twinning activity composed of $\{10\bar{1}2\}$ and $\{11\bar{2}1\}$ tension twins. In addition, these tension twins are much more glissile than the $\{10\bar{1}1\}$ compression twins and will cause less strengthening during tensile loading compared to that obtained during compressive loading leading to a difference in tensile and compressive flow strengths.

Another reason for the higher twinning activity during compression near c axis can be due to a change in the volume fraction of the second phase during ECAE. Zaefferer [229] concluded that the cubic β phase plays an important role in strain accommodation during deformation along c axis. Therefore, the lower the volume fraction of the β phase is, it is more likely to activate twinning modes in α to accommodate the applied strain. It was reported that ECAE of Ti64 at 700 °C results in a decrease in the volume fraction of the β phase up to 8% [230]. It was also shown that the β phase fragments during ECAE of Ti64 forming clusters instead of a continuous phase in between α grains [186]. Gey et al.[231] demonstrated that increase in dislocation density of {110} planes of β phase favors the transformation of β to α. Thus, deformation twinning in the present compression experiments could also be promoted by the reduction in the volume fraction of β phase during ECAE increasing the need for twinning to accommodate the applied strain.

5.7.3. Modeling of Texture Evolution during ECAE

Accurate prediction of texture evolution is essential for understanding the responsible mechanisms for plastic deformation of Ti64 during ECAE. The VPSC model is utilized for this purpose. As mentioned earlier, one of the main inputs of the code is the set of active deformation systems and their respective CRSS values. Among the slip modes available in α Ti, only pyramidal glide on the $\{11\bar{2}2\}$ plane was not included in the present simulations, because it is rarely observed during axial deformation and rolling of Ti64 [194]. Among the twinning systems, the effect of each system on the texture evolution is identified by including one at a time to assist slip systems. Specifically, simulation efforts were centered on the $\{10\bar{1}1\}$ twinning system, since it is the only major twin mode active during ECAE of Ti64. Both slip and twinning systems were assumed to operate without hardening. Below, the deformation systems considered in the simulations and the rationale on selecting their CRSS values are explained.

Earlier studies on titanium single crystals concluded that prismatic slip is the preferential deformation mode [192, 193]. TEM studies on a cold-rolled α Ti alloy also showed that prismatic slip is the easiest system to activate and pyramidal slip along

<c+a> is the hardest [194]. Moreover, the CRSS difference between prismatic and basal slip in Ti decreases as the temperature increases. On the other hand, addition of aluminum to Ti increases the CRSS of prismatic glide [232]. Therefore, during high temperature deformation (800 °C) of Ti64, one could expect similar CRSS levels for prismatic and basal slip. Moreover, uniaxial loading of Ti64 showed that <a> dislocations on prismatic, basal and pyramidal planes can glide with almost equal ease [233]. It was also reported that basal slip and $\{11\bar{2}2\}$ twinning in titanium have approximately equal CRSS levels at low to moderate temperatures [234]. However, it becomes increasingly difficult for $\{11\bar{2}2\}$ twins to nucleate at high temperatures, while the opposite is true for $\{10\bar{1}1\}$ twins. Thus, it is reasonable to use similar CRSS levels for basal slip and $\{10\bar{1}1\}$ twinning at high temperatures.

Due to the high volume fraction of the α phase, texture simulations did not include the deformation in the β phase. The efforts were firstly focused on simulating the texture evolution of rolled Ti64 at 800 °C to fine tune the CRSS values used and validating it with the existing literature [202]. From the aforementioned facts, the CRSS values used for the active slip systems in predicting the rolling texture evolution were taken as:

$$\tau_{\{prism\}} = 1.0;\ \tau_{\{basal\}} = 1.0;\ \tau_{\{pyr<a>\}} = 1.0;\ \tau_{\{pyr<c+a>\}} = 2.2$$

Initial texture was represented by an equally weighted and randomly oriented aggregate composed of 500 grains.

Predicted texture evolution during high temperature rolling to 1.2 equivalent strain (about the same strain level applied during single pass ECAE) is shown in Fig. 5.11(a). There is a good agreement between the prediction and the experimentally observed texture evolution reported in the literature [202]. Comparing the current predictions with the Dunst et al. [234] work utilizing the same modeling approach demonstrates that present study provides a better agreement with experimental observations, although the latter study included the simultaneous deformation of the β phase as well.
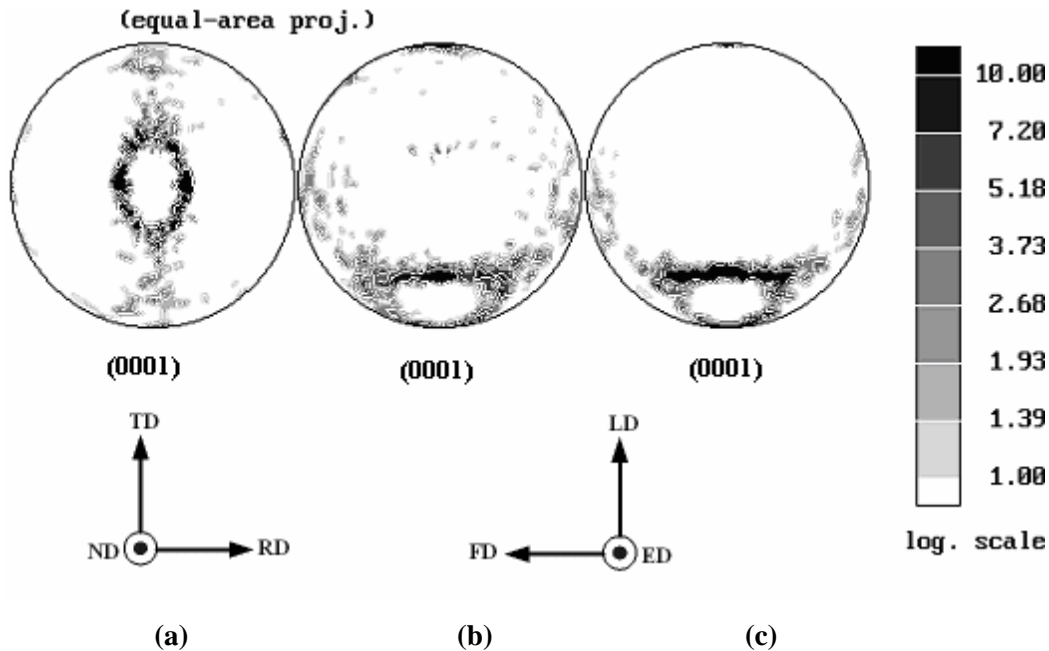
Fig. 5.11. Predicted (0001) pole figures of Ti64 after (a) rolling, (b) one pass ECAE excluding {10$\bar{1}$1} twinning, (c) one pass ECAE including {10$\bar{1}$1} twinning.

Rolling texture simulations also provided some insight for the effect of each slip system on texture evolution. It was found that each of prism, basal and pyramidal <c+a> slip systems produces (0001) components along the transverse, normal and rolling directions, respectively. On the other hand, pyramidal <a> slip aligns basal poles along the rolling and normal directions simultaneously.

Keeping all the simulation parameters (including the CRSS levels of the slip systems) the same and only changing the velocity gradient tensor to present the different stress state, texture evolution after one ECAE pass was predicted as in Fig. 5.11(b). Comparing this pole figure with the present experimental texture and that of the ECAE processed Ti [181] indicates that the consideration of only slip systems does not result in a very good agreement with the experimental texture. Therefore, the {10$\bar{1}$1} twinning system is included in the simulations since it is the only one observed in the deformed structure. The values of the constants A_1 and A_2 (Eq. (10) in Section 2.7.1) that adjust the twin reorientation were taken as 0.1 and 0.4, respectively. Fine tuning of the CRSS value

for $\{10\bar{1}1\}$ twinning with experimental measurements led to a value of 1.2 close to the CRSS used slip systems. Apparently, this attempt resulted in a better agreement, by removing the basal components around the extrusion and flow directions and increasing their intensity tilted towards the longitudinal direction as demonstrated in Fig. 5.11(c). It is worth mentioning that the ECAE texture simulations were able to capture the alignment of the basal planes with the long axes of the elongated grains during ECAE.
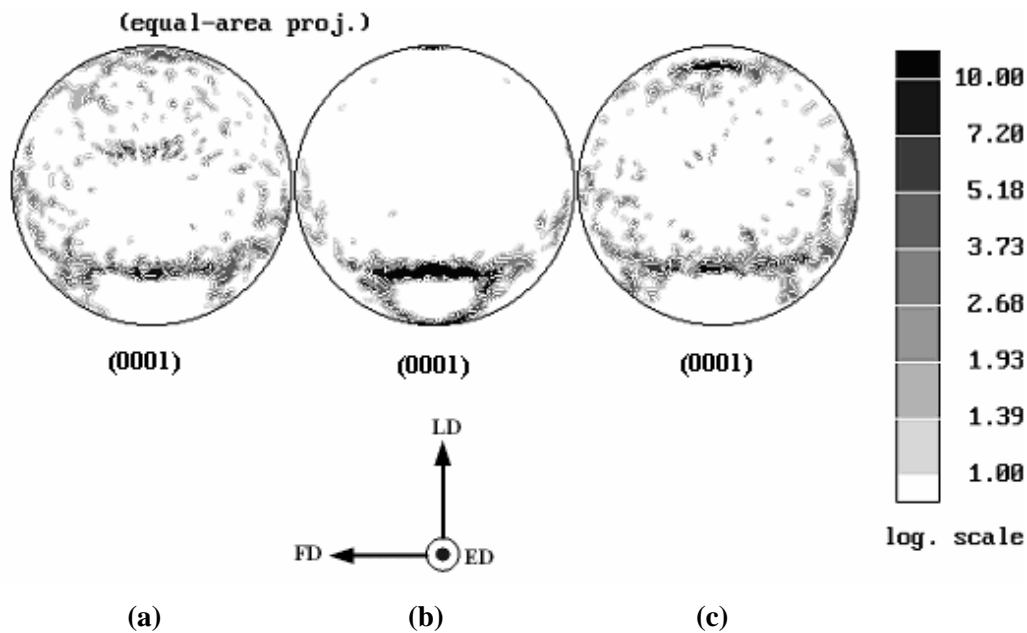
Fig. 5.12. Predicted (0001) pole figures of Ti64 after one pass ECAE with (a) $\{11\bar{2}2\}$ twinning, (b) $\{10\bar{1}2\}$ twinning, and (c) $\{11\bar{2}1\}$ twinning in addition to the slip systems.

As a comparison, the effect of different twinning systems on texture evolution during ECAE is presented in Fig. 5.12. CRSS values of the remaining twin systems are selected so as to match the twin volume fraction of the $\{10\bar{1}1\}$ system at the end of a single ECAE pass. This will demonstrate the effect of each twin system with the same twin density on texture evolution. It is seen that other than twinning on the $\{10\bar{1}2\}$ planes,

highlighted by Fig. 5.12(b), the remaining twin modes result in completely different texture developments. Similar texture evolution in the presence of $\{10\bar{1}2\}$ twins is expected because activity of $\{10\bar{1}1\}$ twins in compression rotates the crystal in the same way as $\{10\bar{1}2\}$ twins do in tension. However, $\{10\bar{1}1\}$ twins were the only ones observed during ECAE at 800°C probably because of the ECAE stress state and the differences in the CRSS of the twin modes.

To compare the relative importance of each deformation system on the resulting texture on a quantitative basis, the relative activity of each system was captured during the simulations. The relative activity of each deformation mode is defined as [166]:

$$RA_{sm} = \frac{\sum_r f^r \cdot \Delta\gamma^{r,sm}}{\sum_r f^r \sum_m \Delta\gamma^{r,m}} \qquad (14)$$

where the numerator indicates the total plastic shear contribution from a single slip or twinning mode (sm) and the denominator is the total plastic shear obtained from all the active modes (m). $\Delta\gamma$ is the individual shear of a deformation system. Shear strain on each crystal (r) is weighted by its volume fraction (f^r) to represent the contributions of the individual deformation systems over the whole aggregate. The contribution of the active deformation modes during rolling and ECAE in the absence of twinning is similar as seen in Figs. 5.13(a) and 5.13(b), respectively.

The texture of Ti64 during rolling is mainly developed by a combination of basal and pyramidal <a> slip systems, accounting for about 80% of the deformation at a strain of 1.2. Prismatic slip activity at the initial deformation stage in Fig. 5.13(a) is replaced by basal slip at higher strains. Similarly, pyramidal <a> and pyramidal <c+a> slip systems were found to be in competition. This is expected, since pyramidal <a> slip reduces the amount of pyramidal <c+a> slip required to accommodate deformation [1]. Pyramidal <c+a> activity increases at higher strains with a corresponding decrease in pyramidal <a> activity.
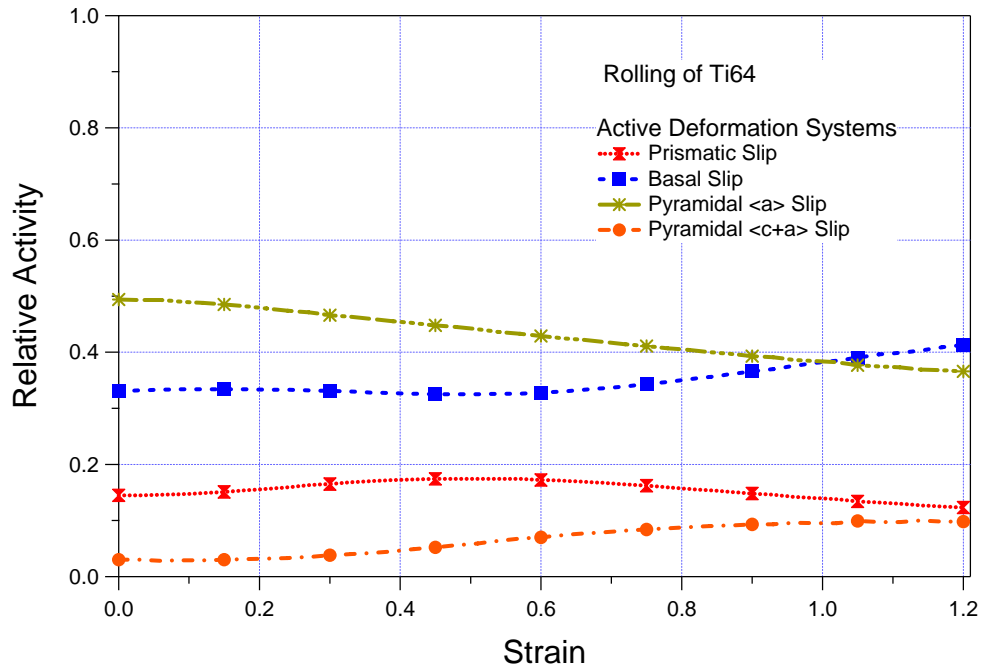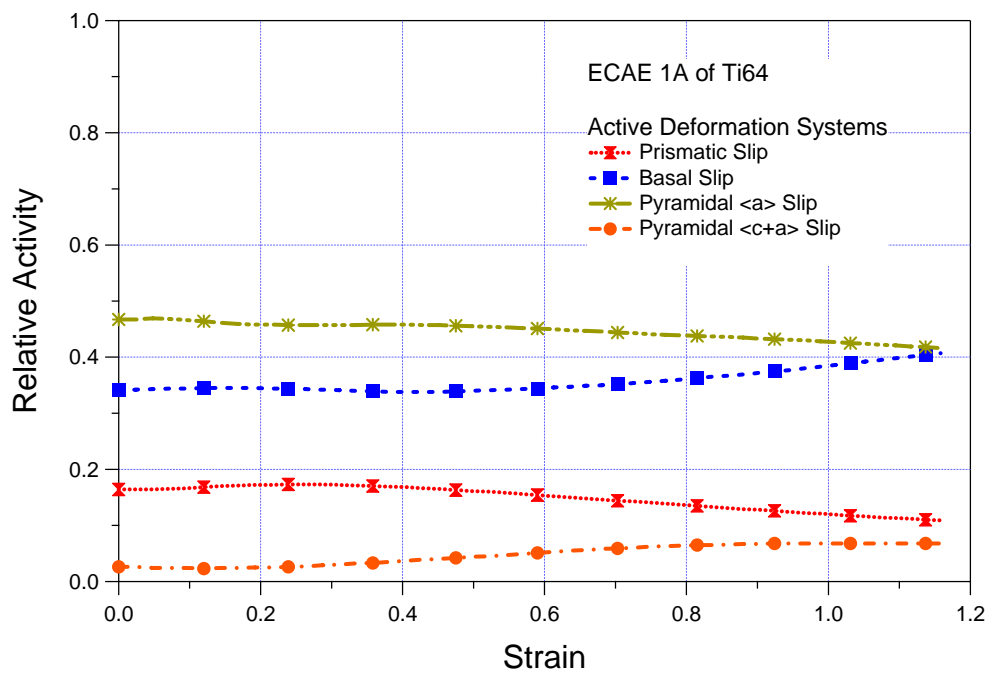
Fig. 5.13. Predicted relative activities of the slip modes during (a) rolling up to a strain of 1.2, and (b) single pass ECAE of Ti64.
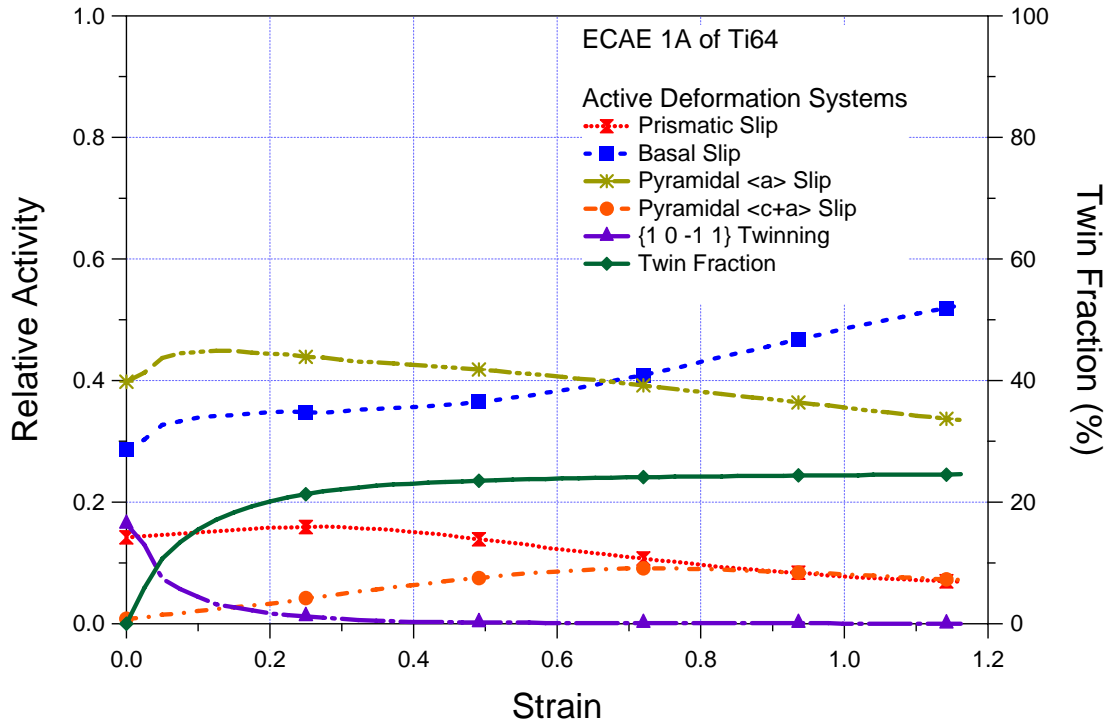
Fig. 5.14. Predicted relative activity of slip and twinning modes during single pass ECAE of Ti64.

When twinning is included in the ECAE simulations (Fig. 5.14), it is seen that the twin activity is observed only up to 0.4 strain. However, the considerable volume fraction associated with the present twin system is effective in shaping the final texture evolution. In the later stages of deformation, deformation along the c axis is accommodated by pyramidal <c+a> slip instead of twinning. Twin volume fraction after one ECAE pass is around 25% which is a slight overestimation when compared to the microstructural observations (Figs. 5.4 and 5.5). An interesting point is the continuous increase of the basal slip activity providing around 50% of the deformation after one ECAE pass when twinning is active. This increase results in the diminishing of both prism and pyramidal <a> slip activities. One reason for this might be that at each deformation step, the basal planes of more grains are gradually oriented parallel to the long axes of the elongated grains. This reasoning can be better visualized by Figs. 5.9(b) and 5.11(c). Thus, simple shear during ECAE will correspond to basal shears on the hcp crystals.

5.8. Conclusions

This chapter focused on the equal channel angular extrusion of Ti-6Al-4V alloy at a high temperature (800°C, ~ 0.55 T_m) and reported the microstructure and texture evolution during ECAE and post-ECAE room temperature mechanical behavior. Significant deformation twinning activity was observed at such a high deformation temperature. Possible reasons for high temperature twinning were discussed, emphasizing the effect of applied stress state on the separation of twin partials. The active deformation modes were discussed in the light of texture evolution during ECAE emphasizing the effect of individual deformation systems, including mechanical twinning, on texture evolution and resulting mechanical properties. Utilization of the VPSC crystal plasticity model led to successful predictions of the texture evolution during ECAE including the effect of mechanical twinning. The following conclusions were reached:

1. ECAE of Ti64 at 800°C, particularly the second pass following Route A, resulted in the $\{10\bar{1}1\}$ twinning as a major deformation mechanism. This is the first time where deformation twinning in Ti64 has been reported at such high temperatures and at low to moderate strain rates (1 s^{-1}). The resulting microstructure consisted of a fine network of nano twins.

2. Existence of high twinning activity at high temperatures was ascribed to the high stress levels achieved and moderate strain rate used during ECAE. It was argued that the high applied stress levels and the stress state during ECAE may lead to increase in the separation distance between the $\{10\bar{1}1\}$ twinning partials and the sessile stair rod dislocations creating a low effective SFE, and help nucleating twins.

3. High activity of basal and pyramidal <a> slip aided by the $\{10\bar{1}1\}$ mechanical twins during ECAE led to the texture evolution where the basal planes are almost aligned with the long axes of the elongated grains making an angle of 29° with the extrusion direction.

4. The consideration of the $\{10\bar{1}1\}$ deformation twin activity was necessary to correctly predict the experimental texture evolution during ECAE. Activity of the

$\{10\bar{1}1\}$ twins removes the basal components around the extrusion and flow directions and increase their intensity tilted towards the longitudinal direction.

5. Other than strengthening due to α plate and grain refinement, higher twinning activity in the ECAE 2A sample resulted in higher yield strength and work hardening rate compared to the as-received material in the post-processing room temperature monotonic experiments.

6. Observed directional tension-compression anisotropy in the ECAE 2A sample can not be attributed solely to the crystallographic texture evolved during ECAE, but it was claimed to be dependent on the tension-compression asymmetry of the critical shear stress levels of different slip modes and on the processing induced deformation structures.

5.9. Suggestions for Future Work

It was reported that crystallographic texture is not the sole reason for directional tension-compression anisotropy. A comprehensive understanding into the effect of processing induced microstructure on anisotropy would not be possible without an experimental approach probing the tensile and compressive stress strain response along multi directions. This approach combined with microstructural observations would allow correlating the flow response with slip/twin and dislocation substructure interactions. Such a study will also shed light on the existence of asymmetric CRSS values of deformation systems upon reverse loading.

The profuse high temperature twinning in ECAE 2A samples was surprising and a mechanistic explanation on its cause was suggested. One important question that needs an answer is the role of high temperature on the occurrence of this twin mode during ECAE. Detailed microstructural studies on lower temperature extruded billets is needed to investigate whether the $\{10\bar{1}1\}$ twins are still active or any alternative twin modes are activated at low processing temperatures. This will also strengthen the aforementioned argument regarding the effect of applied stress state and magnitude on twin nucleation.

One of the intriguing methods to consider for better understanding the observed the tension-compression anisotropy is to repeat both tests but terminate them at a given

strain. TEM observations on the strained tension and compression samples could be different especially in terms of their twin type and twin volume fraction. Since the type of twinning in hcp materials is directional dependent, activation of different twin modes during different stress states could lead to considerable anisotropy. A similar, but less tedious approach would involve the use of a miniature test frame in an SEM equipped with an EBSD system. This will allow the in-situ observation of active deformation mechanisms during mechanical testing.

Another future study could investigate improving the mechanical properties of ECAE processed Ti64 by going to higher number of passes. Although this is a challenging task considering the limited ductility of Ti64 which only allows processing at high temperatures, it is still viable with the use of isothermal ECAE dies. The profuse twinning with multiple twin variants in the 2A billet was remarkable. However, it is still questionable whether the twin fraction would continue to increase at higher number of ECAE passes. In such a case, twin boundaries might eventually act as grain boundaries refining the microstructure further and leading to even higher strength levels. Increase in ductility levels would also be expected due to improved strain hardening.

CHAPTER VI

EFFECT OF STRAIN PATH CHANGES ON THE MICROSTRUCTURE, TEXTURE AND FLOW BEHAVIOR OF UFG PURE ZIRCONIUM

6.1. Background

Zirconium (Zr) and its alloys are the main structural materials for applications in the nuclear industry due to their low neutron absorption coefficient preventing the negative effects of embrittlement. Also due to its high corrosion resistance, it finds applications in chemical plants. Pure Zr transforms from hcp α phase to bcc β phase at 850 °C. Similar to titanium, it has an axial (c/a) ratio lower than 1.633.

Owing to its technological importance, it is crucial to accurately assess the mechanical response after deformation processing. It is known that low symmetry metals such as Zr are anisotropic prior to processing and even small amounts of plastic deformation are sufficient to induce substantial anisotropy in these materials. The effects of conventional deformation techniques such as rolling on the mechanical response and flow anisotropy of Zr have been investigated [1, 146, 154, 194]. However, no attempt has been made so far regarding the mechanical properties and texture evolution of severely deformed Zr at ambient temperatures.

As mentioned earlier, crystallographic texture, microstructure evolution and post-processing mechanical response studies on ECAE materials have mainly focused on cubic systems, mainly because of insufficient ductility of hcp materials. Among the studies on ECAE of hcp materials, only few studies focused on Zr [184, 235, 236]. Cao et al. [235] demonstrated the microstructural evolution of Zr702 (commercial grade Zr with high wt% Hf impurity content) alloy up to 8 passes of ECAE following different processing routes at 350 °C. Other than the grain refinement down to sub-micron level, one of the main findings was the similarity of microstructural evolution to that of fcc materials processed using ECAE; namely, as commonly observed in fcc materials, formation of lamellar structures bounded by geometrically necessary boundaries (GNB). Additionally, improved tensile response along extrusion direction (ED) after ECAE was explained by the Hall-Petch relationship.

Choi et al. [235] performed room temperature ECAE of pure Zr, only by using a 135° die corner angle reducing the grain size from 200 μm to 0.4 μm. However they were not successful in processing at room temperature with a 90° die corner angle. They identified the activation of $\{10\bar{1}2\}$ tensile twins during the initial pass and $\{10\bar{1}1\}$ compressive twins after four passes of ECAE. Room temperature activation of the latter twin mode is interesting since $\{10\bar{1}1\}$ twins generally operate at higher temperatures in hcp materials [44]. It is important to note that the activation of the latter twin mode was not exhibited using microscopy techniques, instead was deduced from orientation relations on the basal pole figures.

Yu et al. [236] monitored the texture evolution of Zr702 up to four ECAE passes at 350 °C. Following a somewhat successful prediction of the texture evolution after one ECAE pass, they concluded that prismatic slip followed by basal and pyramidal <c+a> slip is responsible for the observed texture. Another work demonstrated the microstructural evolution of Zr702 at room temperature using a 135° die angle, up to four ECAE passes. Especially after the third ECAE pass, $\{11\bar{2}1\}$ compressive twins were abundant in the microstructure and were quoted as a main deformation mechanism [237]. The same authors showed that the twins disappeared completely after an annealing treatment of 10 min at 600 °C [237]..

ECAE has been the most used SPD method investigated for the grain refinement in zirconium and its alloys. Recently, the split Hopkinson bar technique was used to achieve ultra-fine grain size in Zr702 and similar microstructural features were found as compared to those observed after ECAE [238]. Considering the previous work conducted on ECAE of Zr, current work is the first time demonstration of room temperature processing using a 90° ECAE die corner angle. Room temperature processing is crucial in retaining the refined microstructure and ECAE texture throughout the processing by minimizing the possible recovery-recrystallization mechanisms and magnifying their effects on the post-ECAE mechanical response. The room temperature processing of Zr through a 90° corner angle was partly achieved using the sliding walls concept in the present ECAE die that helps reducing the die frictional effects [185].

Additionally, none of the above studies shed light on the post-ECAE mechanical anisotropy. This phenomenon was investigated for Ti and Ti64 in the previous chapters. Agnew et al.[183] investigated the tensile response of ECAE processed magnesium alloy AZ31B on two perpendicular material planes and along three directions. The significant plastic anisotropy was rationalized in terms of the strong ECAE texture.

There have also been quite a few works on modeling the texture evolution and mechanical response of Zr. These studies concentrated on predicting the flow behavior and texture evolution of Zr and its alloys under various stress states and deformation temperatures. Modeling the material behavior of Zr is challenging due to the activity of multiple deformation systems and the need to describe their interactions realistically in constitutive models for accurate prediction of the hardening response and the resulting texture evolution. Tome et al. [239] achieved this task by reproducing the tensile and compressive response of clock-rolled pure Zr along different directions up to 30% strain at both liquid nitrogen and room temperature where they used a latent hardening scheme implemented in a VPSC code. This approach was also extended by Kaschner et al. [240] to model the texture evolution and flow response of pure Zr subjected to temperature reloads. A VPSC code was also put in use by Castelnau et al. [241] and Sanchez et al. [153] to simulate the texture evolution of Zr 702 alloy under channel die compression at room temperature and zircaloy subjected to torsion at 750 °C, respectively. A couple of attempts used a Taylor type approach to capture the texture evolutions during cold rolling of pure Zr [194] and high strain compression of Zr-2.5Nb [242] at elevated temperatures. All of these modeling works were effective in complementing the experimental findings for a better understanding of the complex deformation behavior of Zr and its alloys. Apparently, a suitable modeling approach is required for the case of severely deformed Zr as well where a highly anisotropic flow behavior is expected.

In this chapter, microstructural development, texture evolution and post-processing mechanical behavior of high purity zirconium (Zr) are investigated during single pass ECAE at room temperature. Examining these properties in yet another hcp material will provide a venue for observing the common trends and apparent contrasts in the material behavior of hcp materials subjected ECAE. The present study also aims at providing a comprehensive understanding into the effect of ECAE texture on the post-

processing plastic anisotropy of pure Zr by identifying the underlying deformation mechanisms. For this purpose, room temperature ECAE processed Zr with two initial textures were compressed up to high plastic strains in three orthogonal directions of the processed billet. The observed flow anisotropy after ECAE is correlated with the induced crystallographic texture and the underlying deformation mechanisms were revealed employing the VPSC polycrystal plasticity model. A single set of hardening parameters is used to predict the texture evolution and flow response after the strain path changes achieved by ECAE and post-ECAE compression experiments.

6.2. ECAE Processing of Pure Zr

The initial material was processed from a high-purity crystal bar (composition wt ppm: 35 Hf, 50 Fe, 20 Al, 50 V, 50 O, 20 N, 22 C) that is sufficiently low in interstitial impurities such that twinning is quite active. The mechanical processing included knockdown forging followed by several passes through a rolling mill such that the final product was a clock-rolled plate. After clock-rolling the plate is annealed at 550 °C for 1 hr resulting in an average grain size of 25 μm as seen in Fig. 6.1. The texture of the initial material can be described as a strong c-axis (basal poles) fiber in the plate normal direction. Prior to extrusion, Zr bars with a cross section of 8×8 mm cut from the clock-rolled and annealed plate were inserted into 25.4×25.4 mm cross section nickel cans and extruded for a single pass at room temperature. Nickel was chosen specifically as the can material due to its similar strength with Zr and favorable room temperature extrusion properties.

ECAE was conducted at an extrusion rate of 0.03 mm/sec corresponding to an approximate strain rate of 10^{-3} s^{-1}, using a 90° corner angle ECAE die. This strain rate was selected to match with the strain rate employed in the post-ECAE compression experiments. Two single pass extrusions were performed with different initial billet orientations to demonstrate the effect of initial texture on ECAE texture evolution, and post-processing mechanical response. In the first extrusion, the billet is aligned such that the basal poles are along the extrusion direction of the die coordinate system. In the second extrusion, the billet is aligned such that the basal poles are along the flow

direction of the die coordinate system. The orientations of the billets with respect to the die coordinate system are presented in Fig. 6.2.
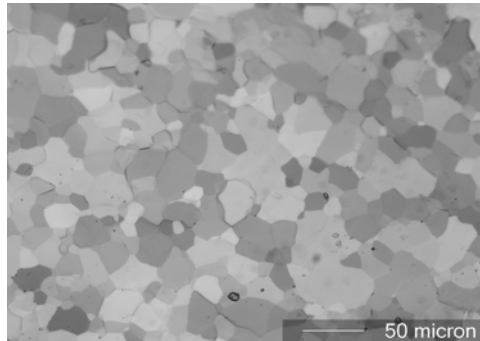
Fig. 6.1. Optical microscopy image showing the as-received microstructure of clock-rolled and annealed pure Zr.

(a)   (b)
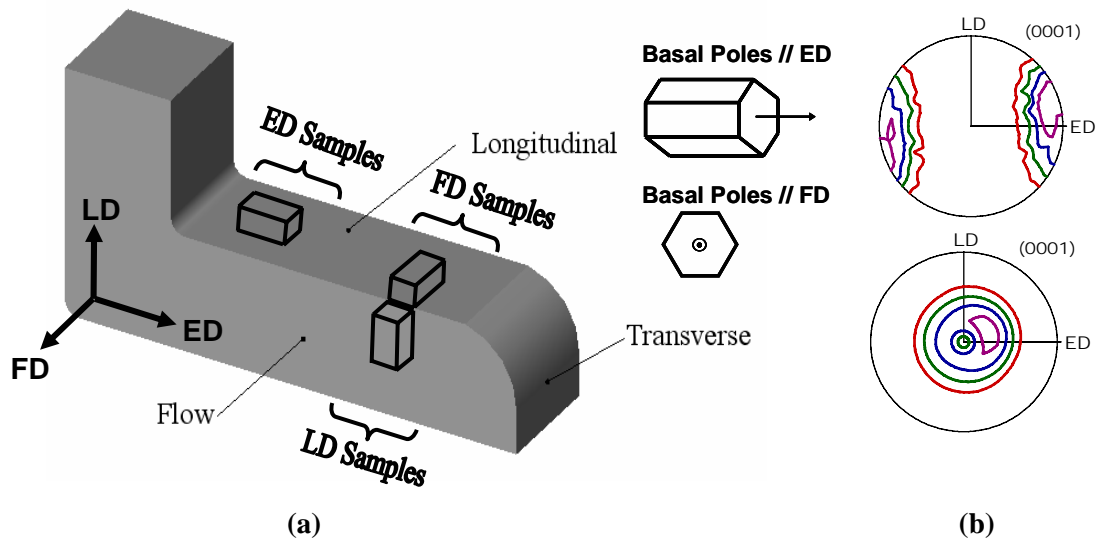
Fig. 6.2. (a) Zr billet representation during ECAE processing and orientation of mechanical test samples on the as-processed billet. ED, LD and FD denote the extrusion, longitudinal and flow directions, respectively. (b) Initial textures with respect to the die coordinate system: basal poles parallel to ED (top) and basal poles parallel to FD (bottom).

Room temperature monotonic stress-strain response of the ECAE processed Zr was investigated through compressive loading at a strain rate of 10^{-3} s^{-1}. Plastic strains up to 30% were employed by interrupting each test and unloading-reloading at 10% intervals. Three batches were prepared with each containing samples having their compression axes parallel to one of the three orthogonal directions (extrusion, longitudinal, flow) of the extruded billet (Fig. 6.2(a)). In selected compression experiments, deformation was tracked using a digital image correlation (DIC) as described in Section 3.4.

6.3. Microstructural Evolution

6.3.1. Extrusion Case I: Basal Poles along Extrusion Direction

TEM observations shown in Fig. 6.3(a) reveal that ECAE led to considerable grain refinement with an average grain size of 400 nm. In some areas, well defined dislocation bands containing cells with low misorientation boundaries are found. At room temperature Zr experiences $\{10\bar{1}2\}$ tensile twinning. However high strain and stress levels applied during ECAE might have activated additional twin systems to accommodate the deformation, as mentioned earlier in Ti64 for $\{10\bar{1}1\}$ twinning. Feasibility and likelihood activation of additional twin systems will be elaborated in detail with the help of texture measurements, post-processing mechanical testing results and VPSC simulations.

OIM studies on the as-processed Zr were unsuccessful due to the severe lattice distortions introduced by the high dislocation density. Therefore, as-processed Zr was annealed at 400 °C for one hour, to remove the excessive dislocations but preserve the processing texture. Fig. 6.4(a) demonstrates the microstructural evolution on the flow plane of the annealed sample in the form of an inverse pole figure map. Recovery and grain growth are apparent microstructural mechanisms and equiaxed grain morphology is observed. Some areas demonstrate excessive grain growth.
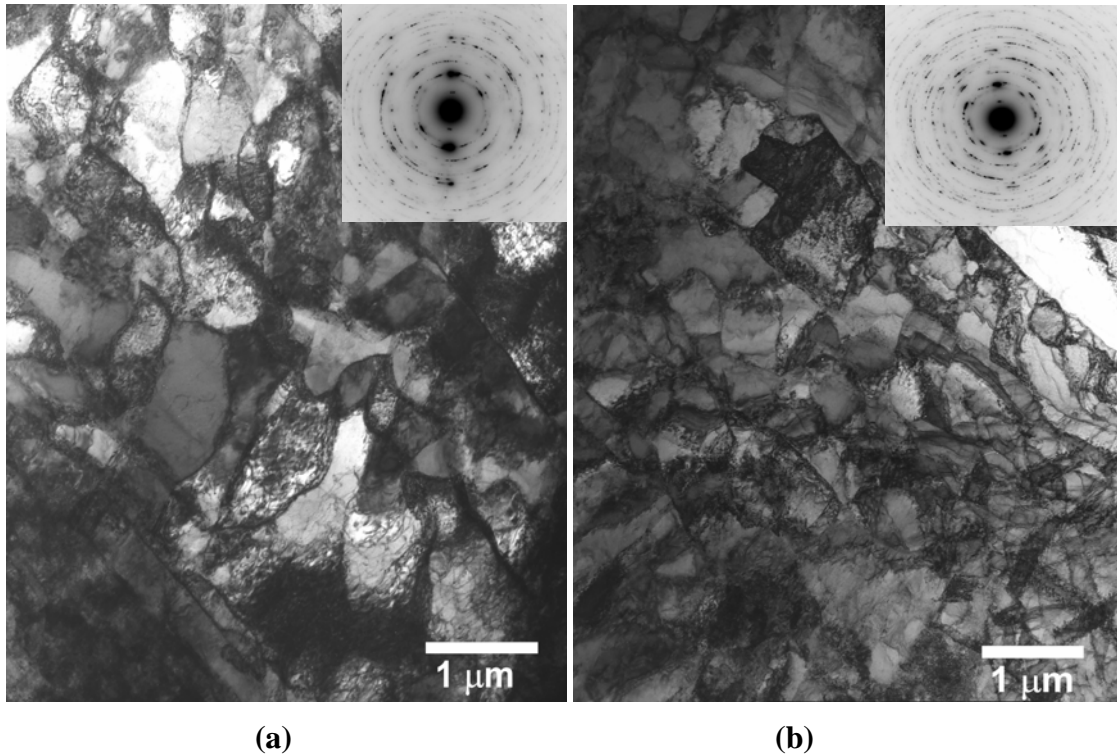
Fig. 6.3. Bright-field TEM image of pure Zr after single ECAE pass at room temperature, (a) initial basal poles oriented along ED, (b) initial basal poles oriented along FD.

6.3.2. Extrusion Case II: Basal Poles along Flow Direction

ECAE of this orientation resulted in similar microstructural features with the previous case. Grain size refinement was down to sub-micron range with an average grain size of 450 nm as seen in Fig. 6.3(b). As in the previous case this sample was also annealed at 400 °C for one hour for OIM investigation. Fig. 6.5(a) exhibits significant recovery and grain growth in the microstructure. However, there is a notable difference in the grain morphology as compared to the first extrusion case. Namely, the inverse pole figure map reveals many elongated grains as opposed to the equiaxed structures observed in the previous case.

(a)　　　　　　　　　(b)
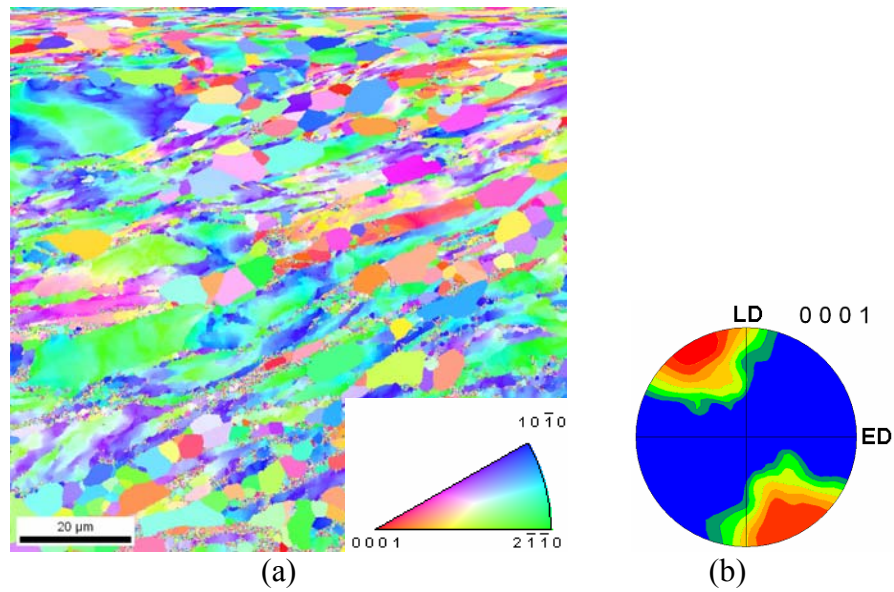
Fig. 6.4. (a) Inverse pole figure map, (b) pole figure of Zr after a single ECAE pass at room temperature followed by annealing at 400 °C for one hour. Extrusion case I.

(a)　　　　　　　　　(b)
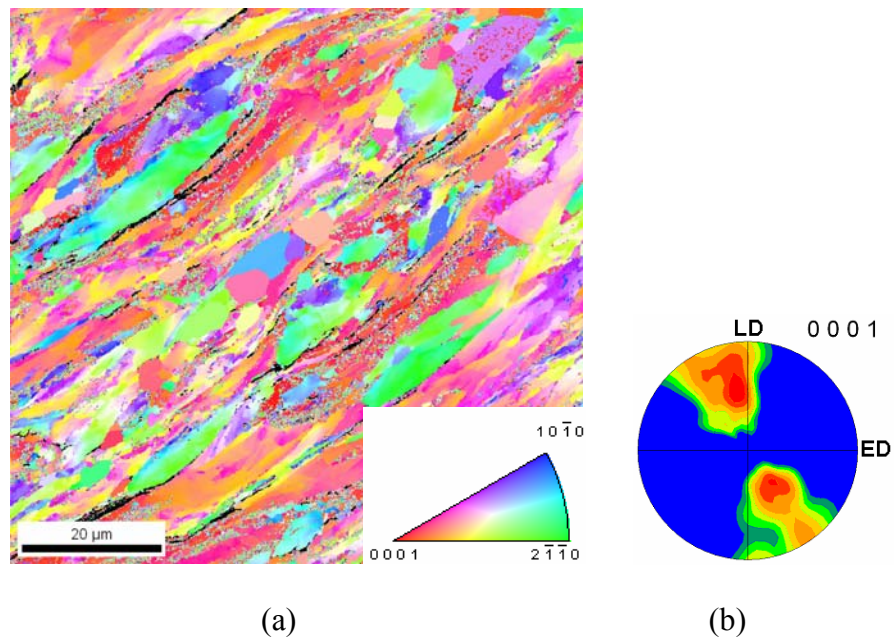
Fig. 6.5. (a) Inverse pole figure map, (b) pole figure of Zr after a single ECAE pass at room temperature followed by annealing at 400 °C for one hour. Extrusion case II.

6.4. Texture Evolution

6.4.1. Extrusion Case I: Basal Poles along Extrusion Direction

Fig. 6.6(a) shows the texture evolution after a single ECAE pass at room temperature. It is seen that the basal poles which are initially aligned with ED rotate counter clockwise. Eventually, they are tilted about 25° from the LD. A similar type of texture evolution was shown in ECAE processing of several hcp materials, including the Ti64 extrusions in this study, where the basal planes are almost aligned with the long axis of the elongated grains [183, 236, 243, 244]. As mentioned earlier for Ti64, The long axes of the elongated grains represent the inclination of a distorted ellipsoidal grain with respect to the extrusion direction. This texture evolution does not change significantly upon annealing at 400 °C for one hour, as evidenced in Fig. 6.4(b).

(a) (b)

(c) (d)

Fig. 6.6. Crystallographic texture evolution during extrusion case I. (a) After single pass ECAE. (b) Post-ECAE compression along ED to 30% strain. (c) Post-ECAE compression along LD to 30% strain. (d) Post-ECAE compression along FD to 30% strain.

During post-ECAE compression experiments, textures develop differently as a function of the loading axis as illustrated in Figs 6.6(b) to 6.6(d). The rotation of basal poles around FD continues in the counter clockwise direction during subsequent compression along ED. The strength of the maximum peak decreases and a weak component appears near ED. Compression along LD leads to a similar texture evolution as that for the ED sample. There is a counter clockwise rotation around FD and the texture gets more diffuse. For the FD samples, the texture evolution is quite different than the other two sample orientations (ED and LD). Basal poles tend to align themselves with the compression axis (FD).

6.4.2. Extrusion Case II: Basal Poles along Flow Direction

When the basal poles were initially aligned with FD, ECAE displaces a majority of them towards the perimeter of the pole figure tilted about 25° from the LD as seen in Fig. 6.7(a). Other than the fact that, a small portion of basal poles remains spread around FD, this texture evolution is similar to the one that is seen for the previous extrusion case, except a higher concentration of basal poles around FD. With very different starting textures, both Zr billets demonstrate similar texture evolution after ECAE. This might be attributed to the high level of applied strain via the simple shear strain state of ECAE, dictating the texture evolution regardless of the initial texture. As in the previous extrusion case, annealing at 400 °C for one hour did not make much effect on the texture evolved after ECAE. However, an apparent reduction of the basal poles around FD is seen in Fig. 6.5(b).

Different crystallographic texture evolutions detected depending on the direction of applied compressive strain as exhibited in Figs. 6.7(b) to 6.7(d). Post-ECAE compression along ED results in a further counter clockwise rotation of the basal poles around FD and movement f the basal poles towards the rim of the pole figure. In addition, weak components along ED are created. Texture evolution during the compression of LD sample can be described by the movement of basal poles from the center to rim of the pole figure; this change is accompanied by slight rotation of the poles around FD in counter clockwise direction. Finally, compression along FD results in a movement of the basal poles from the rim to the center of the pole figure to align them with compression

axis. The basal poles are spread 10°-15° around FD. The texture evolutions during post-ECAE compressions along ED and LD in both extrusion cases reveal similar features. This is expected since the as-ECAE processed textures are similar as well. Only, FD compressions exhibit considerably different texture evolutions due to the different basal pole concentrations in their initial textures.
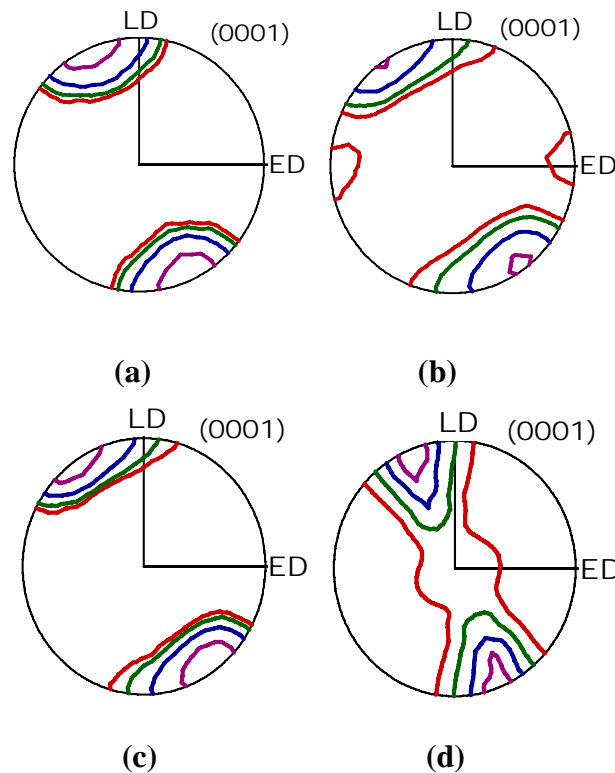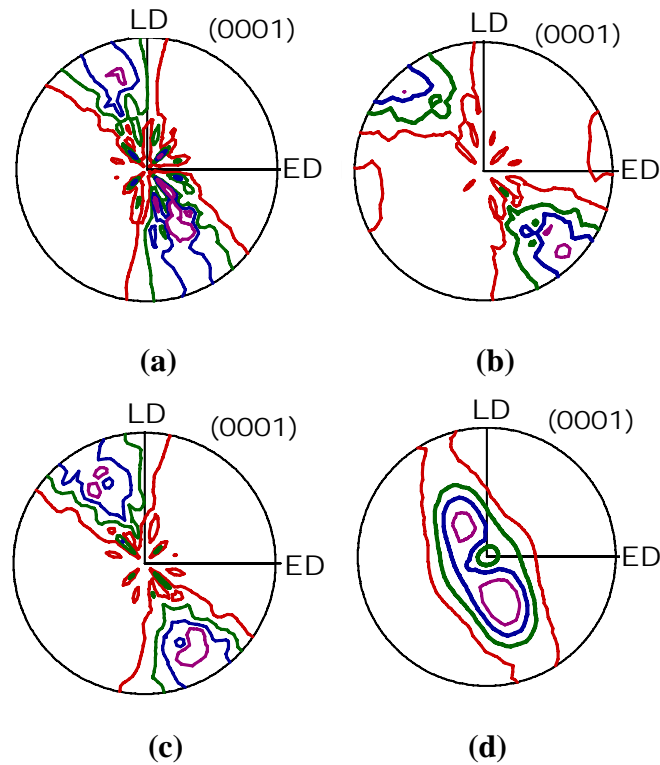

Fig. 6.7. Crystallographic texture evolution during extrusion case II. (a) After single pass ECAE. (b) Post-ECAE compression along ED to 30% strain. (c) Post-ECAE compression along LD to 30% strain. (d) Post-ECAE compression along FD to 30% strain.

6.5. Mechanical Behavior

The as-received pure Zr used in this study has a similar composition and processing history with the one used in [240]. The as-received compressive response is demonstrated in Fig. 6.8 as reproduced from the data in [240]. Apparent plastic flow anisotropy is evident and explained by the relative activity of various slip and twin modes

depending on the compressive loading direction. During compression through the thickness of the plate, the basal poles are aligned parallel to loading direction. This leads to the activation of pyramidal <c+a> slip having a relatively higher CRSS which in turn results in a high yield strength. In contrast, compression in the plane of the plate aligns the basal poles perpendicular to the loading direction. This results in deformation via easy prismatic slip, and the material exhibits a lower yield strength. The high hardening rate above 10% strain was explained due to the activation of $\{10\bar{1}2\}$ tensile twins. This twinning mode was activated due to the tensile strain along the basal poles that is induced by the applied compressive strain.
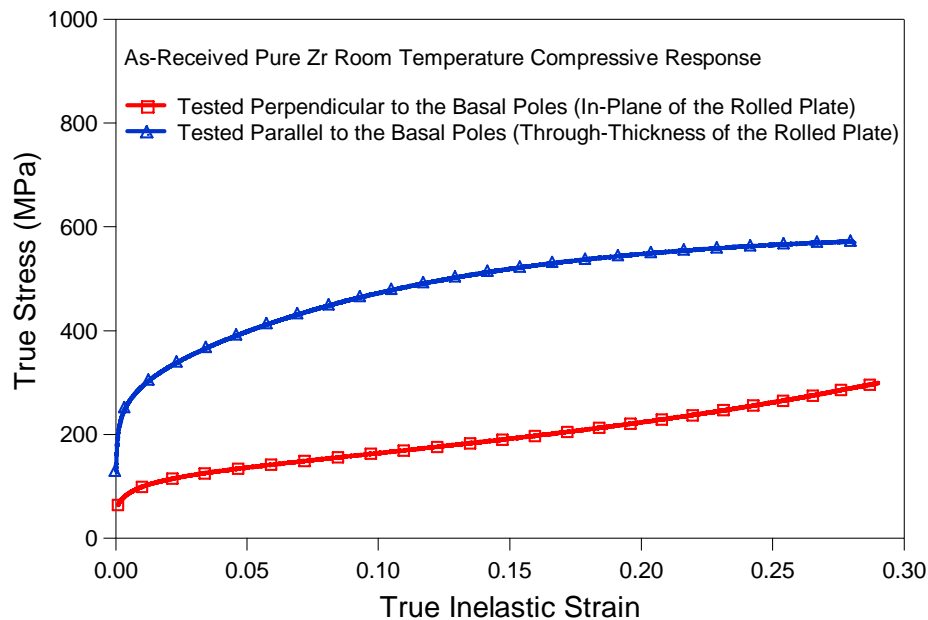
Fig. 6.8. Uniaxial room temperature compressive response of the as-received pure Zr plate along two perpendicular directions

6.5.1. Extrusion Case I: Basal Poles along Extrusion Direction

Fig. 6.9 shows the compressive response of the single pass ECAE processed Zr along three orthogonal directions. Owing to grain refinement via ECAE, higher yield strengths in all three orientations as compared to the as-received response are clearly

seen. It is seen that a considerable plastic anisotropy is present. Particularly, compression along LD results in the highest yield strength whereas along ED and FD have similar yield strengths. Considering the strain hardening behaviors, compression along FD hardens at a higher rate than that along ED after the first 10% plastic strain. LD sample strain hardens at a higher rate as compared to the other two orientations starting from the first few percents of plastic strain. However, this sample softens above 10% plastic strain. Experimental points obtained from cross-sectional measurements of the sample after each 10% strain interval verify the accuracy of the true stress - true strain relation used to obtain the flow curve of the LD sample. These points are shown in Fig. 6.9. The procedure followed to obtain these points is as follows: after each 10% strain increment, the instantaneous force is divided by the instantaneous sample cross-sectional area normal to the loading axis measured after unloading.

Fig. 6.9. Uniaxial compressive response of the as ECAE processed Zr along three orthogonal directions up to 30% plastic strain for the extrusion case I.

The striking behavior of abnormal softening after 10% strain during compression of LD needs more attention. The softening behavior repeated itself in multiple LD compression samples and therefore cannot be attributed to a possible experimental error. Moreover, all samples from different orientations were tested using the same experimental setup. The reason behind this abnormal softening was investigated in more detail using speckle analysis with a DIC system.

It was found that the softening behavior during axial compression is due to a complex strain state induced by the strong texture in the material. As seen in Fig. 6.10, the deformed grids provide proof that in addition to the applied compressive axial strain, a certain amount of shear takes place. This deformation behavior can be explained considering the orientation relation between the strong texture in the material and the loading axis. The texture in the LD sample during loading is such that the basal poles are tilted 25° from the loading axis. During compression, the sample prefers to slip at this particular material plane, however is prohibited due to the constraint from the compression platens. This results in the formation of an inhomogeneous strain field as will be discussed in further detail in Section 6.6.
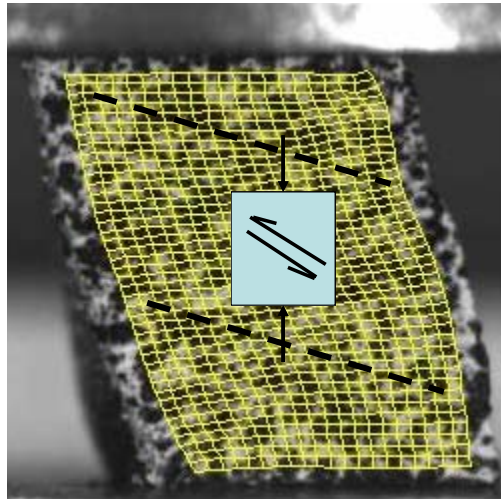
Fig. 6.10. Inhomogeneous strain field present during LD compression detected with the help of the deformed grids obtained via the DIC technique.

6.5.2. Extrusion Case II: Basal Poles along Flow Direction

Room temperature compression experiments demonstrated improved yield strengths in pure Zr after ECAE. Compression along three orthogonal directions up to 30% plastic strain reveals an anisotropic behavior as in the previous extrusion case, however, the order of strength levels are different in this case (Fig. 6.11). Namely, compression along LD and FD give similar yield strength levels whereas the sample along ED is softer than both. As in the previous extrusion case, ED response exhibits a steady and low hardening rate. The LD and FD responses are similar and indeed, they follow the same response until about 5% strain. Above 5% strain, the FD sample hardens at a much higher rate than that of LD sample.
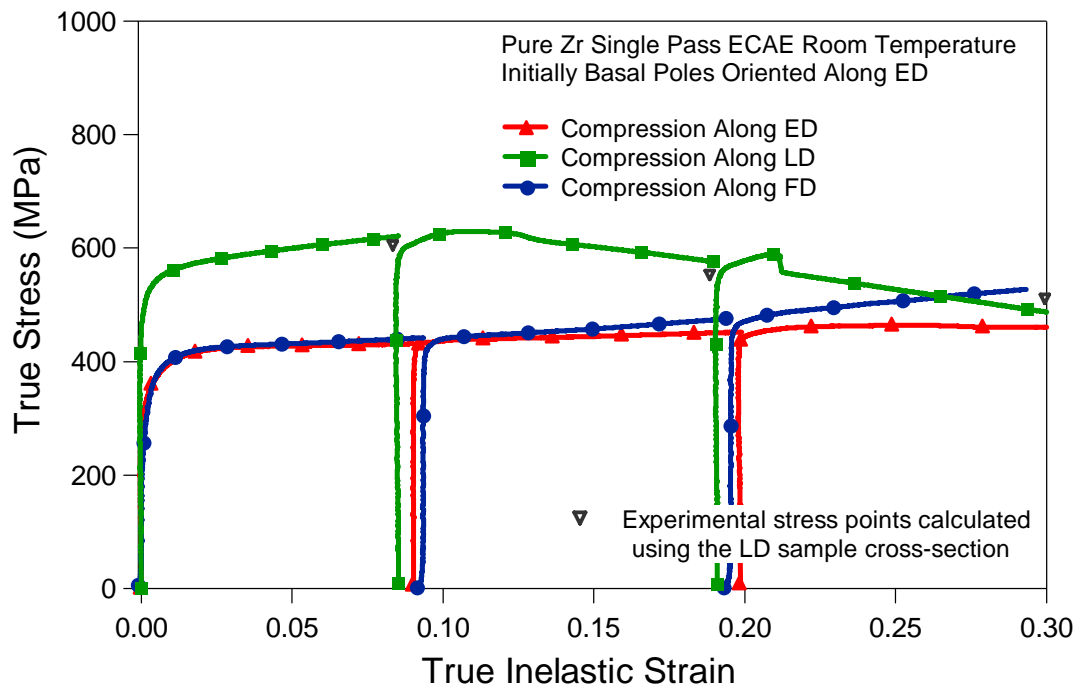

Fig. 6.11. Uniaxial compressive response of the as ECAE processed Zr along three orthogonal directions up to 30% plastic strain for the extrusion case II.

The LD sample repeats the abnormal softening behavior for this extrusion case as well. The experimental points obtained from dividing the instantaneous force by the

instantaneous sample cross-sectional area are also exhibited. Since the textures of the two extrusion cases are not far apart, one can more confidently argue the strong influence of the inter-relation between the orientation of basal poles and loading axis on the softening behavior.

The contrast in flow behavior trends of the two extrusion cases is attributed to their different textures evolutions after ECAE. A high concentration of basal poles around FD and LD results in a high yield strength coupled with a high hardening rate during FD and LD compression of the second extrusion. In the first extrusion, only the LD sample has a high concentration of its basal poles aligned with the loading axis and therefore it exhibits a high yield strength and strain hardening rate as compared to the other two sample orientations (ED and FD).

6.6. Discussion of the Results

The experimental texture evolutions and stress-strain responses of ECAE processed Zr are predicted employing the VPSC crystal plasticity model in combination with the predominant twin reorientation scheme. As a result, active deformation mechanisms governing the ECAE of pure Zr and their influence on texture evolution and post-ECAE flow response are determined. The first input for VPSC calculations is the initial texture. The measured crystallographic textures for the two starting orientations are represented by 1944 spherical grains with individual weight fractions. The two initial Zr billet textures were previously presented in with respect to the ECAE die coordinate frame in Fig. 6.2(b). Another major input to the simulations is the active deformation mechanisms, their respective Voce hardening parameters and the latent hardening coefficients coupling them.

At room temperature, the easy slip system in Zr is prismatic slip that takes place on the $\{10\bar{1}0\}$ planes and along the $<10\bar{1}2>$ directions. However, this slip system can only accommodate shears along the $<a>$ directions [123, 193]. The two deformation mechanisms that can accommodate shears along the $<c>$ direction, meaning an extension or contraction along the $<c>$ axes of the hcp crystal, are pyramidal $<c+a>$ slip and deformation twinning. The former generally takes place at comparably elevated temperatures, whereas the latter is commonly observed at lower temperatures, high strain

rates and in coarse-grained materials [1, 123]. The specific deformation twinning system activated depends on the sense of shear (tension or compression along basal poles), the c/a ratio of the hcp crystal and the temperature of deformation [122, 137]. Recent works on clock-rolled Zr showed that at room temperature, the main deformation twinning mode was $\{10\bar{1}2\}$ tensile twinning [239, 245]. This was observed during compression of the clock-rolled Zr plate during in-plane compression, which positions the basal poles perpendicular to the compression axis. In the same studies, the main slip mechanisms were identified as prismatic <a> and pyramidal <c+a> [239, 245]. The current simulations will rely on these observations and allow the activation of these three systems during ECAE and post-ECAE compression experiments.

Table 6.1

Voce hardening and latent hardening parameters used in the VPSC simulations for predicting the texture evolution of and mechanical response of ECAE processed pure Zr.

Deformation System	τ_0 (MPa)	τ_1 (MPa)	Θ_0 (MPa)	Θ_1 (MPa)	$h^{s,prism}$	$h^{s,basal}$	$h^{s,pyr}$	$h^{s,twin}$
Prismatic Slip	22	50	560	15	1	1	1	6
Basal Slip	190	22	21	10	1	1	1	3
Pyramidal <c+a> Slip	105	115	400	78	1	1	1	6
Tensile Twinning	100	120	100	50	1	1	2	10

Additionally, basal slip is included as a third active slip mode in the simulations. Although basal slip is not commonly observed during room temperature deformation of pure Zr [108, 246, 247], the rationale to consider it operative stems from two main reasons. Firstly, as will be seen in the following sections, the simulations showed that basal slip was a necessary shear accommodating mechanism for accurate predictions of

the ECAE texture. Secondly, there have been few studies reporting the activation of basal slip in Zr during room temperature deformation [248, 249]. Possible reasons for the activation of basal slip at ambient temperature will be discussed in more detail in Section 6.6.3. The Voce and latent hardening parameters in [239, 240] were selected as a start point in the simulations and were adjusted slightly so as to match the texture evolution and stress-strain response of the ECAE processed Zr. Table 6.1 lists the parameters utilized in the present model. These parameters are qualitatively similar to the ones reported in [239, 240]. The small differences are attributed to the slight variations in the composition and the clock rolling of the as-received Zr material.

As in the experiments, the strain rate used throughout the simulation was 10^{-3} s^{-1}. In simulating the ECAE process, the deformation state was described as simple shearing along the intersection plane at 45º [68]. The velocity gradient for this deformation in the fixed die coordinate system (ED-LD-FD) is given in [216], where Φ is half of the die angle.

$$L = \dot{\varepsilon} \begin{bmatrix} \sin\Phi & \cos\Phi - 1 & 0 \\ \cos\Phi + 1 & -\sin\Phi & 0 \\ 0 & 0 & 0 \end{bmatrix} = \begin{bmatrix} 0.001 & -0.001 & 0 \\ 0.001 & -0.001 & 0 \\ 0 & 0 & 0 \end{bmatrix} \quad (15)$$

It should be noted that during the simulations, ECAE simple shear is preceded by a 10% compressive strain. This is owing to the fact that the Zr billets are jacketed in nickel cans. From the dimensional measurements on the extruded Zr and the nickel can, it was found that the Zr billets fill up the small clearance between the billets and the jacket inner-wall. To account for this observation in a simple way, a 10% compressive strain is applied in the LD, which is followed by a 100% simple shear strain. The velocity gradient for the subsequent axial compressive tests along three orthogonal directions considered strain control in the direction of straining and assumed traction-free surfaces in the other two directions.

6.6.1. Prediction of the Extrusion Case I

Predictions of the texture evolution and mechanical behavior after ECAE are conducted using VPSC and are presented in Fig. 6.12. Figs. 6.12(a) to 6.12(c) show the simulated ECAE texture of Zr, where the positive effect of including basal slip is clearly

displayed with a reasonable texture prediction in Fig. 6.12(c). Significant basal slip is unexpected for Zr, but as shown in Fig. 6.12(a), suppressing basal slip leads to an inaccurate texture prediction.
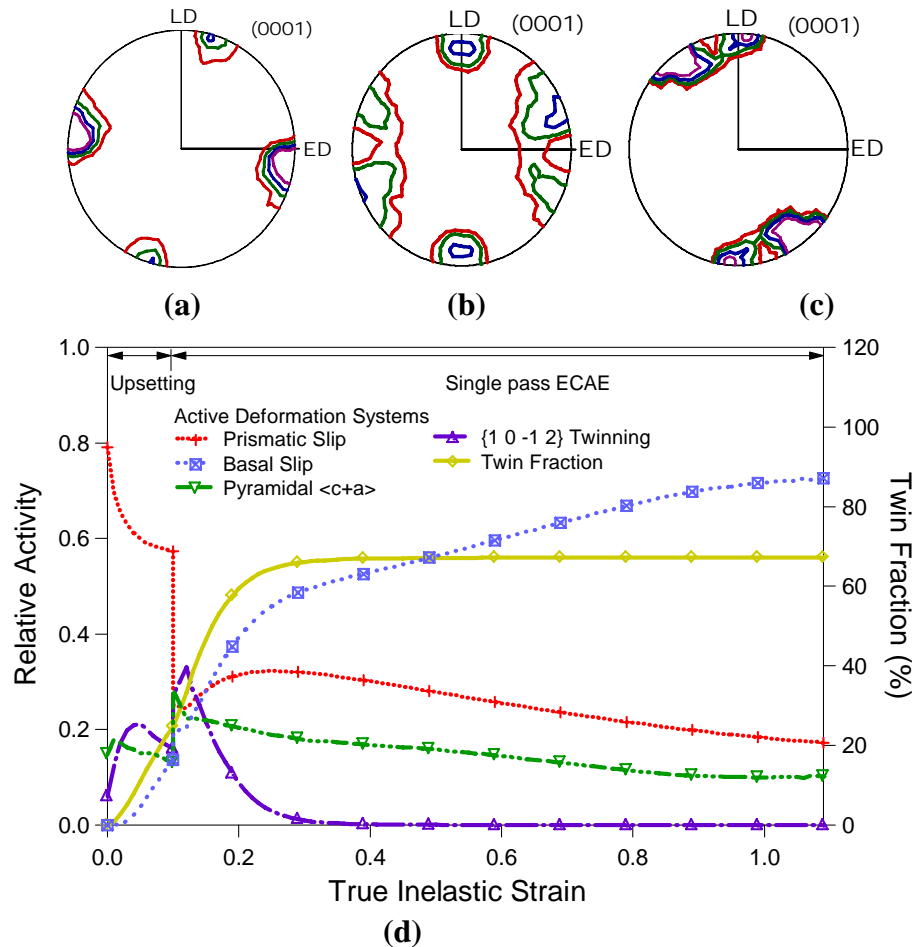
Fig. 6.12. Predicted texture evolution of Zr during single ECAE pass; (a) without basal slip, (b) after initial upsetting, (c) with basal slip and initial upsetting. (d) Predicted relative activity of the operative deformation mechanisms during the extrusion case I.

As seen in Fig. 6.12(d), basal slip is the most active deformation mechanism with reaching to almost 70% of the total activity. The prismatic slip activity decreases steadily down to 20% of the total activity. Pyramidal <c+a> slip and $\{10\bar{1}2\}$ twinning mostly operate during the initial 10% compressive strain, where the billet in the die upsets. This

is because during die upsetting along LD, both ED and FD experience tensile strains. The change in the texture after upsetting is shown in Fig. 6.12(b). After the initial upset, pyramidal <c+a> slip decays following a similar pattern as that of prismatic slip and making up 10% of the total activity at the end of a single ECAE pass.

The twin volume fraction after a single ECAE pass is predicted as 70%. This could be regarded as a considerably higher level than expected due to the fact that twinning is suppressed with decreasing grain size which certainly takes place during ECAE. The assumption of 10% initial upset during ECAE could be an overshoot and might be responsible for the high twin volume, since the majority of twinning activity takes place during the initial upsetting of the billet as observed in Fig. 6.12(d).

Regarding the post-ECAE mechanical response and texture evolution, the predictions demonstrate a very well agreement with the experimental results. In simulating the compression response along ED, the yield strength level and the low steady hardening level is successfully captured as seen in Fig. 6.13(a). The texture evolution in which the basal poles are further rotated counter clockwise around FD is also predicted. Nevertheless, the low intensity basal poles around ED are not reproduced in the texture prediction as observed in Fig. 6.13(c). The active deformation mechanisms resulting in the observed texture evolution and mechanical response are prismatic slip and basal slip, with increasing activity of basal slip with applied compressive strain.

The yield strength levels and the hardening rates are also well predicted during the compression along FD as seen in Fig. 6.14(a). Considering the texture evolution, the two major positions of basal poles, which are tilted from LD and concentrated around FD with 5°-10° spread, are successfully reproduced in Fig. 6.14(c). The appearance of basal poles along FD is expected since during compression along FD, basal poles tend to rotate towards the loading axis. During FD compression, tensile strains will be induced along basal poles around LD. These tensile strains will activate the $\{10\bar{1}2\}$ tensile twins. Actually, this is confirmed by the predictions on the relative activity of deformation systems where apparent twinning activity is seen.

The two major active slip systems are prismatic and basal, with the latter increasing with applied compressive strain. Also after about 10% strain, pyramidal <c+a> slip is activated. Pyramidal <c+a> is mainly needed to accommodate the strain along the

<c> axes of the orientations around FD, which were previously formed by tensile twinning in the first 10% compressive loading. High twinning and pyramidal <c+a> slip activity explains the higher hardening rate observed during compression of this sample above 10% strain as compared to that of the ED sample. Twin boundaries can act like grain boundaries and increase the hardening rate by preventing the passage of slip dislocations [137, 187]. In the model, this effect is represented by latent hardening parameters linking these two deformation modes, which is found to be high compared to those between slip modes (Table 6.1). The measurements show a higher hardening rate after 25% plastic strain which are not fully captured in the prediction.

The last orientation is compression along LD, shown in Fig. 6.15. As mentioned earlier, only in this sample, an abnormal softening behavior is observed for compressive strains above 10%. To account for this phenomenon, a shear strain with a rate of 10^{-3} s^{-1} and tilted 50° from the loading axis is superimposed on the applied compressive strain for strains larger than 10% as shown in Fig. 6.15(c). This approximation was based on the shapes of the deformed grids in the middle region of the sample as obtained from the DIC method. This approach resulted in a successful prediction of the softening behavior and shows that the simple approximation to this complex behavior is satisfactory. Fig. 6.15(a) underlines the effect of superimposing the extra shear strain after 10% plastic strain.

Superimposing shear was also beneficial in terms of better agreement with the experimental texture measurement after compression. Namely, without the extra shear strain the correct position of the basal poles could not be attained (Fig. 6.16(a)); whereas with the shear strain imposed, basal poles reside at about 25° tilted from LD providing a good agreement with the experimental measurement as seen in Fig. 6.16(b). As for the active deformation systems, basal slip is the most active mode, then pyramidal <c+a> slip follows. Prismatic slip remains lowest and maintains about 10% relative activity. Although the twin volume fraction is not considerably different than the previous two orientation, higher yield strength in this orientation can be explained by the high pyramidal <c+a> slip activity. Since the loading axis is parallel to LD, where a high concentration of basal poles exist, pyramidal <c+a> slip having a comparably high CRSS is required to accommodate the deformation.

(a)

(b) **(c)**

Fig. 6.13. (a) Predicted stress-strain response during post-ECAE compression along ED is given along with the measured response for the extrusion case I. (b) Predicted relative activity of the operative deformation mechanisms responsible for the stress-strain response given in (a). (c) Predicted texture evolution at the end of 30% plastic strain applied along ED.

(a)

(b)   **(c)**
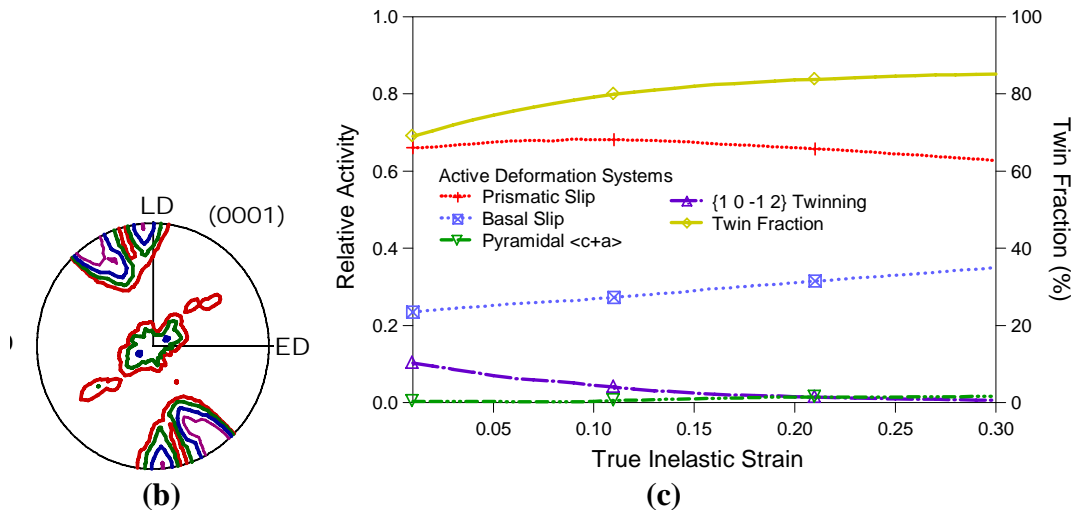
Fig. 6.14. (a) Predicted stress-strain response during post-ECAE compression along FD is given along with the measured response for the extrusion case I. (b) Predicted relative activity of the operative deformation mechanisms responsible for the stress-strain response given in (a). (c) Predicted texture evolution at the end of 30% plastic strain applied along FD.
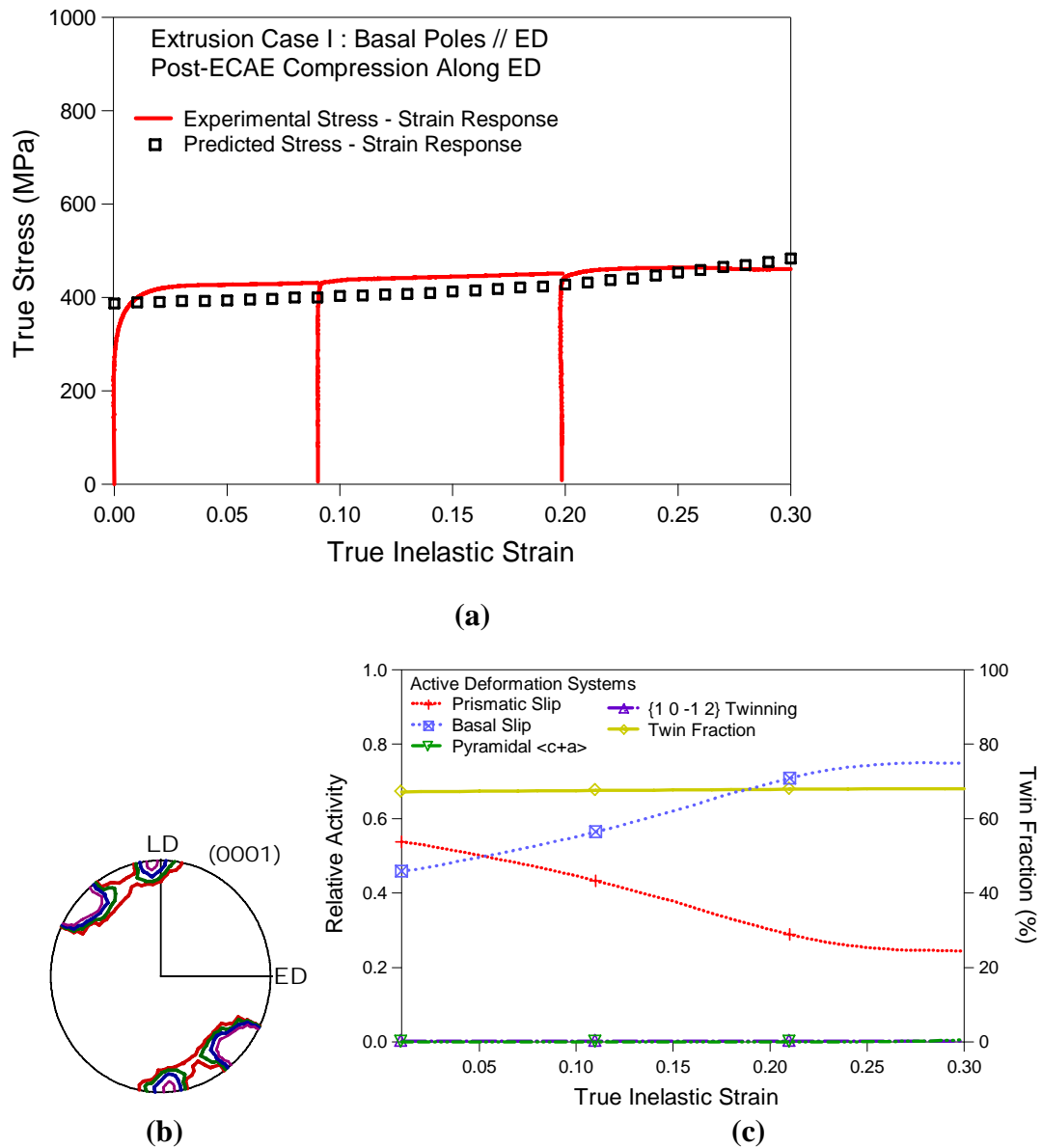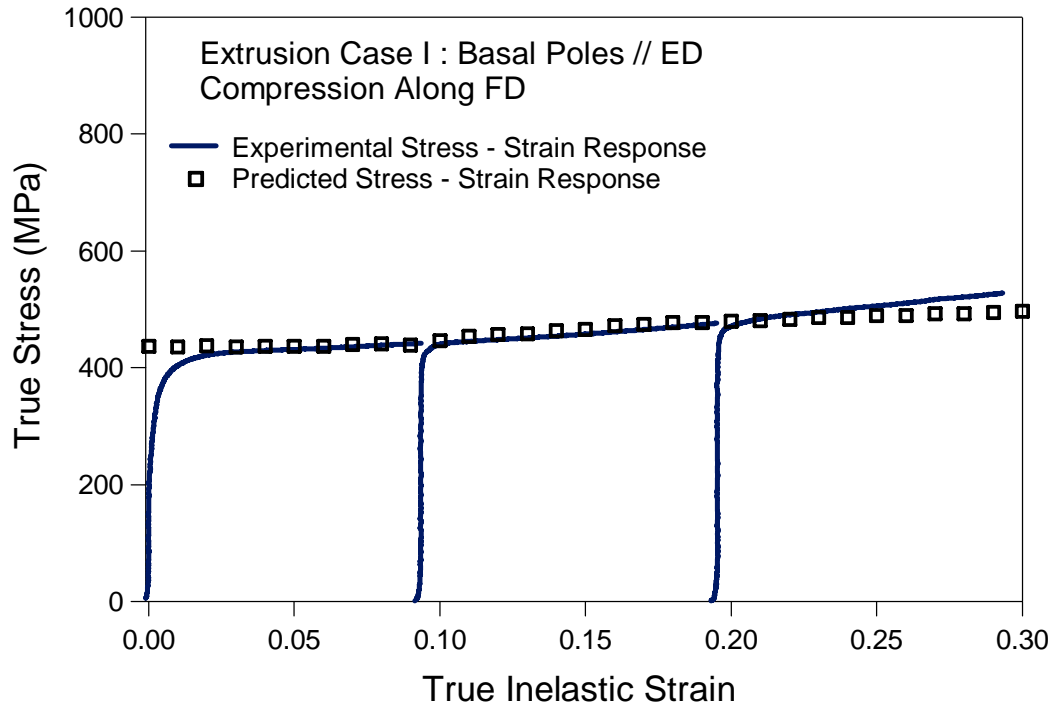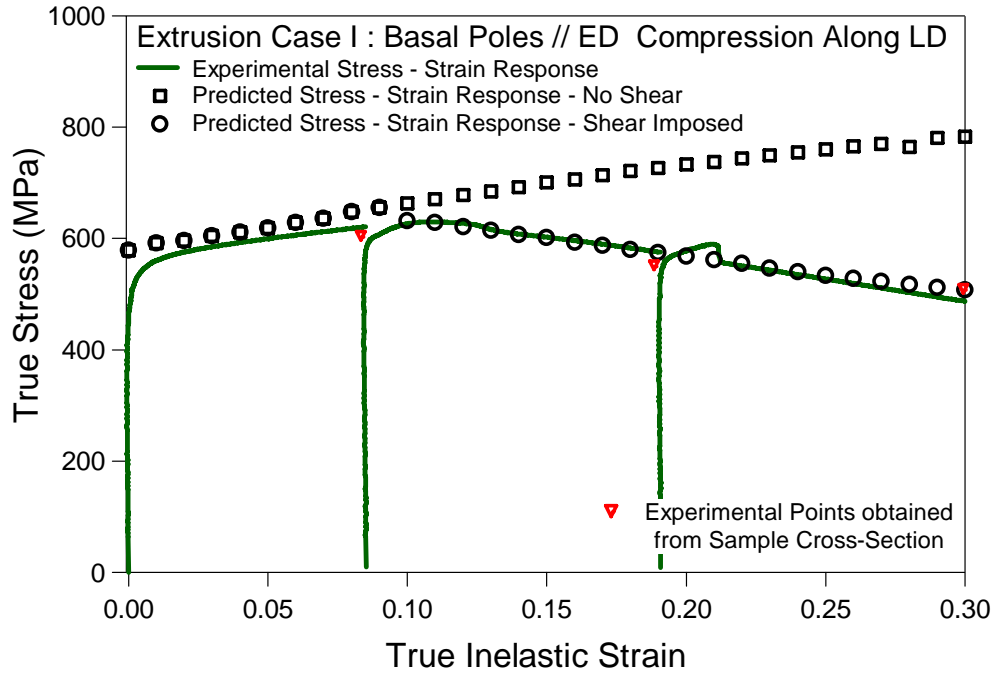
(a)
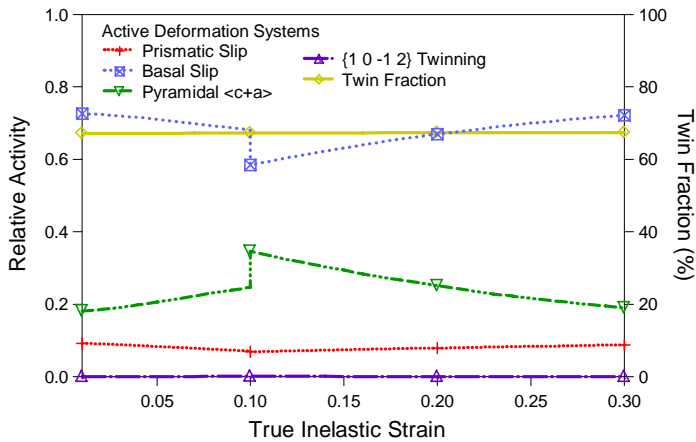
(b)
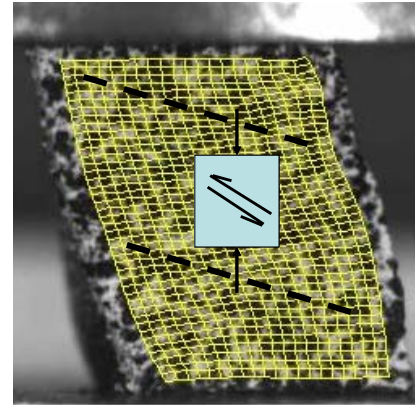
(c)

Fig. 6.15. (a) Predicted stress-strain response during post-ECAE compression along LD is given along with the measured response for the extrusion case I. (b) Predicted relative activity of the operative deformation mechanisms responsible for the stress-strain response given in (a). (c) Inhomogeneous strain field present during LD compression.
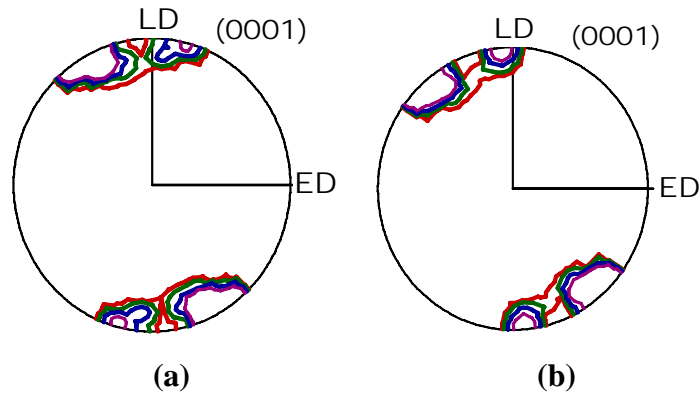
Fig. 6.16. Predicted texture evolution at the end of 30% plastic strain applied along LD with (a) no shear strain superimposed and (b) shear strain superimposed.

As observed from the relative activity predictions in Fig. 6.15(b) for all three compression samples, the main trends in the anisotropy of post-ECAE compressive flow response can be explained by the crystallographic texture evolved during ECAE. However, in the previous chapter on Ti and Ti64, it was shown that anisotropy in the flow response of ECAE processed materials is attributed to the simultaneous effect of texture and processing induced microstructure. It is surprising that the model performed so well in predicting the texture evolution during ECAE and post-ECAE flow response, despite the fact that substructure evolution was neglected. This suggests that crystallographic texture and multiple deformation modes in Zr are the key factors governing texture and plastic anisotropy. The reason why texture can sufficiently describe the anisotropy in this case is mainly due to the single pass extrusion preventing the development of an influential substructure.

To summarize, the texture evolution during ECAE and both the texture evolution and the mechanical response in three orthogonal directions after post-ECAE compression experiments were successfully predicted. The merit is that these were accomplished using a single set of hardening parameters and only using the initial crystallographic texture of the as-received material as the input to the VPSC model.

6.6.2. Prediction of the Extrusion Case II

For predictions of this extrusion case, the only input changed in our model is the initial texture where the basal poles are along FD. Figs. 6.17(a) to 6.17(c) show that the texture prediction is in reasonable agreement with the experimental measurement after ECAE and emphasize the significance of including basal slip as an active deformation mechanism. It is important to mention that the predictions overestimate the texture strength concentrated around FD. Comparing the relative activities of deformation mechanisms, it is seen in Fig. 6.17(d) that basal slip continues to increase and reaches about 40% of the total activity. Prismatic slip decreases at a low rate and consumes about 60% of the total activity. In contrast to the previous extrusion case, the activity of prismatic slip is definitely higher, whereas the basal slip activity is much lower. Moreover, the pyramidal <c+a> activity almost ceases after the first 10% upsetting strain. The twin volume fraction after a single ECAE pass reaches about 60%. As in the previous extrusion case, pyramidal <c+a> slip and $\{10\bar{1}2\}$ twinning are mostly activated during the initial 10% compressive strain, where the billet in the die upsets.

The yield strength level and the low hardening rate in the ED sample is successfully captured in the simulations as seen in Fig 6.18(a). The observed counter clockwise rotation of basal poles is captured as displayed in the texture evolution predictions of Fig. 6.18(c). However, the low intensity poles appearing near ED in the measured texture are not predicted. The major deformation systems are prismatic slip and basal slip. The former system accommodates about 70% of the applied strain. There is also a slight activity of $\{10\bar{1}2\}$ tensile twins.

Predictions for the compression along FD slightly overestimated the yield strength level; however the hardening rate is accurately predicted especially for strains larger than 10% as demonstrated in Fig. 6.19(a). Fig. 6.19(b) shows that the texture evolution prediction also agrees well with the experimental measurement. The exact locations of the two peaks around FD are not established properly in the simulations; still the main locations of the basal poles are reasonably established. It is seen that during FD compression, all four deformation systems contribute substantially. Especially, pyramidal <c+a> slip and twinning activities are higher than observed for the other two orientations

and thus overestimates the yield strength level in the prediction. This is mainly due to the presence of a high basal pole density around FD in the ECAE texture prediction.
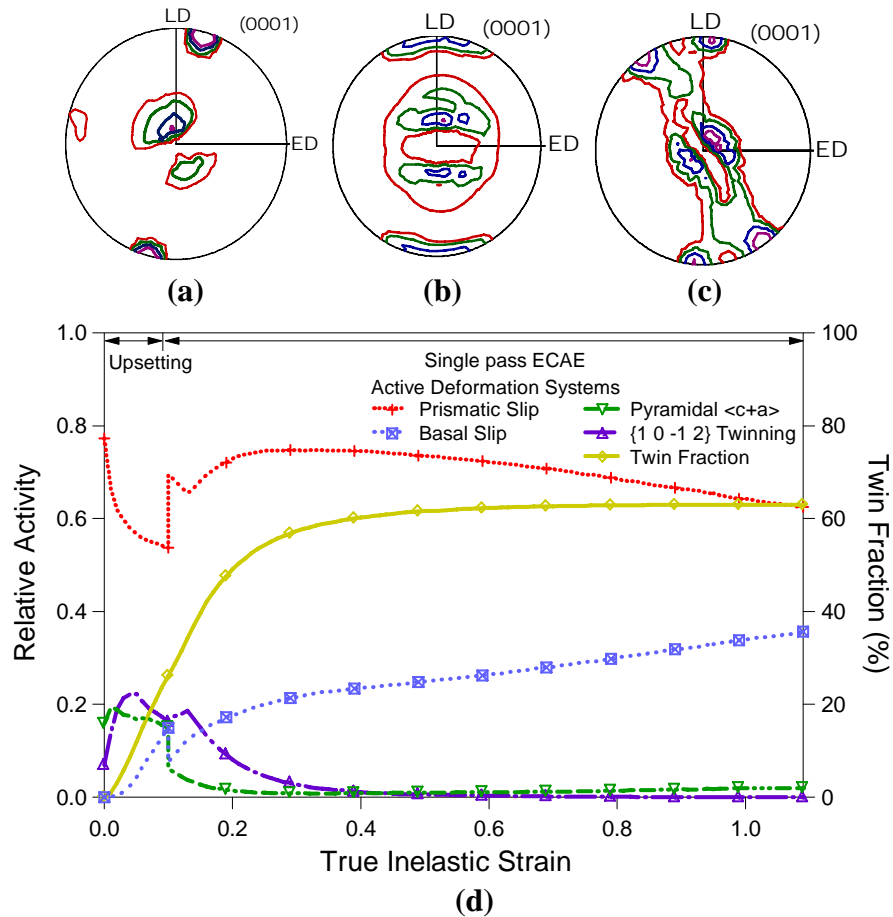
Fig. 6.17. Predicted texture evolution of Zr during single ECAE pass; (a) without basal slip, (b) after initial upsetting, (c) with basal slip and upsetting. (d) Predicted relative activity of the operative deformation mechanisms during the extrusion case II.

As described in Section 6.5.2, the LD sample exhibited the softening behavior for strains over 10%, and thus superimposing an extra shear strain is necessary to account for this effect as in the previous extrusion case. The details about the extra shear strain were given earlier in Section 6.6.1 for modeling the LD response of the previous extrusion case and were not changed for simulating the present case.

(a)

(b)   **(c)**
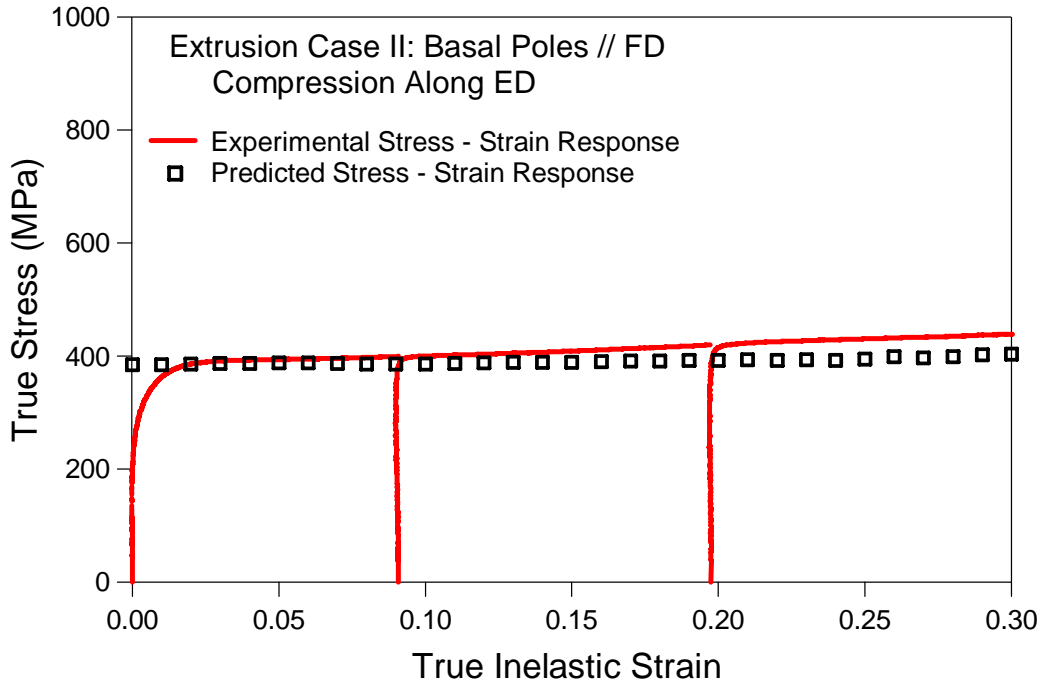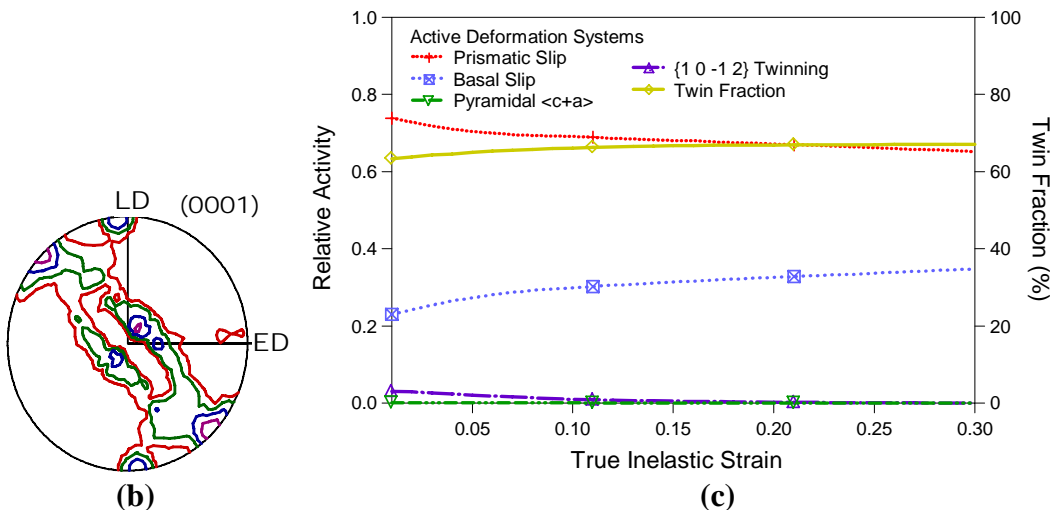
Fig. 6.18. (a) Predicted stress-strain response during post-ECAE compression along ED is given along with the measured response for the extrusion case II. (b) Predicted relative activity of the operative deformation mechanisms responsible for the stress-strain response given in (a). (c) Predicted texture evolution at the end of 30% plastic strain applied along ED.
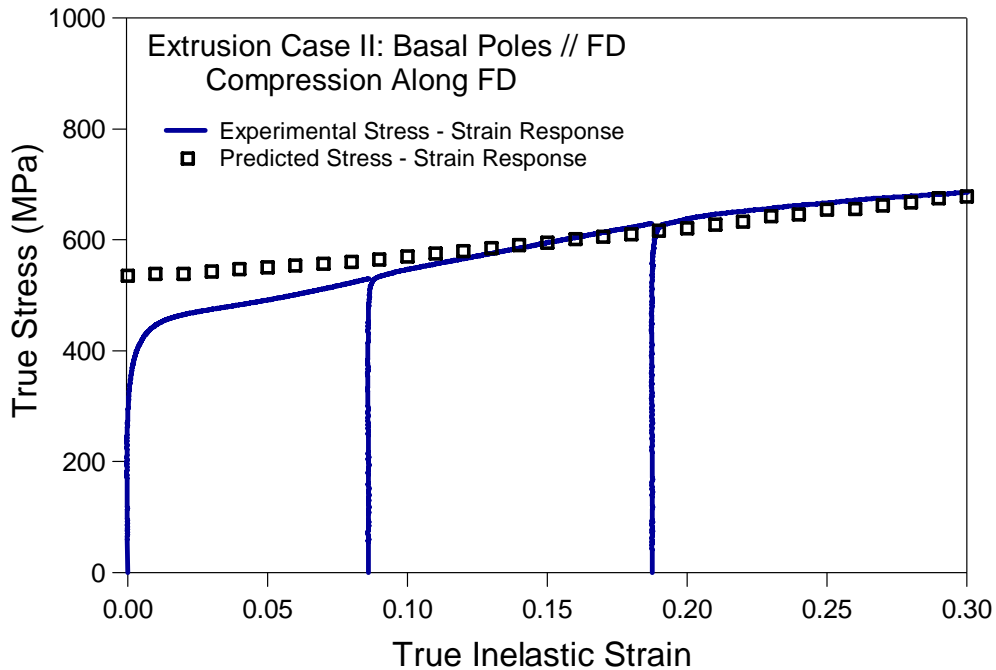
(a)
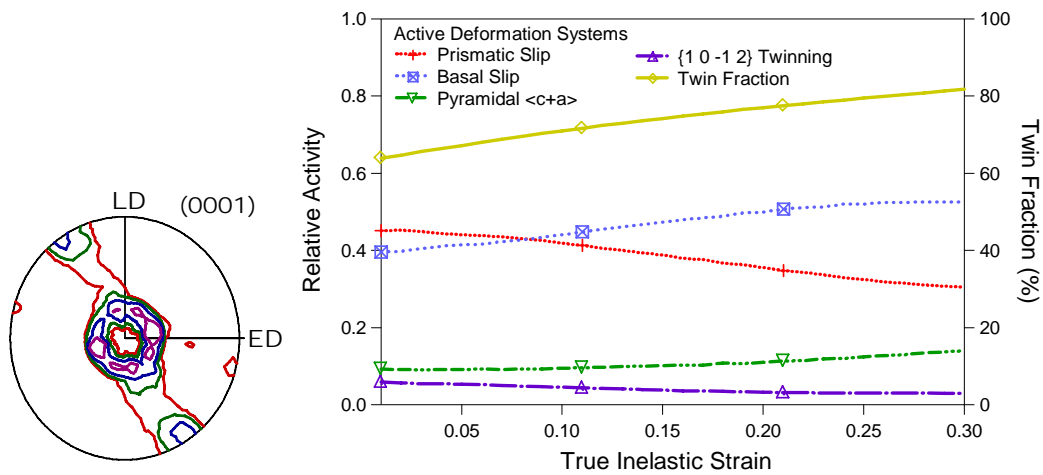
(b)   **(c)**

Fig. 6.19. (a) Predicted stress-strain response during post-ECAE compression along FD is given along with the measured response for the extrusion case II. (b) Predicted relative activity of the operative deformation mechanisms responsible for the stress-strain response given in (a). (c) Predicted texture evolution at the end of 30% plastic strain applied along FD.

(a)

(b)

(c)
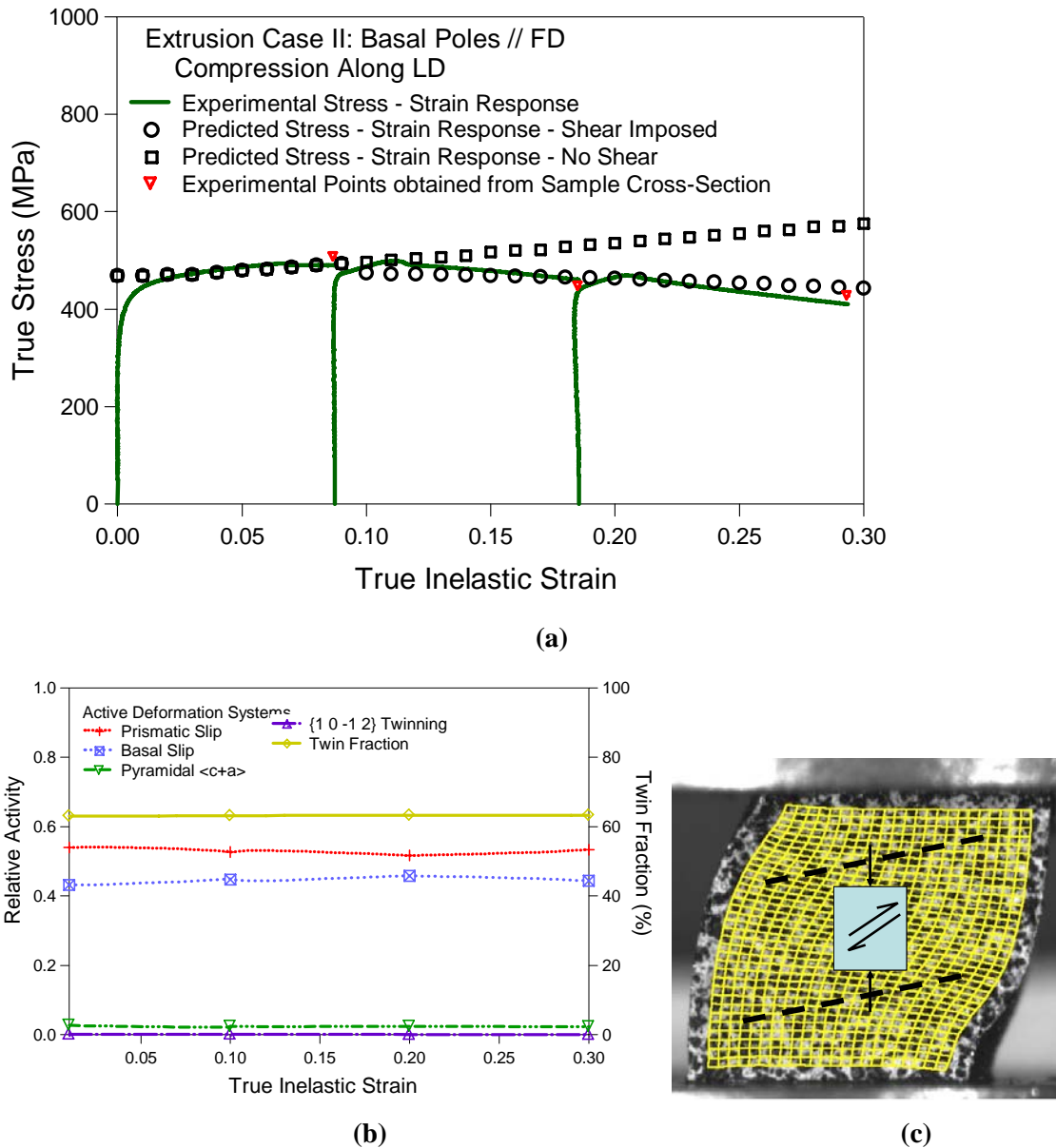
Fig. 6.20. (a) Predicted stress-strain response during post-ECAE compression along LD is given along with the measured response for the extrusion case II. (b) Predicted relative activity of the operative deformation mechanisms responsible for the stress-strain response given in (a). (c) Inhomogeneous strain field present during LD compression.

Fig. 6.20(a) compares the two predicted flow curves showing the effect of imposed extra shear strain. The yield strength level, the hardening rate and the softening above 10% plastic strain are successfully captured. As in the other two sample orientations, the major active deformation systems are prismatic and basal slip. These two systems accommodate the applied strain almost equally as seen in Fig. 6.20(b). There is also a slight activity of pyramidal <c+a> slip activity. Without the extra shear strain imposed, as presented in Fig. 6.20(c), the basal poles on the perimeter are aligned with LD (Fig. 6.21(a)). This does not resemble the experimental observation. A better agreement is achieved when the extra shear strain is in effect, as evidenced in Fig. 6.21(b). Regardless, the basal pole concentration around FD is overestimated.

Comparing the texture evolutions and active deformation systems during post-ECAE compression experiments, the main trends in the flow anisotropy is attributed to the texture formed after ECAE. As for the previous extrusion case, the texture evolution during ECAE and both the texture evolution and the mechanical response in three orthogonal directions after post-ECAE compression experiments were successfully predicted. In achieving this, no change has been made in our model keeping all the parameters the same. As a result, the deformation mechanisms responsible for texture evolution and mechanical response after ECAE were identified, demonstrating the importance of initial billet texture.

(a)   (b)
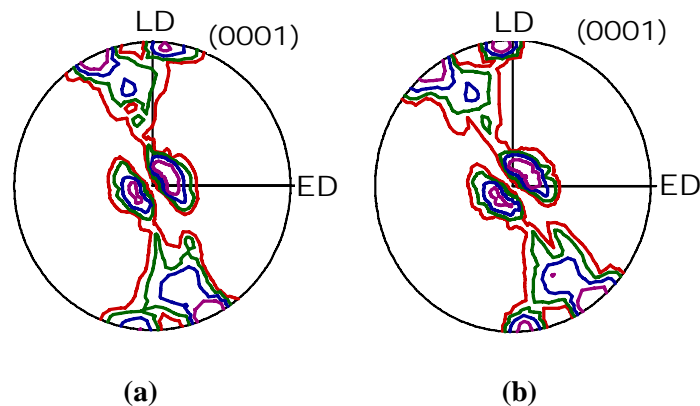
Fig. 6.21. Predicted texture evolution at the end of 30% plastic strain applied along LD with (a) no shear strain superimposed and (b) shear strain superimposed.

6.6.3. Room Temperature Operation of Basal Slip

As reported in the literature, basal slip is not a common deformation mechanism during room temperature deformation of pure Zr. Studies focusing on the factors determining the preference between prismatic and basal slip conclude that c/a ratio, stacking fault energies of prism and basal planes and the oxygen content level are the most important to consider [1, 250, 251]. It is known that dislocations tend to slip on the close packed planes and along the close packed directions to minimize the Peirels-Nabarro forces. The c/a ratio determines relative packing density of prismatic and basal planes. The lower c/a ratio increases the atomic packing density on prismatic planes and favors deformation on them. Since c/a ratio of Zr is 1.593 [1], lower than the ideal ratio of 1.633, one expects to observe prismatic slip as the primary slip mode. In contrast, in hcp materials with c/a ratios larger or very close to 1.633, such as Zn and Mg, basal slip is preferred over prismatic slip. Another view that suggests the preference of prismatic slip over basal slip is the relatively low stacking fault energy (SFE) of prismatic planes in Zr [250, 251]. Low SFE on prismatic planes will decrease the tendency to cross slip due to the extended stacking faults and will thus confine the dislocations on the prismatic planes.

Impurity content can also be influential on the selection of active deformation systems. However, reports on this issue have been contradictory. Conrad [144] reported that the presence of oxygen increases the c/a ratio, dropping the packing density of prismatic planes. This suggests that basal slip is more likely in such a scenario. In addition, Churchman [252] reported that the difference between CRSS levels of prismatic and basal slip in titanium decreases with increasing impurity levels in favor of the latter. In contrast, a study on titanium specimens with five different oxygen contents indicated that increasing oxygen content is effective in activating prismatic slip [199]. Furthermore, presence of impurities decreases the SFE on prismatic planes [246], making prismatic slip favorable, as discussed above.

Nevertheless, there are a few instances where basal slip activity at low temperatures is documented via experimental observations and/or modeling studies on Zr and its alloys. Dickson and Craig [248] showed microscopic evidence of basal slip of screw dislocations in Zr consisting of one to five crystals. At regions of high stress and at

instances of high strain rate pronounced basal slip was observed at room temperature. With a similar idea, Akhtar and Teghtsoonian [246] attributed the dynamic recovery in stage III hardening during tensile deformation of Zr single crystals to cross slip from prismatic to basal planes. Martin and Reed-Hill [249] explained the development of kink bands in polycrystalline zirconium at ambient temperature by basal slip.

There are also few studies where the need for basal slip for successful texture predictions is demonstrated using polycrystal plasticity modeling [194, 236, 241, 253, 254]. Philippe et al. [194] and Salinas-Rodriguez [253] included basal slip in their simulations to capture the texture evolutions during cold rolling of pure Zr and high strain compression of Zr-2.5Nb at room temperature, respectively. The latter study also showed that with increasing temperature the activity of basal slip exceeded that of prismatic slip. More recently, the effect of initial texture on the texture evolution during channel die compression of Zr702 was studied [254]. Texture predictions agreeing with experimental measurements included basal slip as an active deformation mechanism, especially in the samples with specific initial textures. In those samples, basal slip traces were identified using optical microscopy at 20% plastic strain. Additionally for the same samples, orientation factors during channel die compression (similar to the Schmid factor in axial deformation) for individual grains were comparably higher for basal slip [254].

In the present work, Zr billets with two different strong textures are used where they experience a strain state of compression plus simple shear up to high levels during ECAE. It is believed that the initial strong textures used accompanied with the high stress levels reached during simple shear ECAE processing supply the driving forces for the mechanisms responsible for basal slip in Zr at room temperature in this study. A similar explanation was given in Section 5.7.1 for the occurrence of profuse compression twinning during ECAE of Ti64

6.7. Conclusions

The present chapter was aimed at bridging the processing microstructure, the crystallographic texture and the post-ECAE mechanical behavior to gain a better understanding into the effect of microstructure and texture evolution on the post-ECAE flow response of pure Zr. This goal was accomplished by combining an experimental and

computational approach. Room temperature single pass ECAE of pure Zr was followed by compression experiments in three orthogonal directions to identify the effect of severe plastic deformation via simple shear on flow anisotropy. Texture measurements and flow responses were predicted using the VPSC model for a better understanding of the operating deformation mechanisms. This study was conducted on two initial Zr billet textures to demonstrate the general trends in microstructural development and texture evolution during ECAE and post-ECAE mechanical response, including plastic flow anisotropy. The predictive power of the computational model utilized is exhibited via accurate simulations of the aforementioned material properties. The major conclusions of this chapter can be summarized as:

1. Similar to the other hcp materials examined in this study, ECAE of pure Zr resulted in improved yield strengths due to grain refinement down to submicron regime achieved by single pass ECAE at room temperature.

2. ECAE of pure Zr leads to the alignment of basal planes with the long axes of the elongated grains, i.e., basal poles are tilted about 25° from the LD after a single pass. This texture evolution was observed regardless of the initial billet texture.

3. Considerable plastic flow anisotropy is present after ECAE as indicated by compression experiments along three orthogonal directions of the extruded billets up to 30% plastic strain. The main trends in anisotropy observed after both extrusions are attributed to the crystallographic texture evolved during ECAE. The reason why texture can sufficiently describe the anisotropy in this case is mainly due to the single pass extrusion preventing the development of an influential substructure.

4. Activity of basal slip was necessary for accurate predictions of texture evolution during ECAE and the texture evolution and flow response during post-ECAE compression experiments. Although uncommon, room temperature operation of basal slip is attributed to the initial strong textures used accompanied with the high stress levels generated via the simple shear strain state of ECAE.

5. The softening behavior during axial compression of the LD samples in both extrusion cases is due to a complex strain state induced by the strong asymmetric texture in the material. This anomalous deformation behavior was rationalized by

considering the orientation relation between the strong texture in the material and the loading axis. The unexpected softening response was accurately predicted by imposing an extra shear strain to the axial compressive strain without changing any material parameters.

6. The main deformation mechanisms responsible for texture evolution during ECAE and both the texture evolution and the mechanical response along three orthogonal directions during the post-ECAE compression experiments were successfully predicted using a single set of hardening parameters in both extrusion cases.

6.8. Suggestions for Future Work

One of the major findings of this study was that including basal slip in the simulations was required to correctly predict the experimental texture evolutions and mechanical responses. Detailed TEM studies involving Burger's vector analysis is necessary to shed light on the operation of individual slip systems and would be the most direct evidence. However, this might require a very intensive work and turn out to be inconclusive due to the very high dislocation density present in the severely deformed materials. Additionally, TEM studies will not only help identify basal slip, it will also form a stronger basis to justify the use of remaining deformation mechanisms (prismatic slip, pyramidal <c+a> slip and $\{10\bar{1}2\}$ tensile twins) in the simulations.

Another assumption in the simulations was the separation of the ECAE process into two parts consisting of an upsetting compressive strain state followed by simple shear strain state. Although this approach gave reasonable predictions, in reality the two strain states might be acting simultaneously. Macro simulations taking advantage of the finite element analysis (FEA) can verify this argument. Also for simulating the response of LD compression samples, utilizing an approximate shear strain for the last 20% straining can be improved further by identifying the average strain field in the sample via DIC method.

The continuation of ECAE up to higher number of passes could be pursued due to two reasons. First of all, in more practical sense it will help refine the grain size further leading enhanced strength levels. With single pass ECAE, the trends in anisotropy could

be sufficiently explained by crystallographic texture arguments. As opposed to what is observed during compression of single pass extruded copper along FD [31], no abrupt spike followed by a softening is observed in the FD stress-strain response of Zr after similar extrusion conditions. Higher number of ECAE passes will lead to the development of a processing induced microstructure and provide a platform for investigating its effects of on possible plastic flow anisotropy.

CHAPTER VII
SUMMARY AND MAIN CONCLUSIONS

Combining ECAE and cold rolling, strength and ductility levels reaching to those of commercial Ti-6Al-4V alloy were achieved in CP grade 2 Ti. ECAE of grade 4 Ti took place at higher deformation temperatures due to higher oxygen content of this material, though still proved to be a suitable method for refining grain size and improving strength properties. In both materials post processing annealing treatments were crucial in enhancing ductility levels. Strong in-plane anisotropy in yield strengths of the grade 2 Ti ECAE processed plus rolled slabs was observed which can not be attributed to the sole effect of crystallographic texture because of the presence of a directional substructure affecting the mean free path of dislocations. Taylor factors were used to distinguish the effects of crystallographic texture and microstructural morphology.

High temperature deformation twinning and grain refinement during ECAE of Ti64 led to a noteworthy improvement in flow stresses under tension and compression at room temperature. Strong directional anisotropy of yield strengths was evident which can not be explained only by texture and additional effects due to asymmetry of critical resolved shear stresses of deformation modes and the processing induced deformation structure were suggested. It was also concluded that twinning can be one of the main modes of deformation in difficult-to-work alloys in a wide range of temperatures as long as high strength levels are sustained in the microstructure.

Texture evolution and post ECAE mechanical response were demonstrated in high purity Zr. Experimental observations were supported by polycrystal plasticity predictions. The post-ECAE compression experiments showed that the main trends in anisotropy can be sufficiently explained by the texture evolved after a single ECAE pass. Basal slip was dictated as a mandatory deformation mechanism for accurate texture and flow behavior predictions. Regardless of the initial billet texture, a single ECAE pass led to similar texture evolutions where basal planes are aligned with the long axis of the elongated grains.

CP Ti, both grade 2 and grade 4, Ti64 and pure Zr exhibited high strength levels due to grain refinement via ECAE processing. Only in CP grade 2 Ti, cold rolling was

utilized as an additional strain path change mechanism for further microstructural refinement. This second step may in principle be applied to CP grade 4 Ti, Ti64 and Zr as well. However, especially for CP grade 4 Ti and Ti64, the temperature of deformation for this additional step have to be increased due to their relatively limited ductility. As a result, due to recovery effects, a secondary deformation step after ECAE might not be as beneficial as in the case of CP grade 2 Ti.

In both Ti64 and Zr, single ECAE pass led to similar texture evolution although the extrusion temperatures and rates were different. In both cases, basal slip was included as an active deformation system for accurate texture predictions. Higher number of ECAE passes with various routes should be conducted to see the effect of applied strain and strain path change on this similarity.

The anisotropy in yield strengths of CP Ti was explained by a simultaneous contribution of texture and processing induced microstructure, whereas in Zr main trends in anisotropy could be attributed to the texture evolved after ECAE. This contrast was believed to be due to the absence of a well developed dislocation substructure in UFG Zr after a single ECAE pass and the presence of a highly directional microstructure in UFG Ti after multiple ECAE passes followed by cold rolling. It is expected that higher number of ECAE passes will lead to a well developed dislocation substructure in UFG Zr and thus increase the contribution of microstructure on yield strength anisotropy.

To summarize, the present work studied the effect of strain path changes induced by severe plastic deformation on the microstructure, crystallographic texture and flow behavior of three hexagonal close packed (hcp) material systems, i.e. CP Ti, Ti64 and high purity Zr. Post-SPD texture evolutions and mechanical behaviors are also examined in detail. This provided a significant contribution to the field, not only due to the very few number of studies focusing on hcp materials, but also due to the unique approach bridging the processing-microstructure-property features for gaining a comprehensive understanding of the material behavior. The main conclusions considering all three hcp material systems under study are:

1. Severe plastic deformation of hcp materials, although challenging, is achievable and results in UFG microstructures with considerable increase in flow strength levels of the materials. The strength levels can be further improved by taking

advantage of abrupt strain path changes via conventional deformation methods subsequent to ECAE. Usually, application of post-ECAE heat treatments is necessary to obtain optimum mechanical properties combining high levels of strength and ductility.

2. Depending on the ECAE route followed, a strong texture combined with an oriented microstructural morphology can be developed in UFG hcp materials. The post-ECAE mechanical response, especially the plastic flow anisotropy, of UFG hcp materials are mainly dictated by these two factors, i.e. crystallographic texture and microstructural morphology. In relation with the number of ECAE passes, the ECAE route used and the specific material studied, the relative importance of these two mechanisms on flow anisotropy varies.

3. The texture evolution during ECAE of hcp materials and the post-ECAE texture evolution and mechanical response during straining along any given direction can be accurately predicted in cases where texture and multiplicity of deformation modes govern the plastic anisotropy.

4. Regardless of the material studied, the initial billet texture and the extrusion conditions such as extrusion rate and temperature, ECAE of hcp materials revealed similar crystallographic texture evolutions. This finding hints at a common deformation mechanism occurring in all cases studied which is believed to be basal slip. The occurrence of a common plasticity mechanism irrespective of material inherent properties and processing conditions suggests that its activity is related to the applied deformation mode.

5. Activation of special deformation systems in unexpected conditions, such as high temperature twinning in Ti64 and room temperature activity of basal slip in pure Zr, can be observed during ECAE. These instances can be attributed to the state and level of strain applied during ECAE providing microstructures with high strength levels that trigger the activity of uncommon deformation mechanisms.

REFERENCES

[1]   Tenckhoff E. Journal ASTM International 2005;2:199.

[2]   Philippe MJ, Bouzy E, Fundenberger JJ. Mater Sci Forum 1998;273-275:511.

[3]   Valiev RZ, Islamgaliev RK, Alexandrov IV. Prog Mater Sci 2000;45:103.

[4]   Meyers MA, Mishra A, Benson DJ. Prog Mater Sci 2006;51:427.

[5]   Valiev RZ, Langdon TG. Prog Mater Sci 2006;51:881.

[6]   Valiev RZ, Estrin Y, Horita Z, Langdon TG, Zehetbauer MJ, Zhu YT. JOM 2006;58:33.

[7]   Gleiter H. Nanostruct Mater 1992;1:1.

[8]   Iwahashi Y, Horita Z, Nemoto M, Langdon TG. Acta Mater 1997;45:4733.

[9]   Iwahashi Y, Horita Z, Nemoto M, Langdon TG. Acta Mater 1998;46:3317.

[10]   Segal VM. Mater Sci Eng A 1999;271:322.

[11]   Humphreys FJ, Prangnell PB, Bowen JR, Gholinia A, Harris C. Phil Trans A 1999;357:1663.

[12]   Ko YG, Shin DH, Park KT, Lee CS. Scripta Mater 2006;54:1785.

[13]   Stolyarov VV, Zhu YT, Lowe TC, Islamgaliev RK, Valiev RZ. Nanostructured Mater 1999;11:947.

[14]   Stolyarov VV, Zhu YT, Lowe TC, Valiev RZ. Journal Nanosci Nanotech 2001;1:237.

[15]   Vinogradov AY, Stolyarov VV, Hashimoto S, Valiev RZ. Mater Sci Eng A 2001;318:163.

[16]   Yu SH, Shin DH, Park NJ, Huh MY, Hwang SK. Mater Science Forum 2002;408-412:661.

[17]   Yu SH, Ryoo HS, Shin DH, Hwang SK. Mater Research Soc 2002;730:143.

[18]   Agnew SR, Mehrotra P, Lillo TM, Stoica GM, Liaw PK. Acta Mater 2005;53:3135.

[19]   Agnew SR, Lillo TM, Macheret J, Stoica GM. In: Proceedings of the 2001 TMS Annual Meeting. Warrendale (PA): TMS; 2001. p. 243.

[20]   Shin DH, Kim I, Kim J. Metals and Materials Int 2002;8:513.

[21]   Semiatin SL, Segal VM, Goforth RE, Frey ND, DeLo DP. Metall Mater Trans A 1999;30:1425.

[22]   Semiatin SL, DeLo DP. Materials and Design 2000;21:311.

[23]   Cao WQ, Liu Q, Godfrey A, Hansen N. Mater Sci Forum 2002;408-412:721.

[24]   Li BL, Godfrey A, Meng QC, Liu Q, Hansen N. Acta Mater 2004;52:1069.

[25]   Winther G, Huang X. Advanced Eng Mater 2003;5:317.

[26]   Bowen JR, Prangnell PB, Jensen DJ, Hansen N. Mater Sci Eng A 2004;387-389:235.

[27]   Huang X, Winther G, Hansen N, Hebesberger T, Vorhauer A, Pippan R, Zehetbauer M. Mater Science Forum 2003; 426-432:2819.

[28]   Huang X, Hansen N. Mater Sci Eng A 2004;387-389:186.

[29]   Mahesh S, Tome CN, McCabe RJ, Kaschner GC, Beyerlein IJ, Misra A. Metall Mater Trans A 2004;35:3763.

[30]   Hansen N, Jensen DJ. Acta Metall Mater 1992;40:3265.

[31]   Beyerlein IJ, Tome CN. International Journal Plasticity 2007;23:640.

[32]   Peeters B, Van Houtte P, Kalidindi SR, Aernoudt E. Journal de Physique. IV 2001;11:4365.

[33]   Peeters B, Teodosiu C, Kalidindi SR, Van Houtte P, Aernoudt E. Journal De Physique. IV 2001;11:5119.

[34]   Liu Q, Huang X, Lloyd DJ, Hansen N. Acta Mater 2002;50:3789.

[35]   Winther G, Juul Jensen D, Hansen N. Acta Mater 1997;45:2455.

[36]   Gazder AA, Davies CHJ, Pereloma EV. Mater Forum 2005;29:210.

[37]   Gazder AA, Dalla Torre F, Gu CF, Davies CHJ, Pereloma EV. Mater Sci Eng A 2006;415:126.

[38]   Mishin OV, Gottstein G. Phil Mag A 1998;78:373.

[39]   Mishin OV, Gertsman VY, Valiev RZ, Gottstein G. Scripta Mater 1996;35:873.

[40]   Cao WQ, Godfrey A, Liu Q. Mater Sci Eng A 2003;361:9.

[41]   Yoo MH. Metall Trans A 1981;12 A:409.

[42]   Lebensohn RA, Tome CN. Acta Metall Mater 1993;41:2611.

[43]   Yoo MH, Morris JR, Ho KM, Agnew SR. Metall Mater Trans A 2002;33:813.

[44]   Paton NE, Backofen WA. Metall Trans 1970;1:2841.

[45]   Peeters B, Bacroix B, Teodosiu C, Van Houtte P, Aernoudt E. Acta Mater 2001;49:1621.

[46]   Peeters B, Kalidindi SR, Van Houtte P, Aernoudt E. Acta Mater 2000;48:2123.

[47]   Barlat F, Ferreira Duarte JM, Gracio JJ, Lopes AB, Rauch EF. International Journal Plasticity 2003;19:1215.

[48]   Gleiter H. Acta Mater 2000;48:1.

[49]   Gleiter H. Prog Mater Sci 1989;33:223.

[50]   Valiev RZ, Korznikov AV, Mulyukov RR. Mater Sci Eng A 1993;168:141.

[51]   Valiev R. Nature Materials 2004;3:511.

[52]   Koch CC, Cho YS. Nanostruct Mater 1992;1:207.

[53]   Fecht HJ. Nanophase Materials 1994:125.

[54]   Koch CC. Nanostruct Mater 1997;9:13.

[55]   Fecht HJ, Hellstern E, Fu Z, Johnson WL. Metall Trans A 1990;21:2333.

[56]   Valiev RZ. Mater Sci Forum 2003;426:237.

[57]   Haouaoui M, Karaman I, Maier HJ, Hartwig KT. Metall Mater Trans A 2004;35:2935.

[58]   Hartwig KT, Zapata H, Parasiris A, Mathaudhu SN. Powder Materials 2001;14:211.

[59]   Alexandrov IV, Zhu YT, Lowe TC, Islamgaliev RK, Valiev RZ. Metall Mater Trans A 1998;29:2253.

[60]   Nieman GW, Weertman JR, Siegel RW. Scripta Metall 1989;23:2013.

[61]   Sanders PG, Fougere GE, Thompson LJ, Eastman JA, Weertman JR. Nanostructured Mater 1997;8:243.

[62]   Sanders PG, Weertman JR, Barker JG. J Mater Research 1996;11:3110.

[63]   Erb U. Nanostructured Materials 1995;6:533.

[64]   Ebrahimi F, Zhai Q, Kong D. Scripta Mater 1998;39:315.

[65]   Sanders PG, Eastman JA, Weertman JR. Acta Mater 1998;46:4195.

[66]   Suryanarayana C, Koch CC. Hyperfine Interactions 2000;130:5.

[67]   Sanders PG, Eastman JA, Weertman JR. Acta Mater 1997;45:4019.

[68]   Segal VM. Mater Sci Eng A 1995;197:157.

[69]   Valiev RZ. Mater Sci Eng A 1997;234-236:59.

[70]   Saito Y, Utsunomiya H, Tsuji N, Sakai T. Acta Mater 1999;47:579.

[71]   Saito Y, Tsuji N, Utsunomiya H, Sakai T, Hong RG. Scripta Mater 1998;39:1221.

[72]   Tsuji N, Ito Y, Saito Y, Minamino Y. Scripta Mater 2002;47:893.

[73]   Chang CI, Du XH, Huang JC. Scripta Mater 2007;57:209.

[74]   Lee WB, Lee CY, Chang WS, Yeon YM, Jung SB. Materials Lett 2005;59:3315.

[75]   Mabuchi M, Kubota K, Higashi K. Materials Transactions 1995;36:1249.

[76]   Huang JY, Zhu YT, Jiang H, Lowe TC. Acta Mater 2001;49:1497.

[77]   Cornwell LR, Hartwig KT, Goforth RE, Semiatin SL. Mater Characterization 1996;37:295.

[78]   Barber RE, Dudo T, Yasskin PB, Hartwig KT. Scripta Mater 2004;51:373.

[79]   Iwahashi Y, Wang J, Horita Z, Nemoto M, Langdon TG. Scripta Mater 1996;35:143.

[80]   Hughes DA, Hansen N. Acta Mater 1997;45:3871.

[81]   Berbon PB, Furukawa M, Horita Z, Nemoto M, Langdon TG. Metall Mater Trans A 1999;30:1989.

[82]   Horita Z, Smith DJ, Nemoto M, Valiev RZ, Langdon TG. J Mater Research 1998;13:446.

[83]   Oh-Ishi K, Horita Z, Furukawa M, Nemoto M, Langdon TG. Metall Mater Trans A 1998;29:2011.

[84]   Gholinia A, Prangnell PB, Markushev MV. Acta Mater 2000;48:1115.

[85]   Stolyarov VV, Zhu YT, Alexandrov IV, Lowe TC, Valiev RZ. Mater Sci Eng A 2001;299:59.

[86]   Zhu YT, Lowe TC. Mater Sci Eng A 2000;291:46.

[87]   Huang X, Vorhauer A, Winther G, Hansen N, Pippan R, Zehetbauer M. In: Ultrafine Grained Materials III. Warrendale (PA): TMS; 2004. p. 235.

[88]   Bay B, Hansen N, Hughes DA, Kuhlmann-Wilsdorf D. Acta Mater 1992;40:205.

[89]   Kuhlmann-Wilsdorf D, Hansen N. Scripta Metall Mater 1991;25:1557.

[90]   Hughes DA. Mater Sci Eng A 2001;319-321:46.

[91]   Hansen N, Huang X, Hughes DA. Mater Sci Eng A 2001;317:3.

[92]   Winther G. Scripta Mater 2005;52:995.

[93]   Huang X. Mater Sci Eng A 2005;409:52.

[94]   Mishin OV, Juul Jensen D, Hansen N. Mater Sci Eng A 2003;342:320.

[95]   Liu Q, Hansen N. Scripta Metall Mater 1995;32:1289.

[96]   Juul Jensen D, Hansen N. Acta Metall Mater 1990;38:1369.

[97]   Barrett CS. Trans AIME 1939;135:296.

[98]   Liu Q, Hansen N. Proc R Soc London 1998;454:2555.

[99]   Wert JA. Acta Mater 2002;50:3125.

[100]   Duggan BJ, Lee CS. Scripta Metall Mater 1992;27:1503.

[101]   Lee CS, Duggan BJ. Acta Metall Mater 1993;41:2691.

[102]   Lee CS, Smallman RE, Duggan BJ. Mater Sci Tech 1994;10:862.

[103]   Li ZJ, Winther G, Hansen N. Mater Sci Eng A 2004;387-389:199.

[104]   Wu PD, Neale KW, Van Der Giessen E. Int Journal Plasticity 1996;12:1199.

[105]   Christian JW, Mahajan S. Prog Mater Sci 1995;39:1.

[106]   Yoo MH, Agnew SR, Morris JR, Ho KM. Mater Sci Eng A 2001;319-321:87.

[107]   Westlake DG. J Nucl Mater 1968;26:208.

[108]   Rapperport EJ. Acta Metall 1959;7:254.

[109]   Davies KG, Teghtsoonian E. 1963;227:762.

[110]   Groves GW, Kelly A. Phil Mag 1963;8:877.

[111]   Taylor GI. Journal Institute Metals 1938;62:307.

[112]   Agnew SR, Yoo MH, Tome CN. Acta Mater 2001;49:4277.

[113]   Obara T, Yoshinga H, Morozumi S. Acta Metall 1973;21:845.

[114]   Agnew SR, Duygulu O. Mater Sci Forum 2003;419-422:177.

[115]   Cottrell AH, Bilby BA. Phil Mag 1951;42:573.

[116]   Serra A, Bacon DJ. Phil Mag 1996;73:333.

[117]   Cahn RW. Acta Metall 1953;1:49.

[118]   Venables JA. Phil Mag 1961;6:379.

[119]   Yapici GG, Karaman I, Luo ZP, Chumlyakov YI. In: Ultrafine Grained Materials III. Warrendale (PA): TMS; 2004. p. 291.

[120]   Karaman I, Yapici GG, Chumlyakov YI, Kireeva IV. Mater Sci Eng A 2005;410-411:243.

[121]   Karaman I, Sehitoglu H, Maier HJ, Chumlyakov YI. Acta Mater 2001;49:3919.

[122]   Yoo MH, Lee JK. Phil Mag A 1991;63:987.

[123]   Partridge PG. Metall Rev 1967;12:169.

[124]   Mahajan S, Williams DF. Int Metall Rev 1973;18:43.

[125]   Gray III GT, Kaschner GC, Mason TA. In: Advances in Twinning. Warrendale (PA): TMS; 1999. p. 157.

[126]   Thompson N, Millard DJ. Phil Mag 1952;43:421.

[127]   Allen NP, Hopkins BE, McLennan JE. Proc R Soc London 1956;234:221.

[128]   Reed-Hill RE. In: The Inhomogeneity of Plastic Deformation. Materials Park (OH): ASM; 1973. p. 285.

[129]   Bell RL, Cahn RW. Proc Roy Soc 1957;239:494.

[130]   Gharghouri MA, Weatherly GC, Embury JD, Root J. Phil Mag A 1999;79:1671.

[131]   Partridge PG. Phil Mag 1965;12:1043.

[132]   Meyers MA, Vohringer O, Lubarda VA. Acta Mater 2001;49:4025.

[133]   Chin GY, Hosford W, Mendorf DR. Proc R Soc London;309:433.

[134]   Chun JS, Byrne JG, Bornemann A. Phil Mag 1969;20:291.

[135]   Gray III GT. Acta Metall 1988;36:1745.

[136]   Gray III GT. In: Advances in Twinning. Warrendale (PA): TMS; 1999. p. 337.

[137]   Song SG, Gray III GT. Metall Mater Trans A 1995;26:2665.

[138]   Marcinkowski MJ, Lipsitt HA. Acta Metall 1962;10:95.

[139]   Koike J. Metall Mater Trans A 2005;36:1689.

[140]   Hull D. Acta Metall 1961;9:191.

[141]   Lahaie DJ, Embury JD, Chadwick MM. Scripta Metall Mater 1992;27:139.

[142]   Meyers MA, Andrade UR, Chokshi AH. Metall Mater Trans A 1995;26:2881.

[143]   Christian JW. Metall Trans A 1982;13:509.

[144]   Conrad H. Prog Mater Sci 1981;26:123.

[145]   Hosford WF. In: The Mechanics of Crystals and Textured Polycrystals. Oxford: Oxford University Press; 1993.

[146]   Kocks UF, Tome CN, Wenk HR. In: Texture and Anisotropy. Cambridge: Cambridge University Press; 1998.

[147]   Gambin W. Key Engineering Materials 2004;274-276:253.

[148]   Gambin W. In: Plasticity and Textures. New York (NY): Kluwer Acdemic Publishers; 2001.

[149] Hu H, Goodman SR. Trans AIME 1963;227:627.

[150] Canova G, Kocks UF. Acta Metall 1984;32:211.

[151] Montheillet F, Cohen M, Jonas JJ. Acta Metall 1984;32:2077.

[152] Baczinski J, Jonas JJ. Acta Mater1996;44:4273.

[153] Sanchez P, Pochettino A, Chauveau T, Bacroix B. J Nuclear Mater 2001;298:329.

[154] Murty KL. Mater Sci Forum 2003;426-432:3575.

[155] Hill R. Proc R Soc London 1948;193:281.

[156] Backofen WA, Hosford W, Burke JJ. Trans ASM 1962;55:264.

[157] Bishop JFW, Hill R. Phil Mag 1951;42:414.

[158] Honneff H, Mecking H. In: Proceedings of the Sixth Int Conf on Textures of Materials. Tokyo: The Iron and Steel Institute of Japan; 1981. p. 347.

[159] Molinari A, Canova GR, Ahzi S. Acta Metall 1987;35:2983.

[160] Tome CN, Pochettino A, Penelle R. In: Proceedings of the Eighth Int Conf on Textures of Materials. Warrendale (PA): TMS, 1988. p. 985.

[161] Molinari A, Ahzi S, Kouddane R. Mechanics of Materials 1997;26:43.

[162] Beyerlein IJ, Lebensohn RA, Tome CN. Mater Sci Eng A 2003;345:122.

[163] Lebensohn RA, Tome CN, Maudlin PJ. J Mechanics Phys Solids 2004;52:249.

[164] Lebensohn RA, Tome CN. Mater Sci Eng A 1994;A175:71.

[165] Tome C, Canova GR, Kocks UF, Christodoulou N, Jonas JJ. Acta Metall 1984;32:1637.

[166] Tome CN, Lebensohn RA, Kocks UF. Acta Metall Mater 1991;39:2667.

[167] Kallend JS, Kocks UF, Rollett AD, Wenk HR. Mater Sci Eng A 1991;A132:1.

[168] Szpunar JA. J Mater Sci;19:3467.

[169] Eder OJ, Klemencic RJ. Journal Applied Crystallography 1975;8:628.

[170] Wenk HR, Lutterotti L, Vogel S. Nuclear Instruments Methods Physics Research A 2003;515:575.

[171] Von Dreele RB. Journal Applied Crystallography 1997;30:517.

[172] Wright SI, Adams BL. Metall Trans A 1992;23:759.

[173] Randle V, Engler O. In: Texture Analysis Macrotexture, Microtexture and Orientation Mapping. Boca Raton (FL): CRC Press; 2000.

[174] Wright SI. J Comp Assis Microscopy 1993;5:207.

[175]   Vendroux G, Knauss WG. Eng. Mechanics 1998;38:86.

[176]   Zhu YT, Kolobov YR, Grabovetskaya GP, Stolyarov VV, Girsova NV, Valiev RZ. J Mater Research 2003;18:1011.

[177]   Stolyarov VV, Zhu YT, Alexandrov IV, Lowe TC, Valiev RZ. Mater Sci Eng A 2003;343:43.

[178]   Stolyarov VV, Zhu YT, Lowe TC, Valiev RZ. Mater Sci Eng A 2001;303:82.

[179]   Bengus VZ, Tabachnikova ED, Natsik VD, Mishkuf I, Chakh K, Stolyarov VV, Valiev RZ. Low Temperature Physics 2002;28:864.

[180]   Tabachnikova ED, Bengus VZ, Stolyarov VV, Raab GI, Valiev RZ, Csach K, Miskuf J. Mater Sci Eng A 2001;309-310:524.

[181]   Yu SH, Shin DH, Park NJ, Huh MY, Hwang SK. Mater Sci Forum 2002;408-412:661.

[182]   Alexandrov IV, Beyerlein IJ. Mater Sci Forum 2005;472-485:460.

[183]   Agnew SR, Horton JA, Lillo TM, Brown DW. Scripta Mater 2004;50:377.

[184]   Choi WS, Ryoo HS, Hwang SK, Kim MH, Kwun SI, Chae SW. Metall Mater Trans A 2002;33:973.

[185]   Segal V, Goforth RE, Hartwig KT. U.S. Patent No. 5,400,633 1995.

[186]   Yapici GG, Karaman I, Luo ZP, Rack H. Scripta Mater 2003;49:1021.

[187]   Yapici GG, Karaman I, Luo ZP, Maier HJ, Chumlyakov YI. J Mater Research 2004;19:2268.

[188]   Donachie MJ. In: Titanium, A Technical Guide. Materials Park (OH): ASM International; 2000.

[189]   Jia D, Wang YM, Ramesh KT, Ma E, Zhu YT, Valiev RZ. Applied Physics Letters 2001;79:611.

[190]   Hoppel HW, May J, Goken M. Advanced Eng Mater 2004;6:781.

[191]   Mahesh S, Beyerlein IJ, Tome CN. Scripta Mater 2005;53:965.

[192]   Naka S, Kubin LP, Perrier C. Phil Mag A 1991;63:1035.

[193]   Akhtar A, Teghtsoonian E. Metall Trans A 1975;6:2201.

[194]   Phillipe MJ, Serghat M, Van Houtte P, Esling C. Acta Metall 1995;43:1619.

[195]   Gray III GT. Journal Physique IV 1997;7:423.

[196]   Haouaoui M, Karaman I, Maier HJ. Acta Mater 2006;54:5477.

[197] Karaman I, Sehitoglu H, Chumlyakov YI, Maier HJ, Kireeva IV. Metall Mater. Trans A 2001;32:695.

[198] Karaman I, Sehitoglu H, Beaudoev AJ, Chumlyakov YI, Maier HJ, Tome CN. Acta Mater 2000;48:2031.

[199] Williams JC, Sommer AW, Tung, P. P. Metall Trans 1972;3:2929.

[200] Lutjering G, Williams JC. In: Titanium. Berlin: Springer; 2003.

[201] Lutjering G. Mat Sci Eng A 1998;243:32.

[202] Dunst D, Mecking H. Zeitschrift fur Metallkunde 1996;87:498.

[203] DeLo DP, Semiatin SL. In: Ultrafine Grained Materials. Warrendale (PA): TMS; 2002. p. 257.

[204] Sergueeva AV, Stolyarov VV, Valiev RZ, Mukherjee AK. Scripta Mater 2000;43:819.

[205] Mishra RS, Stolyarov VV, Echer C, Valiev RZ, Mukherjee AK. Mater Sci Eng A 2001;298:44.

[206] Ko YG, Jung WS, Shin DH, Lee CS. Scripta Mater 2003;48:197.

[207] Kim WJ, Hong SI, Kim YS, Min SH, Jeong HT, Lee JD. Acta Mater 2003;51:3293.

[208] Yapici GG, Karaman I, Luo ZP. In: Ultrafine Grained Materials III. Warrendale (PA): TMS; 2004. p. 433.

[209] Salem AA, Kalidindi SR, Doherty RD. Acta Mater 2003;51:4225.

[210] Johnson AJW, Bull CW, Kumar KS, Briant CL. Metall Mater Trans A 2003;34:295.

[211] Follansbee PS, Gray III GT. Metall Trans A 1989;20:863.

[212] Pelissie C, Guetaz L, Baillin X, Moret F, Guichard D, De Monicault JM. Rev Metall 1996;93:1509.

[213] Williams JC, Baggerly RG, Paton NE. Metall Mater Trans A 2002;33:837.

[214] Bowen AW. Mater Sci Eng 1979;40:31.

[215] Shin DH, Kim I, Kim J, Kim YS, Semiatin SL. Acta Mater 2003;51:983.

[216] Beyerlein IJ, Tome CN. Mater Sci Eng A 2004;380:171.

[217] Mendelson S. Mater Sci Eng 1969;4:231.

[218] Mendelson S. Journal Applied Physics 1970;41:1893.

[219] Minonishi Y, Ishioka S, Koiwa M, Morozumi S, Yamaguchi M. Philos Mag A 1982;45:385.

[220] Kim I, Kim J, Shin DH, Liao XZ, Zhu YT. Scripta Mater 2003;48:813.

[221] Marcinkowski MJ, Miller DS. Phil Mag 1961;6:871.

[222] Copley SM, Kear BH. Acta Metall 1968;16:227.

[223] Goodchild D, Roberts WT, Wilson DV. Acta Metall 1970;18:1137.

[224] Fujita M, Kaneko Y, Nohara A, Saka H, Zauter R, Mughrabi H. Iron and Steel Institute Journal 1994;34:697.

[225] Zhu YT, Liao XZ, Srinivasan SG, Zhao YH, Baskes MI, Zhou F, Lavernia EJ. Applied Physics Letters 2004;85:5049.

[226] Chen M, Ma E, Hemker KJ, Sheng H, Wang Y, Cheng X. Science 2003;300:1275.

[227] Lecomte JS, Philippe MJ, Klimanek P. Revue Metall 1999;96:201.

[228] Fundenberger JJ, Philippe MJ, Wagner F, Esling C. Acta Mater 1997;45:4041.

[229] Zaefferer S. Mater Sci Eng A 2003;344:20.

[230] Bieler TR, Semiatin SL. Int Journal Plasticity 2002;18:1165.

[231] Gey N, Humbert M, Philippe MJ, Combres Y. Mater Sci Eng A 1996;219:80.

[232] Sakai T, Fine ME. Acta Metall 1974;22:1359.

[233] Jones IP, Hutchinson WB. Acta Metall 1981;29:951.

[234] Williams DN, Eppelsheimer DS. J Inst Met 1952;81:553.

[235] Cao WQ, Yu SH, Chun YB, Yoo YC, Lee CM, Shin DH, Hwang SK. Mater Sci Eng A 2005;395:77.

[236] Yu SH, Chun YB, Hwang SK, Shin DH. Phil Mag 2005;85:345.

[237] Lee BS, Kim MH. Mat Sci Eng A 2006;423:180.

[238] Kad BK, Gebert JM, Perez-Prado MT, Kassner ME, Meyers MA. Acta Mater 2006;54:4111.

[239] Tome CN, Maudlin PJ, Lebensohn RA, Kaschner GC. Acta Mater 2001;49:3085.

[240] Kaschner GC, Tome CN, Beyerlein IJ, Vogel SC, Brown DW, McCabe RJ. Acta Mater 2006;54:2887.

[241] Castelnau O, Francillette H, Bacroix B, Lebensohn RA. Journal Nuclear Mater 2001;297:14.

[242] Rodriguez AS, Jonas JJ. Metall Trans A 1992;23:271.

[243] Agnew SR, Mehrotra P, Lillo TM, Stoica GM, Liaw PK. Mater Sci Eng A 2005;408:72.

[244] Field RD, Hartwig KT, Necker CT, Bingert JF, Agnew SR. Metall Mater Trans A 2002;33:965.

[245] Addessio LB, Cerreta EK, Gray Iii GT. Metall Mater Trans A 2005;36:2893.

[246] Akhtar A, Teghtsoonian E. Acta Metall 1971;19:655.

[247] Akhtar A. J Nuclear Mater 1973;47:79.

[248] Dickson JI, Craig GB. J Nuclear Mater 1971;40:346.

[249] Martin JL, Reed-Hill RE. Trans AIME 1964;230:780.

[250] Legrand PB. Phil Mag B 1984;49:171.

[251] Xiao L, Gu H. Metall Mater Trans A 1997;28:1021.

[252] Churchman AT. Proc R Soc London 1954;226:216.

[253] Salinas-Rodriguez A. Acta Metall Mater 1995;43:485.

[254] Francillette H, Bacroix B, Gasperini M, Bechade JL. Acta Mater 1998;46:4131.

VITA

Guney Guven Yapici was born in Adana, Turkey in 1980. He graduated from Uskudar Science High School, Istanbul and started his education at Bogazici University, Istanbul. In July of 2001, he received his B.S. degree in mechanical engineering. Since January 2002, he has continued his studies in the Department of Mechanical Engineering at Texas A&M University. He has been conducting research on mechanics and materials science as a research assistant since then. He also served as a teaching assistant for the "Materials and Manufacturing Selection in Design" course. In May 2004, he received his M.S. degree in mechanical engineering. He worked as a graduate researcher in the Materials Science and Technology Division at Los Alamos National Laboratory for three months in the summer of 2006. He received his Ph.D. degree in mechanical engineering in August 2007. During his graduate studies, he published nine peer-reviewed journal articles. He has been an author on two conference proceedings. He also had the opportunity to present his research in more than twenty international conference symposia. He can be reached at his permanent address:

Akdogan Sk. Ay Apt.
40/7 Besiktas 80690
Istanbul, TURKEY.